THE HONG KONG
POLYTECHNIC UNIVERSITY
香港理工大學
Pao Yue-kong Library
包玉剛圖書館

Copyright Undertaking

This thesis is protected by copyright, with all rights reserved.

By reading and using the thesis, the reader understands and agrees to the following terms:

1. The reader will abide by the rules and legal ordinances governing copyright regarding the use of the thesis.
2. The reader will use the thesis for the purpose of research or private study only and not for distribution or further reproduction or any other purpose.
3. The reader agrees to indemnify and hold the University harmless from and against any loss, damage, cost, liability or expenses arising from copyright infringement or unauthorized usage.

IMPORTANT

If you have reasons to believe that any materials in this thesis are deemed not suitable to be distributed in this form, or a copyright owner having difficulty with the material being included in our database, please contact lbsys@polyu.edu.hk providing details. The Library will look into your claim and consider taking remedial action upon receipt of the written requests.

Pao Yue-kong Library, The Hong Kong Polytechnic University, Hung Hom, Kowloon, Hong Kong

http://www.lib.polyu.edu.hk

SEAMLESS LOW-POWER OMNIMEDIUM COMMUNICATION VIA PIEZOELECTRICITY

ZHENG GONG

PhD

The Hong Kong Polytechnic University

2025

The Hong Kong Polytechnic University
Department of Computing

Seamless Low-Power Omnimedium Communication via Piezoelectricity

Zheng GONG

A thesis submitted in partial fulfillment of the requirements for
the degree of Doctor of Philosophy
August 2024

CERTIFICATE OF ORIGINALITY

I hereby declare that this thesis is my own work and that, to the best of my knowledge and belief, it reproduces no material previously published or written, nor material that has been accepted for the award of any other degree or diploma, except where due acknowledgment has been made in the text.

Signature: _____

Name of Student: Zheng GONG

Abstract

The forthcoming 6G wireless network aims to deliver universal accessibility, ultra-high-speed connectivity, and low latency, fully integrating the global Internet of Everything (IoE). This ambitious goal necessitates the seamless integration of networks across diverse domains and mediums, including space, air, subterranean, in-body, in-solid, and underwater environments. Supported by this expansive vision, we propose the concept of omnimedium communication, which is centered on achieving seamless, low-power data transmission intra or across a wide variety of physical environments, transcending traditional communication barriers. With omnimedium communication, a wide range of modern societal applications becomes feasible, such as structural health monitoring (SHM) within concrete walls, soil environment surveillance, undersea exploration, and biometric monitoring within the human body.

Despite some progress in communication within non-aerial mediums and across different mediums, existing communication systems often grapple with issues such as lack of robustness, high energy consumption, and substantial size. This thesis introduces two innovative, piezoelectric-based communication paradigms designed to address these challenges. The first paradigm exploits the acoustic-electrical conversion properties of piezoelectric materials to develop passive intra-medium acoustic backscatter communication modules. The second paradigm employs the capacity of piezoelectric materials to radiate electromagnetic (EM) waves, facilitating the design of compact units capable of efficient cross-medium communication.

The first study introduces self-sensing concrete embedded with EcoCapsules, a novel battery-free, miniature piezoelectric backscatter node. This technology meets the critical demand for persistent SHM in civilian buildings, surmounting obstacles presented by wired connections and frequent battery replacement. By incorporating EcoCapsules within concrete structures, we establish robust in-concrete backscatter communication with notable throughput and energy harvesting capabilities, as demonstrated through comprehensive real-world testing.

The second study features MeAnt, a versatile IoT platform that enables cross-medium communication through piezoelectric-based mechanical antennas. This platform ensures seamless communication across various environments, such as air, water, soil, concrete, and biological tissues, exploiting the propagation characteristics of medium-frequency radios. MeAnt tackles prevalent issues such as interference from AM broadcasts and the inherent unidirectional nature of Piezo-MAs, employing a meticulously developed full-stack communication protocol that has proven effective, showcasing significant penetration depth and throughput in diverse environmental conditions.

Collectively, these studies underscore the transformative potential of piezoelectric materials in fostering seamless, low-power omnimedium communication. They provide groundbreaking solutions for intra-concrete SHM and establish versatile networks capable of operating across multiple mediums. These findings illustrate the adaptability and efficiency of piezoelectric technologies in omnimedium communication systems, paving the way for innovative applications and enhanced connectivity in diverse environments.

Publications Arising from the Thesis

Conferences:

1. Zheng Gong, Zhenlin An, Donghui Dai, Jingyu Tong, Shuijie Long, and Lei Yang, "Enabling Cross-Medium Wireless Networks with Miniature Mechanical Antennas", in Proc. of **ACM MobiCom**, 2024.

2. Zheng Gong, Lubing Han, Zhenlin An, Lei Yang, Siqi Ding, and Yu Xiang "Empowering Smart Buildings with Self-sensing Concrete for Structural Health Monitoring", in Proc. of **ACM SIGCOMM**, 2022.

3. Zheng Gong, Zhenlin An, Jingyu Tong, Donghui Dai, and Lei Yang, "Demo: Constructing Smart Buildings with In-concrete Backscatter Networks", in Proc. of **ACM MobiCom**, 2022.

4. Zheng Gong, Zhenlin An, Jingyu Tong, Donghui Dai, and Lei Yang, "Building the Future: Empowering Smart Structures with In-Concrete Backscatter Networks", in Proc. of **ACM Turing Award Celebration Conference-China**, 2023.

5. Donghui Dai, Zhenlin An, Zheng Gong, Qingrui Pan, and Lei Yang, "RFID+: Spatially Controllable Identification of UHF RFIDs via Controlled Magnetic Fields", in Proc. of **USENIX NSDI**, 2024.

Acknowledgments

As I approach the end of my PhD journey, it gives me great pleasure to write this acknowledgment to thank all the people who have helped me and all the things that have happened. It has been the most valuable asset and experience in my life!

Firstly, I would like to thank my PhD supervisor, Dr YANG Lei. I am honored to have the opportunity to be supervised by him. Three years ago, I was a master's student who didn't know much about IoT and mobile computing, and now I have a first glimpse of it. This would not have been possible without his guidance and help over these three years. Every group meeting and discussion, every time he revised my thesis, I benefited a lot. His obsession with research and grasp of details, as well as his flexible combination of various knowledge, have taught me many things that will last a lifetime.

Secondly, I would like to thank many of my group mates and collaborators. Dr AN Zhenlin has been a great help to me. He was always available to guide me from the basics and greatly inspired me. In addition, there are also Mr. DAI Donghui, Mr. TONG Jingyu, Mr. ZHAO Xiaopeng, Mr. MEI Zhimin, Dr. FENG Yuanhao, Dr. PAN Qingrui, Ms. YANG Xueyuan, and Mr. LIAO Sizong. Without the discussions with them, I could not have gained so many ideas and insights towards research. In addition, many excellent researchers at PolyU gave me help in both life and research, such as Mr. WANG Zhicheng, Mr. WANG Shen, Mr. ZHAMG Fengrui, Mr. WANG Guosheng, Mr. LONG Shuijie, Ms. LI Zhuhang, Ms. WANG Xuanzhi, Dr. LIANG

Zhixuan, Dr. LI Zecheng, and Mr. SONG Rui. I am always so grateful to meet such kind and nice people.

In addition, I would like to express my heartfelt gratitude to my parents, Mr LIAO Shengqiang and Ms GONG Bing. Coming to Hong Kong to do a PhD is never easy, and they have given me the best backing. Their unconditional support is the motivation for me to go all the way!

I want to send my sincerest thanks to my wife, Ms ZHANG Xinyu. It is her companionship and encouragement that make me stronger. Thank you for her selfless devotion and love!

Finally, a PhD is just a starting point of my career. I will continue marching on the path of research and striving for glory. As Taric said, I've been to the top of the mountain and the bottom of the gutter. There's much to learn from both. Victory belongs to the most tenacious!

Table of Contents

List of Figures

List of Tables

Chapter 1

Introduction

1.1 Omnimedium Communication for Internet of Everything

In the era of the Internet of Everything (IoE) [4], where billions of devices, systems, and services are interconnected across the globe, the need for seamless communication across various mediums has never been more critical. The term "omnimedium communication" describes the capacity to robustly transmit data across every physical environment (e.g., the air, water, soil, concrete, or biological tissues), whether within a single medium or between different mediums. This concept is vital for the IoE, as it seeks to transcend traditional barriers and create a truly integrated network that can operate ubiquitously in any given medium.

Omnimedium communication holds transformative potential for ocean and soil sensing and exploration, areas crucial for environmental monitoring and resource management. By deploying omnimedium-empowered Wireless Sensor Network (WSN) [5] nodes in these challenging environments, data on various sensors—such as temperature, salinity, soil moisture, and even CMOS—can be collected [6]. These sensors,

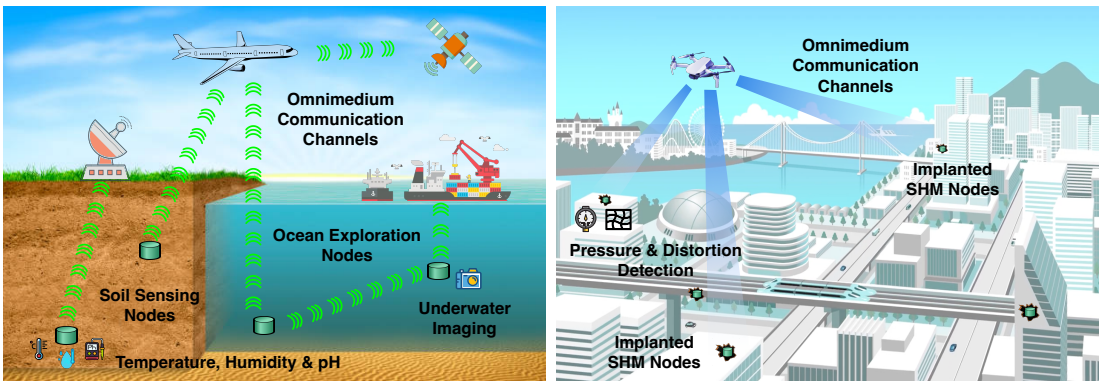

(a) Omnimedium Communication for WSNs (b) Omnimedium Communication for SHM

Fig. 1.1: Typical Application Scenario for Omnimedium Communication. (a) The underwater and underground WSN nodes report data across different mediums and within their respective environments. (b) The drone collects cross-medium communication data from the embedded SHM nodes.

embedded deep within the ocean or soil, rely on omnimedium communication to transmit data back to the surface or air with minimal power consumption. This capability is vital as it allows for real-time monitoring without the need for extensive and intrusive infrastructure. The data collected can enhance our understanding of ecological dynamics and assist in making informed decisions regarding ocean protection, environmental preservation, and agricultural practices. Omnimedium communication helps us better sense, explore, and monitor the whole physical space.

In the context of structural health monitoring (SHM) [7], omnimedium communication can revolutionize how we maintain and ensure the safety of critical infrastructure. By embedding sensor nodes within key structural elements of buildings, bridges, and other constructions, continuous data on the health of these structures can be wirelessly transmitted. This includes monitoring vibrations, stresses, and other potential indicators of structural failure [8]. Meanwhile, the low-power characteristic of these nodes ensures lifelong monitoring without frequent battery replacement. The ability of these sensors to communicate through materials such as concrete and metal, typical barriers in traditional communication systems, ensures that any signs of deterioration are detected early. This proactive monitoring can significantly enhance safety, reduce maintenance costs, and extend the lifespan of infrastructure by facilitating timely

interventions.

The application of omnimedium communication also extends significantly into the biomedical field, opening up innovative avenues for healthcare monitoring and diagnostics [9]. By utilizing miniature sensors that can communicate through biological tissues, medical professionals can obtain real-time data from inside the human body without the need for invasive procedures [10]. These sensors can monitor a wide range of physiological parameters such as heart rate, blood pressure, glucose levels, and organ functionality. Furthermore, omnimedium communication enables these sensors to transmit data seamlessly through the body to external receivers, thus facilitating continuous health monitoring. This capability is particularly crucial for the management of chronic diseases and post-operative care, where consistent and accurate data collection is essential for effective treatment planning. The low power characteristic of omnimedium communication eliminates the frequent need to replace batteries in in-vivo nodes.

1.1.1 In-concrete Communication for SHM

SHM is a critical discipline in civil engineering that involves the use of sensor networks to assess the condition of infrastructure, such as buildings, bridges, and dams [11]. SHM aims to detect and respond to signs of damage or deterioration that could potentially compromise structural integrity and safety. The primary goal of SHM is to ensure public safety and extend the lifespan of infrastructure while optimizing maintenance and repair activities. In a world where infrastructure failures can lead to significant economic loss and endanger lives, the importance of effective SHM can not be overstated. Traditional methods of monitoring structural health often rely on external measurements to evaluate parameters like stress, moisture, deformation, and pressure within a structure. While useful, these external methods can be fraught with inaccuracies and high levels of uncertainty due to their indirect nature. Misjudg-

ments and errors arising from these methods pose severe risks, potentially leading to catastrophic failures.

Omnimedium communication revolutionizes SHM by facilitating the transmission of data from sensors embedded within structures to the outside. This advanced communication technology ensures that data directly collected from the core of the infrastructure—where the most critical changes occur—is reliable and transmitted in real time, regardless of physical barriers such as concrete and steel. By enabling direct internal communication, omnimedium technology provides a more accurate and timely diagnosis of structural health. Further enhancing the efficacy of SHM, omnimedium communication can be seamlessly integrated with advanced data analytics and machine learning algorithms. This integration allows for the continuous analysis of incoming data to identify patterns or anomalies that may indicate potential structural failures. Machine learning models can predict deterioration and forecast potential problems before they manifest visibly, enabling preemptive measures that significantly mitigate risks.

The implementation of omnimedium communication in SHM systems offers numerous benefits, including increased accuracy in data collection, enhanced early warning capabilities, and reduced need for manual inspections, which are often hazardous and expensive. By ensuring continuous and reliable monitoring, this technology not only safeguards lives and properties but also contributes to the sustainable management and operation of vital infrastructure. As societies worldwide continue to expand and urbanize, the role of effective SHM systems, underpinned by robust communication technologies like omnimedium communication, becomes increasingly essential.

In summary, omnimedium communication represents a paradigm shift in how we approach structural health monitoring. By overcoming traditional communication barriers within structures and harnessing the power of real-time data analytics, this technology is set to play a pivotal role in the future of civil engineering and infrastructure management.

1.1.2 Cross-medium Communication for WSN

WSNs are pivotal in extending our ability to explore and interact with the world around us. These networks comprise sensors that collect data from their environment and communicate it wirelessly for analysis and decision-making. Specialized types of WSNs, such as Wireless Underground Sensor Networks (WUSN) [12], Wireless Underwater Sensor Networks [13], and Wireless In-vivo Sensor Networks (VSN [14] within the human body, enable exploration and monitoring in diverse and often challenging environments.

Despite their versatility, the effectiveness of WSNs in complex environments like oceans, soil, or biological tissues is often limited by the attenuation of traditional RF signals. In environments where RF signal loss is substantial, such as underwater or underground settings, the conventional methods of communication fail to perform efficiently. This significant attenuation not only reduces the range and reliability of the sensors but also increases the power consumption and operational costs due to the need for stronger signals and more sophisticated equipment. Omnimedium communication addresses these challenges by enabling low-power, cross-medium communication. This innovative approach allows WSNs to operate effectively in environments with high RF attenuation by adapting to the specific transmission characteristics of each medium—whether it's water, soil, or biological tissues. Through omnimedium communication, data transmission is no longer bound by the limitations of traditional RF signals, thus enhancing the scope and reliability of WSNs in critical applications.

For Wireless Underwater Sensor Networks, these networks can perform tasks such as probing the parameters of oceans, imaging underwater ecosystems, and guiding marine robots for seabed exploration. Omnimedium communication facilitates real-time data transmission across the boundary and back to surface stations, even through deep water that typically significantly attenuates conventional RF signals. For Wireless In-vivo Sensor Networks, sensors placed within the human body can monitor

health indicators like heart rate, glucose levels, and organ function with minimal intrusion. Omnimedium communication ensures that these sensors can reliably transmit data through biological tissues to external receivers, thus supporting advanced health monitoring and diagnostic systems. For Wireless Underground Sensor Networks in agricultural and geological applications, these sensors monitor soil conditions, detect early signs of landslides, or assess the health of crops. With omnimedium communication, the data from these underground sensors can be effectively communicated to the surface, overcoming the barrier posed by the soil.

The integration of omnimedium communication into WSNs represents a significant advancement in sensor technology and its applications. By overcoming the traditional barriers of environmental attenuation, these networks can provide more reliable and timely data across a spectrum of disciplines. The future of WSNs equipped with omnimedium communication will be promising, with potential expansions into more fields and the capability to provide deeper insights into the hidden aspects of our world. This advancement not only enhances current applications but also opens new possibilities for scientific exploration and monitoring in previously inaccessible environments.

1.1.3 Challanges and Solutions

Omnimedium communication, despite its significant potential, encounters several complex challenges that must be addressed to realize its full capabilities. These challenges range from technical to practical, encompassing signal attenuation, power efficiency, and protocol design. Addressing these challenges is crucial for the successful deployment of omnimedium communication systems across diverse environments.

1. **High Attenuation of Traditional RF Signals:** One of the primary technical hurdles in omnimedium communication is the high attenuation of traditional RF signals, particularly in heterogeneous mediums like water and soil [15]. RF

signals tend to lose their strength over distance and when passing through materials that absorb or scatter electromagnetic waves. This attenuation can be severe in underwater and underground environments, where the signal degradation prevents effective long-range communication. To overcome this challenge, research is focused on developing new types of waveforms and utilizing different parts of the electromagnetic spectrum, such as acoustic waves and low-frequency electromagnetic waves. These innovative communication paradigms leverage the effective propagation of acoustic waves in non-air mediums and the deep penetration capabilities of low-frequency electromagnetic waves. These alternative strategies break barriers, reducing attenuation and enhancing signal penetration, thereby improving communication reliability and reach.

2. **Low Power Requirements:** The second major challenge is managing the low power requirements necessary for sustainable operation, especially in remote or inaccessible locations. WSN and SHM nodes, often placed in harsh or inaccessible environments, must operate over extended periods without frequent maintenance or battery replacements. Achieving low power consumption while maintaining effective communication is a complex balance. This necessitates using a refined communication scheme that enables efficient communication within and between various mediums while minimizing energy consumption and maintaining a compact size. Techniques such as passive backscatter communication, energy harvesting from environmental sources (solar, thermal, or vibrational energy), power-efficient communication protocols, and energy-saving operational modes are possible solutions. These strategies help ensure that sensors can collect and transmit data continuously without exhausting their power supplies prematurely.

3. **Communication Protocol Design:** Lastly, the design of adaptive communication protocols that can effectively function intra/inter different mediums presents a significant challenge. Traditional communication protocols are typi-

cally optimized for specific environments (e.g., WiFi, Bluetooth, LTE) and do not perform well in heterogeneous or dynamically changing conditions. Omnimedium communication requires protocols that can adapt to the variable characteristics of different transmission mediums, manage interference, reduce power consumption, and efficiently handle diverse data traffic patterns. Developing such protocols involves creating algorithms that dynamically adjust parameters like transmission power, frequency, and data rates based on the current environmental conditions and medium properties. Additionally, these protocols must ensure robustness and reliability in data transmission, addressing issues such as collision, error rates, and delays, which are more pronounced in challenging environments.

Addressing these challenges requires a multidisciplinary approach, combining advancements in materials science, electromagnetic theory, energy management, and network design. By tackling the high attenuation of signals, optimizing for low power usage, and designing flexible communication protocols, the implementation of omnimedium communication can be realized, paving the way for more robust and versatile applications across multiple fields.

1.2 Related Works and Contribution of this Thesis

In this thesis, we explore omnimedium communication through two distinct perspectives. Initially, we categorize it into two primary types: intra-medium and inter-medium communication.

Intra-medium communication pertains to communication within non-air mediums. Examples of this include interactions between underwater sensors or transmissions from surface to internal nodes in soil and concrete. This communication type focuses solely on single-medium environments where traditional RF signals are significantly

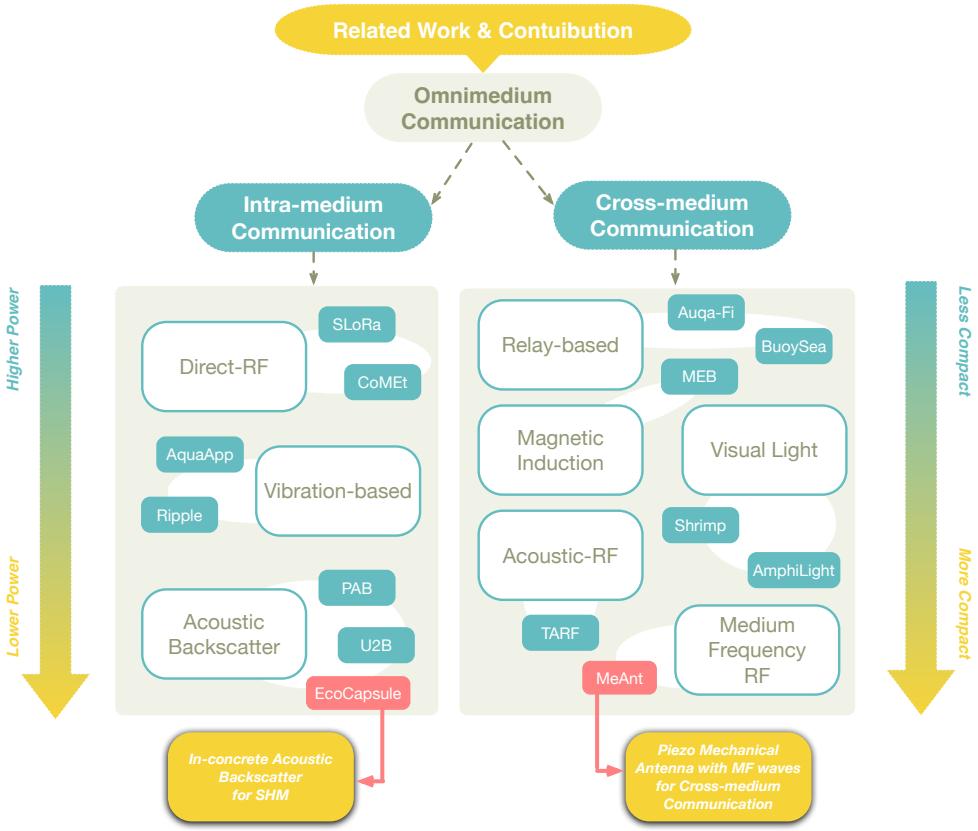

Fig. 1.2: Evolution of Omnimedium Communication: A Visual Representation. The red boxes present our proposed systems facilitating omnimedium communication in two different communication paradigms.

attenuated. Concurrently, we aim to minimize the power consumption of these communications and explore paradigms such as backscatter, which do not rely on internal batteries. Moreover, the nodes are designed to be compact to facilitate deployment and minimize environmental disruption. Existing research, as illustrated in Fig. 1.2, addresses these challenges. Direct-RF-based methods employ specific frequency bands and protocols that enhance penetration and reduce interference, enabling communication across longer distances in shallow water [16–18], thin concrete [19–22], or surface soil [23–25]. On the other hand, vibration-based methods utilize active acoustic vibrations for communication, capitalizing on the ability of acoustic waves to traverse solids [26] and liquids [27]. In contrast, the most recent development involves acoustic backscatter schemes [6, 28–32]. Similar to typical RF backscatter, these systems employ a transmission source to generate an acoustic wave, which is then converted into electrical energy by a piezoelectric transducer for storage. Then, the piezoelectric

transducer selectively reflects or absorbs the incoming acoustic wave for communication. Through this research, we introduce EcoCapsule, the inaugural SHM node that implements backscatter communication within concrete.

Another dimension of omnimedium communication is cross-medium communication, which involves transferring information between different physical environments, such as water [33], soil [34], concrete [35], and the human body [36], to the air. This communication mode has been extensively researched, as illustrated in Fig. 1.2. One commonly studied method is relay-based communication [37–39], which utilizes relay nodes positioned at the medium's boundary. These nodes facilitate the transmission of information in different mediums using two different methods: underwater communication employs acoustic waves, whereas air communication uses RF signals. Additionally, magnetic induction [40–43] and visible light-based [44–46] schemes leverage the penetrating abilities of magnetic field and light to achieve cross-medium communication. The acoustic-RF scheme [47, 48], on the other hand, utilizes millimeter waves to detect surface fluctuations caused by underwater acoustic vibrations. In this research branch, we introduce MeAnt, a pioneering approach to direct cross-medium communication. MeAnt utilizes a novel piezo-based mechanical antenna that emits medium-frequency electromagnetic waves capable of penetrating various mediums, thereby enabling direct cross-medium communication.

1.2.1 EcoCapsule: In-concrete Acoustic Backscatter Communication

The first work, EcoCapsule, explores the development of a novel SHM system using invented self-sensing concrete. The innovation, EcoCapsule, integrates battery-free, miniature piezoelectric backscatter sensors within the concrete to enable wireless communication and structural health monitoring without needing battery replacements or wired connections. This non-intrusive breakthrough addresses significant challenges

in the field of SHM, such as the high costs and maintenance difficulties associated with installing traditional intrusive wired SHM systems.

EcoCapsules are embedded in concrete structures during the construction phase and are designed to conduct SHM permanently without maintenance, providing long-term monitoring capabilities. The technology leverages the properties of piezoelectric materials, which can convert mechanical energy into electrical signals, to facilitate communication through the dense concrete medium, overcoming the limitations posed by the concrete's Faraday cage effect. This method is particularly suited to monitoring large-scale infrastructures like buildings and bridges where traditional monitoring techniques may be cumbersome or invasive.

The EcoCapsule confronts several significant challenges related to energy harvesting, multi-model body waves, and the durability of embedded sensors under extreme pressure. One primary obstacle is concrete's dense, electromagnetically impenetrability, which acts as a Faraday cage, severely impeding traditional radio frequency communication. The EcoCapsule addresses this by utilizing piezoelectric backscatter communication, where mechanical waves, rather than electromagnetic signals, carry data and transmit energy. These waves are less prone to attenuation in solid materials like concrete, thus ensuring reliable energy delivery and data transmission. Moreover, the energy harvesting mechanism within the EcoCapsule is finely tuned to harness mechanical vibrations effectively, converting them into electrical energy sufficient to power the sensor indefinitely, thus eliminating the need for battery replacement—a common drawback in traditional sensor systems. Another significant challenge is the physical pressure exerted by the surrounding concrete, which can damage internal components. The design counters this by encasing the electronics in a robust, stress-resistant shell that withstands high pressures while maintaining sensor sensitivity. This integration of innovative material use, energy-efficient design, and advanced communication techniques allows the EcoCapsule to operate continuously and autonomously, providing real-time monitoring without the need for internal

power sources or invasive maintenance, thereby offering a groundbreaking solution to the persistent challenges of in-situ structural health monitoring.

We present a detailed analysis of the EcoCapsule system's design, including its use of advanced signal processing techniques to handle the complex signal propagation characteristics in concrete. We conducted extensive real-world tests to validate the performance of the EcoCapsules, demonstrating their effectiveness in various concrete types and configurations. The results showed that the EcoCapsules could successfully transmit data on structural integrity, such as stress and strain, to external receivers, facilitating real-time health monitoring of the structures.

In conclusion, the EcoCapsule represents a significant advancement in the field of structural health monitoring, offering a scalable, non-intrusive, and cost-effective solution for long-term infrastructure monitoring. This technology has the potential to greatly enhance the safety and longevity of civil engineering structures, reducing the risk of unforeseen failures and extending their operational life.

1.2.2 MeAnt: Mechanical Antenna for Direct Cross-medium Communication

The second work presents MeAnt, a groundbreaking IoT platform engineered to enable seamless cross-medium communication leveraging miniature mechanical antennas known as Piezo-MAs. This innovation seeks to address the inherent limitations of traditional communication systems, particularly in challenging environments such as underwater, soil, and concrete, where conventional electromagnetic signals suffer significant attenuation and interference. The MeAnt platform operates on medium-frequency (MF) EM waves, facilitated by the novel use of Piezo-MAs, which bypass the need for large transmitting antennas by using mechanical motion to generate EM waves.

At the core of the MeAnt platform are the Piezo-MAs, which utilize piezoelectric materials to convert mechanical vibrations into radiative EM signals. This mechanism is advantageous in environments where traditional antennas are ineffective or impractical. By employing medium-frequency radio waves, MeAnt ensures robust penetration and lower attenuation across diverse mediums, which is pivotal for the IoE, facilitating communication across air, water, soil, and more.

We detail the technical challenges overcome by the MeAnt system, including the design of a full-stack communication protocol that mitigates interference from ambient signals (such as AM broadcasts) and ensures efficient data transmission despite the unidirectional nature of Piezo-MAs. The system employs advanced techniques like chirp spread spectrum (CSS) modulation at the physical layer and a novel carrier sense multiple access with collision avoidance (CSMA/CA) protocols at the link layer, which exploits the mechanical vibrations leakage of Piezo-MAs for carrier sensing. Moreover, MeAnt integrates polar codes at the transport layer to enhance data integrity in error-prone environments, leveraging their capacity-achieving performance and low computational complexity. This forward error correction technique is particularly suited to the harsh conditions encountered in cross-medium communications, ensuring reliable data transmission by correcting errors during signal propagation.

In conclusion, MeAnt represents a significant advancement in the field of cross-medium communications. Its ability to operate effectively across various transmission environments without the need for extensive physical infrastructure changes the paradigm of IoT networking, opening up new possibilities for applications ranging from underwater data collection to urban and industrial IoT deployments. The experimental results demonstrate MeAnt's efficacy, achieving communication over distances and through mediums previously challenging for traditional systems, thereby paving the way for its adoption in real-world IoE scenarios.

1.3 Thesis Organization

Based on the motivation and contributions outlined in this chapter, the subsequent chapters are organized as follows:

Chapter. 2 introduces the background of piezoelectricity. Specifically, we outline the piezoelectric effect's fundamental principles and discuss its application in omni-imedium communication technologies. Chapter. 3 introduces EcoCapsule, our innovative SHM hardware, covering the design motivations, challenges, realization, and extensive testing in real-world scenarios. Chapter. 4 details MeAnt, the piezoelectric-enabled mechanical antenna, and its applications in cross-medium communication. In Chapter 5, we reflect on the limitations of our current works, summarize the lessons learned, and explore directions for future research.

Chapter 2

Background of Piezoelectricity

In this chapter, we will elaborate on the fundamentals of piezoelectricity and how it empowers the omnimedium communication.

2.1 Piezoelectric Effect

When an electric field is applied to a dielectric crystal, electric charges accumulate on its surface. Additionally, certain dielectrics can accumulate charges when subjected to mechanical pressure. Materials that exhibit this characteristic are termed piezoelectrics, and this specific response is known as the direct piezoelectric effect (referenced in Fig. 2.1(a)). This effect was initially identified by the French physicists Pierre Curie and Jacques Curie (the Curie brothers) in 1880 [1]. They discovered that some materials, like quartz, produce electrical charges in response to pressure, and the amount of charge generated is directly related to the applied mechanical force. Concurrently, piezoelectric materials will undergo elastic expansion or compression when exposed to an electric field, a phenomenon called the converse piezoelectric effect (identified by Gabriel Lippmann in 1881), where the degree of deformation aligns with the strength of the electric field (shown in Fig. 2.1(b)). As a result, piezoelec-

tric materials are versatile and capable of converting mechanical energy to electrical energy and vice versa.

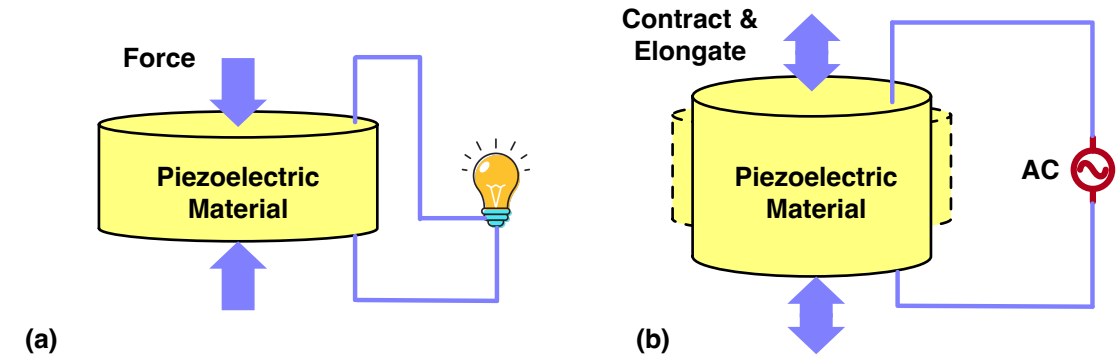

Fig. 2.1: Diagrams illustrating: (a) direct piezoelectric effect and (b) converse piezoelectric effect.

The piezoelectric effect is a fascinating phenomenon that underpins a wide range of applications in modern technology. At its core, the piezoelectric effect refers to the ability of certain materials to generate an electric charge in response to mechanical stress and vice versa. This property is not only intriguing from a scientific standpoint but also extremely useful in various engineering and technological fields.

The practical uses of the piezoelectric effect are vast and varied. In World War I, leveraging the piezoelectric effect, Paul Langevin and his team invented the first ultrasonic submarine detector, known as Langevin sonar, in 1917. This innovative device used a quartz crystal to send ultrasonic pulses for detecting submarines underwater, playing a critical role in the Atlantic campaign of World War II and representing a significant advancement in the development of piezoelectric materials.

In the realm of electronics, piezoelectric crystals are commonly used in quartz watches, where they regulate time by oscillating at a very stable frequency when an electric voltage is applied. This principle of precision oscillation underpins their use in various timing devices.

In medical technology, piezoelectric materials play a critical role. They are used in ultrasound equipment, generating sound waves that penetrate human tissues and reflect back to create images of organs and fetuses. This application leverages their ability

to rapidly oscillate under an electric current, producing sound waves at ultrasonic frequencies.

Moreover, the piezoelectric effect finds applications in more specialized fields like sensor technology and actuators. For example, piezoelectric sensors are capable of converting mechanical forces, such as pressure, sound waves, or acceleration, into electrical signals that can be measured and analyzed. Similarly, piezoelectric actuators convert electrical signals into precise physical movements, which is essential in optical instrumentation and precision engineering.

Additionally, energy harvesting is an emerging area where the piezoelectric effect is gaining traction. In this context, piezoelectric materials are used to convert energy from mechanical stress (such as vibrations, walking, or even vehicular movement) into electrical energy, providing a sustainable source of power for small electronic devices.

In conclusion, the piezoelectric effect is a remarkable natural property that has been harnessed to advance technology in many ways. From maintaining time in watches to facilitating complex medical diagnoses and enabling energy harvesting, the applications of this effect continue to grow and evolve, driven by ongoing research and innovation.

2.1.1 Piezoelectric Equations

In this section, we will formulate the piezoelectric effect to understand the complex stress-electricity conversion process of the materials. In general, the piezoelectric equations quantify the relationship between electric displacement (D), mechanical stress (T), electric field (E), and strain (S). Here, we suppose a cube crystal that exhibits piezoelectric effects.

Direct Piezoelectric Effect: The direct piezoelectric equation relates the electric

displacement D to mechanical stress T and electric field E:

$$D_i = d_{ijk}T_{jk} + \epsilon_{ij}E_j \tag{2.1}$$

Here, d_{ijk} are the piezoelectric coefficients, and ϵ_{ij} are the permittivity constants of the material measured at constant (or zero) stress. Subscripts i, j, k take the values 1,2,3 and define the three spatial dimensions of a cube crystal.

Converse Piezoelectric Effect: The converse piezoelectric equation describes how an applied electric field results in strain (S):

$$S_{ij} = d_{kji}E_k + s_{ijkl}T_{kl} \tag{2.2}$$

In this equation, S_{ij} is the strain, s_{ijkl} are the elastic compliance coefficients at constant electric field, T_{kl} is the stress, and E_k is the electric field. Similarly, i, j, k, and l are tensor indices that account for the directions and planes along which the stresses and strains act. In a three-dimensional space, these indices can take values from 1 to 3, corresponding to the three spatial dimensions (x, y, z).

Matrix Representation for Piezoelectric Relations: Often, the piezoelectric relations are expressed in matrix form for practical calculations. Note that the variables in the following equation possess distinct dimensional properties, signifying that the piezoelectric equations vary across different dimensional frameworks.

$$\begin{bmatrix} \mathbf{D} \\ \mathbf{S} \end{bmatrix} = \begin{bmatrix} \boldsymbol{\epsilon} & \mathbf{d} \\ \mathbf{d^T} & \mathbf{s} \end{bmatrix} \begin{bmatrix} \mathbf{E} \\ \mathbf{T} \end{bmatrix} \tag{2.3}$$

Here, $\mathbf{D}$ and $\mathbf{S}$ are vectors of electric displacement and strain, respectively, $\mathbf{E}$ and $\mathbf{T}$ are vectors of electric field and stress, $\boldsymbol{\epsilon}$ is the permittivity matrix, $\mathbf{d}$ is the piezoelectric matrix, and $\mathbf{s}$ is the compliance matrix.

In the parameters, the most important one is $\mathbf{d}$. The piezoelectric coefficient $\mathbf{d}$ for the direct and converse piezoelectric effects are thermodynamically equivalent and are generally represented in the units of pC $\cdot$N^{-1} and pm $\cdot$V^{-1}, respectively. This matrix

directly relates mechanical stress or strain to electric polarization (direct effect) or electric field to strain (converse effect). The elements of the **d** matrix indicate how sensitive a piezoelectric material is to mechanical stresses or electric fields. High values indicate a material that can generate significant electrical output from small mechanical stresses or significant mechanical response from small electric fields.

Electromechanical Coupling Factor: The electromechanical coupling factor, often denoted by k, is a critical parameter in piezoelectric materials, representing the efficiency of the conversion between electrical and mechanical energies. It quantifies how effectively a piezoelectric material can convert energy from one form to another. The k is defined as the square root of the ratio of the mechanical energy converted to electrical energy to the total mechanical energy supplied, or vice versa:

$$k = \sqrt{\frac{\text{Electrical Energy Converted to Mechanical Energy}}{\text{Electrical Energy Supplied}}} \tag{2.4}$$

$$= \sqrt{\frac{\text{Mechanical Energy Converted to Electrical Energy}}{\text{Mechanical Energy Supplied}}} \tag{2.5}$$

For specific modes of vibration (like thickness, radial, or longitudinal modes), the coupling factor can be expressed in terms of piezoelectric constants, dielectric constants, and elastic stiffness constants of this certain direction:

$$k^2 = \frac{d^2 c}{\epsilon s} \tag{2.6}$$

where d is the piezoelectric coefficient, c is the elastic stiffness at constant electric field, ϵ is the permittivity at constant strain, and s is the elastic compliance at constant electric field of this direction. This formula directly measures how much mechanical energy is converted into electrical energy and is particularly useful for designing piezoelectric devices such as sensors and actuators.

Summarization: The suite of equations related to piezoelectric materials encapsulates a comprehensive mathematical framework for understanding and predicting the behavior of these unique substances, which can convert mechanical energy into electrical energy and vice versa. The piezoelectric matrix **d**, which relates the mechanical

stress and electric displacement, and the elastic compliance $\mathbf{s}$, which connects stress to strain under constant electric fields, are central to modeling the direct and converse piezoelectric effects. This interrelationship is quantified through the piezoelectric coefficients that determine how efficiently a material can respond to mechanical stimuli by generating electrical signals or deform mechanically when subjected to electric fields. The coupling factor k, a measure of the conversion efficiency between electrical and mechanical energies, further enriches the design and analysis of piezoelectric devices by highlighting the efficiency of energy transfer inherent to specific materials and vibration modes.

From practical applications ranging from communication sensors to energy harvesters, these equations are indispensable. They allow engineers and designers to estimate critical performance metrics such as resonant frequencies, energy conversion efficiencies, and the overall responsiveness of piezoelectric materials. By understanding and applying these relationships, one can optimize piezoelectric devices' material selection and structural design to enhance their performance and suitability for various applications. The calculation of k values for different modes of operation, for instance, guides the creation of more effective and precisely tuned piezoelectric devices, ensuring maximal operational efficiency and energy utilization. This mathematical groundwork not only supports the ongoing innovation within piezoelectric technology but also aids in the exploration of new applications where energy conversion and mechanical-electrical interplay are crucial.

2.2 Piezoelectric Materials

In the above section, we have figured out some basic principles of piezoelectricity; now, we want to explore what materials hold this unique characteristic.

The journey into piezoelectric materials began in the late 19th century, with the

discovery of the piezoelectric effect by the Curie brothers, Jacques and Pierre, in 1880. They found that certain crystals, such as quartz and Rochelle salt, generate an electric charge when subjected to mechanical stress. This groundbreaking discovery laid the foundational principles for piezoelectricity, opening up new avenues in science and technology.

As research progressed, the early 20th century saw the development of the first practical applications of piezoelectric materials. During World War I, the piezoelectric effect was utilized in sonar devices, demonstrating its significant potential. The materials used at this time, primarily quartz and Rochelle salt, were limited by their piezoelectric properties and environmental stability, which prompted researchers to seek more robust and versatile alternatives. The quest for materials with enhanced piezoelectric properties led to the synthesis of Barium Titanate ($BaTiO_3$) in the 1940s. This material exhibited strong piezoelectric effects and better temperature stability than natural piezoelectric materials, marking a significant advancement in the field.

However, it was the development of Lead Zirconate Titanate (PZT) in the 1950s that revolutionized piezoelectric technology. PZT, a ceramic perovskite material that can be altered at the atomic level to tailor its piezoelectric properties, offered superior performance in terms of its electromechanical coupling coefficients and its ability to operate over a wider range of temperatures and frequencies. The versatility and enhanced properties of PZT opened up new possibilities in a variety of applications, ranging from everyday consumer electronics to sophisticated aerospace components. It became the material of choice for actuators, sensors, and energy harvesting devices, setting a new standard in the field of piezoelectric materials. The development of PZT not only marked a pivotal moment in the advancement of piezoelectric materials but also underscored the importance of material science in pushing the boundaries of technological innovation.

2.2.1 Chemical Structure and Synthesis of PZT

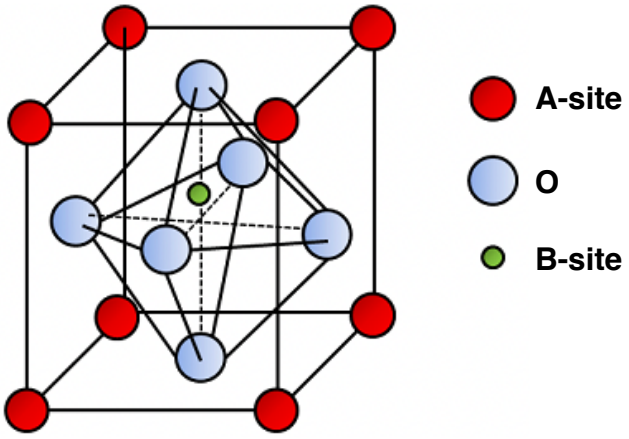

Fig. 2.2: PZT perovskite structure.

PZT is a ferroelectric material and a kind of perovskite. The perovskite crystal structure is pivotal in piezo- and ferroelectric materials due to its exemplary performance, notably exemplified by the PZT solid solution. Named after the mineral calcium titanate ($CaTiO_3$), perovskite structures adopt the general chemical formula ABO_3. Here, 'O' stands for oxygen, 'A' represents a larger cation with a coordination number of 12 and a valence ranging from +1 to +3 (examples include K^+, Pb^{2+}, and Bi^{3+}), while 'B' is a smaller cation with a valence ranging from +3 to +5 (such as Fe^{3+}, Ti^{4+}, and Nb^{5+}). Fig. 2.2 shows the typical perovskite structures of the PZT.

In perovskite structures like PZT, which are noncentrosymmetric, each unit cell inherently possesses a net nonzero charge. This charge distribution becomes polarized due to the B-site ion (e.g., Ti^{4+}) being slightly offset from the center of the unit cell, effectively creating an electric dipole within each cell. Mechanical stress applied to the crystal can alter the position of the B-site ion, thereby modifying the crystal's polarization strength—this phenomenon underlies the direct piezoelectric effect. Conversely, when an electric field is applied, it induces a shift in the B-site ion's position, which distorts the unit cell, typically making it more or less tetragonal in shape. This structural change is the basis of the converse piezoelectric effect.

2.2.2 Poling the PZT

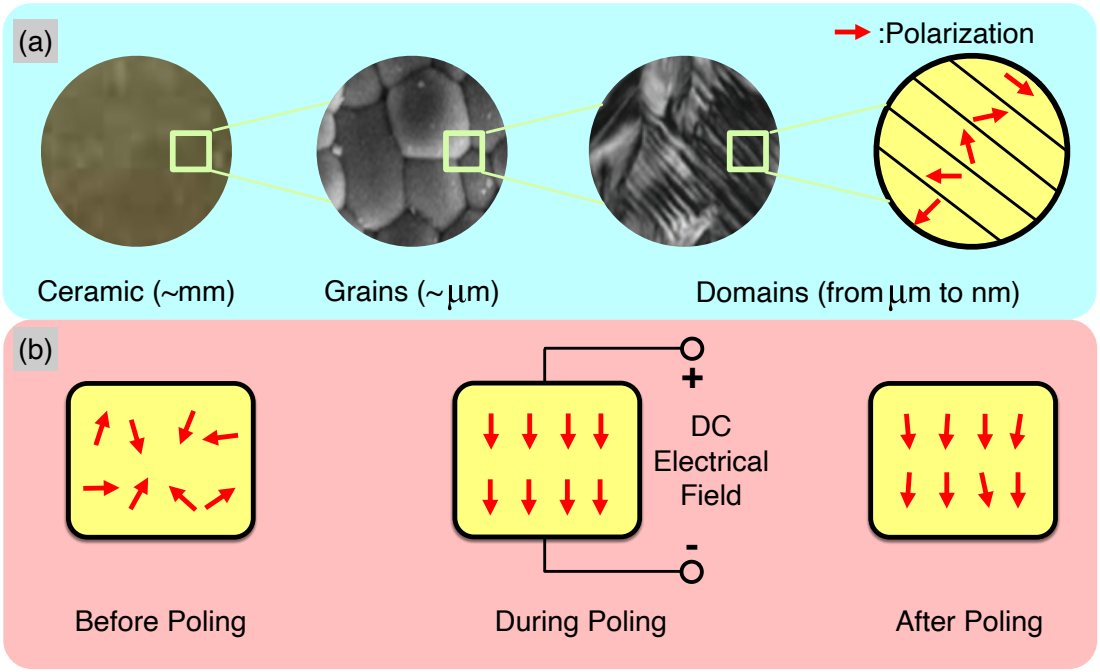

Fig. 2.3: Polarization Distributions: (a) grains and domains in piezoelectric ceramics, and (b) domain reorientation after poling. The microscope photos are reproduced from [1].

In a macroscopic crystalline structure composed of numerous unit cells, the inherent dipoles within each cell are typically found in a random orientation under natural conditions. This random arrangement results in a zero net polarization, meaning the piezoelectric effect is minimal under normal circumstances. When mechanical stress is applied to such a material, it induces a rotation in these dipoles, aligning them towards a direction that optimally reduces the overall electrical and mechanical energy stored within them. However, this induced alignment does not significantly alter the material's macroscopic polarization without initial uniform orientation.

To enhance the piezoelectric effect, it is crucial to establish an initial uniform alignment of the dipoles. This is achieved through a process called poling, where the material is subjected to a high electric field that aligns the dipoles in the direction of the applied field. After removing the electric field, most dipoles retain their new orientation due to the pinning effect, which is caused by microscopic defects within the crystal lattice that inhibit the dipoles' return to their original random positions. This

alignment retention prepares the material to exhibit a strong piezoelectric response upon subsequent mechanical stressing.

It's important to note that the material can lose this alignment under certain conditions, known as depoling [49]. Depoling can occur if the material is exposed to a high electric field opposite to the original poling direction, or if it is heated beyond the Curie temperature of the material. Beyond the Curie temperature, the material undergoes a phase transition that disrupts the dipole alignment, effectively erasing the induced piezoelectric properties until it is poled again. Thus, the piezoelectric properties of a material depend not only on the crystals' intrinsic characteristics but also on the manipulation and stability of the dipole orientations within those crystals.

2.2.3 PZT Equivalent Circuit and Resonant Frequency

In the field of engineering, the frequency characteristics of piezoelectric materials such as PZT are crucial, as they directly influence the material's suitability for specific applications [50]. Understanding these frequency responses allows engineers to tailor PZT properties to enhance device performance and efficiency in various technologies, ranging from sensors to actuators. This section explores the frequency response of typical PZT materials, examining the underlying mechanisms that shape these responses and their practical implications.

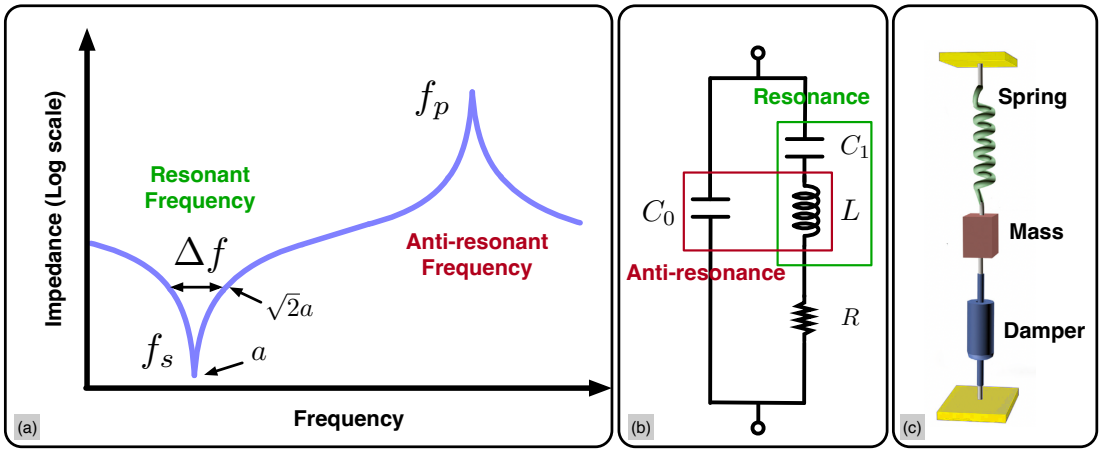

Fig. 2.4: The Resonance and Equivalence of PZT: (a) The resonant and anti-resonant frequencies of the PZT. (b) The BVD equivalent circuit of the PZT. (c) The equivalent physical model of the PZT.

Fig. 2.4(a) shows the typical impedance of the PZT plotted on a logarithmic scale against frequency. The graph highlights two significant points: the resonant frequency (f_s) and the anti-resonant frequency (f_p). The resonant frequency is where the impedance of the PZT reaches a minimum, indicating maximum energy transfer from the electrical to mechanical system, thus maximum vibration. The anti-resonant frequency is where the impedance peaks, indicating minimal energy transfer. The resonant frequency is of paramount importance in practical applications. At this frequency, the PZT exhibits maximum energy efficiency, channeling the electrical input into mechanical output with minimal losses. This characteristic is particularly critical in applications requiring high precision and efficiency, such as ultrasonic transducers in communication or medical imaging, where high vibration amplitudes at resonant frequencies enhance penetration depth and image resolution.

But why does the PZT present the two specific frequencies? We will explain it with the Butterworth-Van Dyke (BVD) equivalent circuit [51], a widely accepted model for representing the dynamic behavior of piezoelectric materials. The BVD model simplifies the complex interactions within the PZT into manageable electrical components that mimic its mechanical and electrical responses.

For a typical piezoelectric material modeled using a BVD equivalent circuit (Fig. 2.4(b)), the BVD equivalent circuit comprises a parallel capacitor C_0, representing the static capacitance of the PZT, and a series branch of a resistor R, an inductor L, and a capacitor C_1. The resistor R models the internal mechanical losses (damping), the inductor L represents the mass or inertia of the piezoelectric material, and the capacitor C_1 simulates the compliance (flexibility or elasticity) of the material.

Resonant Frequency (f_s): This is the frequency at which the impedance of the circuit is at its minimum, primarily influenced by the series resonance of the inductor L and capacitor C_1. The formula for the resonant frequency should be:

$$f_s = \frac{1}{2\pi\sqrt{LC_1}} \tag{2.7}$$

Anti-Resonant Frequency (f_p): This frequency occurs when the total impedance of the circuit is maximized. This typically involves the interaction of C_1 and L along with the effect of the shunt capacitor C_0. The formula reflects the combined effects of C_0 and C_1, typically resulting in a formula:

$$f_p = \frac{1}{2\pi\sqrt{L\left(\frac{C_0 C_1}{C_0+C_1}\right)}} \tag{2.8}$$

Relationship with Electromechanical Coupling Factor (k^2): Recall that the k^2 is the conversion efficiency between electrical and mechanical energies. Essentially, k^2 has the following relationship with the BVD equivalent circuit parameters:

$$k^2 = \frac{f_p^2 - f_s^2}{f_p^2} = \frac{1}{1+\frac{C_0}{C_1}} \tag{2.9}$$

This expression essentially represents the fraction of the stored energy in the piezoelectric device that contributes to the piezoelectric effect ($f_p^2 - f_s^2$) versus the total energy stored in the device (f_p^2). Meanwhile, the ratio $\frac{C_0}{C_1}$ is usually denoted as capacitance ratio, which reflects the sensitivity of the PZT.

Mechanical Quality Factor (Q): The Mechanical Quality Factor, commonly denoted as Q, is a fundamental parameter used to describe the performance of resonant systems, including mechanical and electronic oscillators such as piezoelectric devices. Q is defined as the ratio of the resonant frequency f_s to the bandwidth Δf, where Δf is the difference between the frequencies at which the power falls to half its peak value. Mathematically, it is expressed as:

$$Q = \frac{f_s}{\Delta f} \tag{2.10}$$

This formula encapsulates the system's damping characteristics; a higher Q indicates lower energy dissipation relative to the stored energy, which indicates a system that can sustain oscillations for a longer period with minimal energy input.

In practical terms, a high Q value in a piezoelectric device means that the device is highly efficient at its resonant frequency, with minimal energy loss to heat or other

forms of dissipation. This is particularly desirable in applications such as high-power transducers or antennas where selectivity and stability are crucial.

In contrast, a low Q factor indicates a broader resonance peak, which benefits applications with a wider operational bandwidth. This might be essential in sensors operating effectively across a range of frequencies or in damping applications where quick energy dissipation is necessary.

2.2.4 PZT Fabrication

Fabrication of PZT Transducers involves a series of precise and controlled processes, which are crucial for achieving the desired electrical and mechanical properties in the final product. The process typically begins with preparing the piezoelectric ceramic material, primarily composed of lead zirconate titanate. This material is synthesized from a mixture of lead oxide, zirconium oxide, and titanium oxide, with various dopants that can be added to tailor the material's properties.

The raw materials are first weighed and mixed to achieve a uniform distribution of constituents. This mixture is then calcined at high temperatures to achieve the desired phase and chemical homogeneity. Following calcination, the material is ball-milled to form a fine powder, which is then pressed into disks or other desired shapes under high pressure. These green bodies are sintered at elevated temperatures to enhance their density and mechanical strength, effectively forming the piezoceramic.

Post-sintering, the ceramic undergoes electrode deposition, where metallic coatings are applied to the surfaces to enable electrical connectivity. Common electrode materials include silver, gold, or nickel. These electrodes are crucial as they directly influence the efficiency of the piezoelectric effect by facilitating the application and collection of electrical charges.

The choice of materials and specific ratios in the fabrication process are directly

related to the key parameters of the PZT, such as the electromechanical coupling factor (k^2), resonant and anti-resonant frequencies (f_s and f_p), and the mechanical quality factor (Q). For instance, the type and amount of dopant used can significantly affect the piezoelectric and dielectric properties of the ceramic, thereby altering C_0 and C_1 in the BVD model, which in turn influences k^2 and the frequencies.

In practical applications, the fabrication details dictate the performance of the PZT in its final use environment. For example, in medical imaging applications, a high k^2 value is preferred for better energy conversion, necessitating specific material compositions and processing techniques that enhance this parameter. Similarly, for applications requiring high precision and stability, such as in frequency filters or sensors, the quality of the electrodes and the sintering conditions must be meticulously controlled to achieve high Q values and precise resonant characteristics.

In conclusion, the fabrication of PZTs is a complex interplay of material science, chemical engineering, and precision manufacturing, with each step and choice crucial for tailoring the device's properties to meet specific application needs. The understanding of how these fabrication steps affect the fundamental parameters of the PZT allows engineers and scientists to innovate and optimize piezoelectric devices for a broad spectrum of technological applications, from everyday electronic devices to critical medical and industrial instruments.

Chapter 3

In-concrete Backscatter Network for SHM

3.1 Introduction

On June 24, 2021, Champlain Towers South, a 12-story beachfront condominium in the Miami suburb of Surfside, Florida, USA, partially collapsed. This tragic event resulted in 98 fatalities and garnered global attention [52]. Investigations revealed that the primary cause of the collapse was the degradation of reinforced concrete structural supports in the ground-level parking garage beneath the residential units. This degradation stemmed from water penetration and subsequent corrosion of the reinforcing steel. In today's world, the integrity of architectural structures, especially historical buildings several centuries ago, is crucial for safety and dependability. However, aging and environmental impacts inevitably deteriorate concrete structures. The most effective strategy to prevent sudden collapses is to implement SHM, which involves an automated sensing system to continuously assess the health of a structure.

SHM offers a viable means to ensure the integrity and safety of civil infrastructures by detecting damage progression and estimating performance deterioration. The

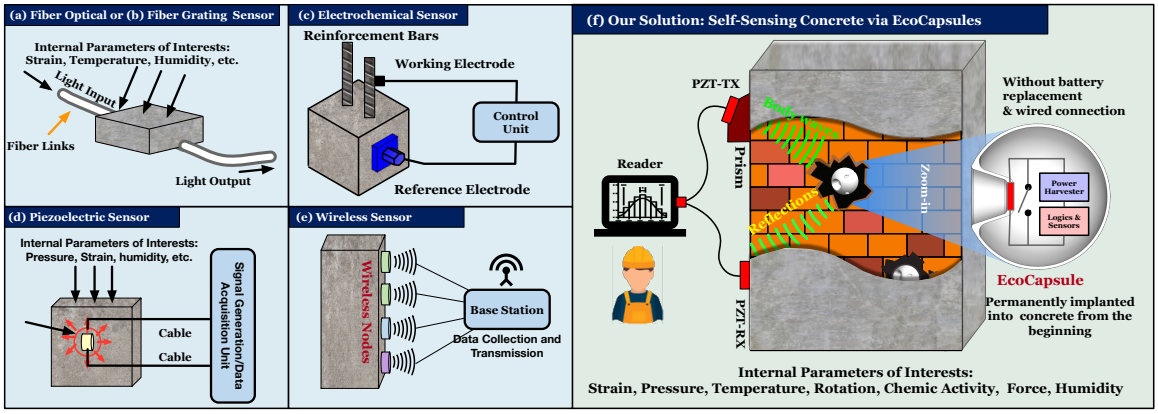

Fig. 3.1: Sensing Solutions for SHM. (a) - (e) shows the traditional sensing solutions by using fiber optical or fiber grating sensors, electrochemical sensors, piezoelectric sensors, and wireless sensors; (f) shows our solution where EcoCapsules are mixed into concrete when the walls are being built. Afterward, the operator can intrusively attach the transmitting and receiving PZTs onto the wall to communicate with the EcoCapsules implanted early, thereby acquiring the SHM-related data from the sensors integrated within the EcoCapsules.

concept of SHM, although not new, aims to realize the long-standing vision of real-time structural assessment. Early detection of risks through SHM can promptly prevent further structural deviation and damage. In civil engineering, four sensing solutions are predominantly used for SHM [53], as illustrated in Fig. 3.1:

(a) Fiber optic sensors utilize the principle of light modulation within optical fibers to detect and measure mechanical changes such as deformations or cracks within the structure. These sensors are highly sensitive, capable of detecting minute changes, and are beneficial for long-term monitoring due to their durability and resistance to harsh environmental conditions;

(b) Fiber Bragg grating sensors exploit changes in light signal characteristics transmitted through fibers embedded in concrete to detect various structural parameters, such as pressure, strain, humidity, rotation, and chemical interactions, etc.;

(c) Electrochemical sensors measure the potential difference between two electrodes—one mounted on a reference point and the other on internal steel—to detect the

presence or concentration of specific chemical elements and monitor chemical activity;

(d) Piezoelectric sensors, introduced in the early 1880s, capture variations in acoustic emission, temperature, strain, force, pressure, or acceleration, thus aiding in the assessment of structural criteria [54].

The traditional SHM solutions discussed previously are *intrusive* due to the necessity of *cables* for connecting sensors embedded within the concrete. These methods suffer from several drawbacks: the inconvenience of wired connections for power and data acquisition, high costs, and limited monitoring regions constrained by the reach of cables. Consequently, such systems are predominantly deployed in high-value infrastructures like bridges and skyscrapers, limiting broader application in routine civil structures.

An RF-based Wireless Sensor Network (WSN) has been proposed as a promising alternative, potentially eliminating the dependency on cables [55]. Nevertheless, the practical deployment of WSN for SHM remains sparse primarily for two reasons. Firstly, the sensor nodes, being battery-driven, require regular battery replacements, which could disrupt the structural integrity or limit sensor placement. Secondly, the composition of reinforced concrete—sand, water, and steel—creates a natural Faraday cage, impeding RF signal transmission and thereby relegating WSN nodes to surface attachment only, as illustrated in Fig. 3.1(e). This limitation prevents them from monitoring the internal structure, which is often more crucial than surface characteristics.

In recent developments, architectural experts have envisioned the use of self-sensing concrete that incorporates minor functional fillers into the mix, enabling an externally modifiable and responsive wireless network within the concrete itself. In this chapter, our research advances this innovative idea by introducing a battery-free, computable, and connectable piezoelectric backscatter sensor named EcoCapsule. This

cost-effective sensor is small enough to be mixed directly with cement, sand, water, and other materials during the construction phase, allowing it to be permanently embedded within the structure without the need for subsequent maintenance, thus preserving the structural integrity throughout the building's lifespan. As depicted in Fig. 3.1(f), to measure critical structural parameters like strain or acceleration, operators attach transmitting and receiving PZTs on the building's surface. The transmitting PZTs generate well-designed elastic waves that penetrate the concrete to power and activate the EcoCapsules for data collection and communication. The EcoCapsules then utilize backscatter communication techniques—reflecting or not reflecting the elastic waves—to modulate and transmit data, representing bit ones or zeros.

Piezoelectric backscatter systems (PBSs) have demonstrated their efficacy in underwater communication scenarios [28, 31]. Yet, their applicability within solid media, such as concrete, is less certain. Deploying PBS for wireless communication in solids poses significant challenges due to the distinct nature of wave propagation compared to liquids:

• **Wave Propagation Complexity:** Elastic waves in solid materials like concrete propagate with greater complexity than in liquid environments, such as water. In liquids, elastic waves typically propagate in a *single* mode, whereas in solids, multiple modes (five or more) are activated. This multimodality leads to various copies of the wave traveling at different speeds and forms, causing severe intra-symbol interference at the receiver (e.g., EcoCapsule), which complicates energy harvesting and symbol decoding. Our approach involves characterizing the signal propagation in concrete and introducing a *wave prism* that selectively filters out unnecessary modes while retaining the S-wave as the primary carrier.

• **Inter-symbol Interference Management:** In the downlink, the reader modulates bits (one or zero) using PIE encoded On/Off Keying (OOK). However, even after deactivation, a PZT may continue to vibrate due to inertia, leading to bit tailing

and additional inter-symbol interference. To address this, we leverage the resonance effects and employ dual-frequency-based Frequency Shift Keying (FSK) to emulate the OOK at the receiver end. By operating the PZT at resonant or non-resonant frequencies, we ensure that non-resonant frequencies are naturally attenuated by the concrete, allowing EcoCapsule nodes to distinguish between high and low-amplitude bits akin to OOK encoded bits.

• **Handling High External Pressure:** The external pressure exerted on an EcoCapsule embedded in concrete is approximately 2.4× greater than that experienced underwater at equivalent depths. To mitigate this, we design spherical, stressless shells to protect the internal circuitry from cracking or deformation under pressure. Additionally, we integrate a Helmholtz resonator array (HRA) at the front of the receiving PZT within each EcoCapsule to enhance wave amplification.

Summary of Results: We have prototyped numerous EcoCapsules, each featuring a mechanically engineered PZT, an HRA, and a custom-designed motherboard that includes an energy harvesting unit, a microcontroller, and an extensible peripheral interface for integrating various sensors (e.g., strain, temperature, and humidity). Our experimental results confirm that EcoCapsules embedded within real-life concrete structures can be effectively powered up and maintain wireless connectivity through continuous body waves (CBW). We achieved a maximum power-up range exceeding 6 meters and data throughput of up to 13 kbps. The technology has been successfully implemented in various concrete types, including ultra-high-performance fiber-reinforced concrete (UHPFRC) with a compressive strength of up to 215 MPa, underscored by our stressless shell design. Furthermore, we conducted a 17-month pilot study on the structural health monitoring of an operational footbridge, demonstrating the long-term viability of our system.

Contributions: This study pioneers the deployment of backscatter systems within concrete environments for wireless charging, communication, and sensing, overcoming longstanding challenges in SHM. Collaboration with civil engineering experts has

yielded a novel prototype and insightful long-term pilot studies, marking significant advancements in the field.

3.2 Background and Related Works

This section introduces the background knowledge about piezo-acoustic backscatter communication.

3.2.1 Piezo-acoustic Backscatter System

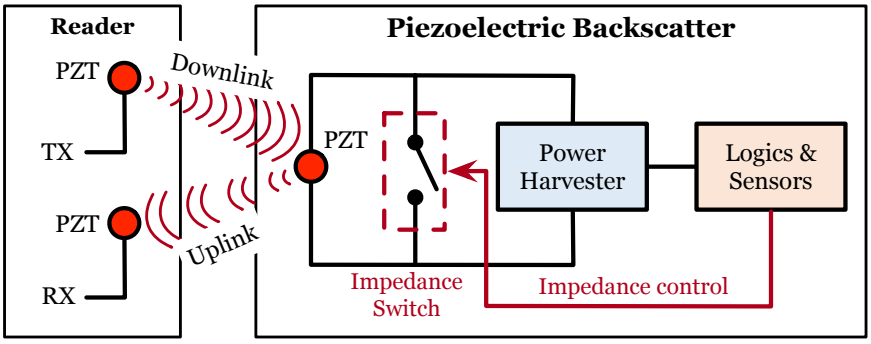

Fig. 3.2: Illustration of a PBS. An EcoCapsule communicates bits of zero and one by controlling the piezoelectric impedance switch, making the node either in absorptive or in reflective states.

A Piezoelectric Backscatter System (PBS) utilizes the piezoelectric effect to facilitate a battery-free wireless network employing backscatter-based communication, akin to RF backscatter systems used in RFID technology. The PBS comprises two principal components as illustrated in Fig. 3.2: a reader and backscatter nodes, which function similarly to RFID readers and tags, respectively. The reader features two PZTs; the transmitter (TX) generates a continuous ultrasonic wave, while the receiver (RX) collects responses from the backscatter nodes.

Each piezoelectric backscatter node is equipped with a single PZT, an impedance switch, a power harvesting unit, and integrated logic and sensor circuitry. The node's impedance switch, controlled by its logic circuit, toggles between two states: absorp-

tive and reflective. Specifically, if the PZT's terminals are shorted, the node is in the reflective state and reflects incoming elastic waves. Conversely, if the terminals are open, the node enters the absorptive state, converting the incoming elastic wave into electrical energy. Therefore, by altering the PZT's impedance (shorted or open), backscatter communication is facilitated.

The underlying mechanism of how changing the impedance at the PZT's terminals enables toggling between absorptive and reflective states hinges on the piezoelectric effect, which can be mathematically described as follows:

$$\underbrace{D}_{\text{charge displacement}} = \underbrace{dT}_{\text{mechanical}} + \underbrace{\epsilon^T E}_{\text{electrical}} \tag{3.1}$$

Here, an applied electric field (E) or mechanical stress (T) induces a charge displacement (D) at the PZT's terminals. The coefficients d and ϵ^T represent the piezoelectric and permittivity coefficients under constant stress, respectively. In an open state, the mechanical energy (T) will be converted into electrical energy (E). In a shorted state, both potential difference and charge at the PZT terminals are absent (D and E are zero), meaning no mechanical stress (T) is present. As a result, an incident mechanical wave encountering the PZT is fully reflected, maintaining a zero *net* tensor (T), indicative of the reflective state in backscatter communication. By alternating the terminal connections between short and open, we can effectively control the PZT's reflective and absorptive properties.

Typically, in a backscatter node, the switch remains open by default, keeping the node in an absorptive state to maximize power harvesting until the MCU is activated. Once powered, communication between the reader and backscatter begins, facilitated through two links: the downlink (reader to backscatter) and the uplink (backscatter to the reader). In the uplink, the backscatter alternates between absorptive and reflective states to modulate bits zero and one. Effectively acting as a mirror, the backscatter node employs its PZT to either reflect or absorb signals, thereby achieving straightforward OOK-based communication.

3.2.2 Elastic Wave in Solid Materials

When a PZT is affixed to a fixed material and voltage is applied, it vibrates accordingly. This vibration propagates as complex multi-mode elastic waves through the solid, with their nature and classification depending on the angle of incidence and the sound speed in the medium. They can be divided into two broad categories: body waves and surface waves. Surface waves propagate along the surface of the medium, while body waves propagate inside the medium. In our research, we focus primarily on body waves. Body waves are seismic waves that propagate through the interior of the Earth, unlike surface waves that travel along the Earth's surface. There are two principal types of body waves: P-waves (primary waves) and S-waves (secondary waves).

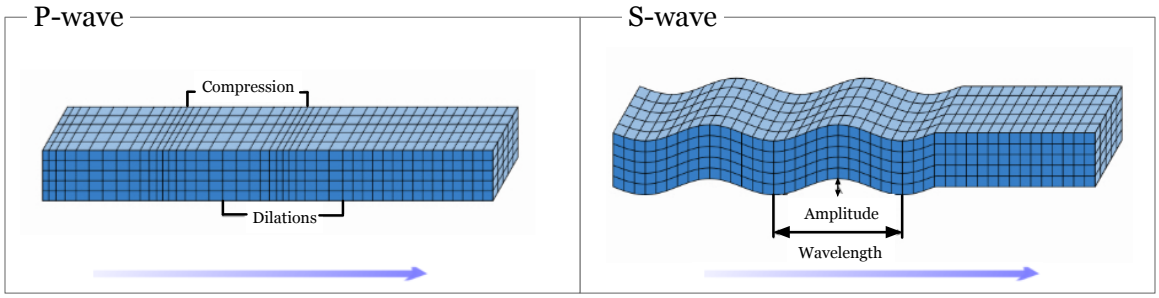

Fig. 3.3: Illustration of P-waves and S-waves propagation as body waves.

P-waves are longitudinal waves that compress and expand the material in the direction of wave propagation. These are the fastest type of seismic waves, traveling through solids, liquids, and gases at speeds ranging from 6 km/s to 14 km/s, depending on the material's density and elastic properties. S-waves, in contrast, are transverse waves that oscillate the material perpendicular to the direction of wave propagation. These waves cannot travel through liquids or gases as they require shear strength to propagate, and their speed is generally slower than that of P-waves, typically ranging from 3 km/s to 8 km/s in solids.

Fig. 3.3 graphically represents the propagation of P-waves and S-waves. P-waves,

characterized by their push-pull motion, can travel through all mediums and are relatively easier to attenuate, whereas S-waves, moving in an up-and-down motion, can only propagate through solids and tend to travel further due to their slower attenuation.

Below is the mathematical representation of body wave propagation in homogeneous media, where $\mathbf{u}$ denotes the displacement, ρ the density, and λ and μ the Lamé parameters. The governing equation for momentum in a body wave can be expressed as:

$$\rho\ddot{\mathbf{u}} = (\lambda + 2\mu)\nabla\nabla \cdot \mathbf{u} - \mu\nabla \times \nabla \times \mathbf{u}. \tag{3.2}$$

P-waves and S-waves are actually two solutions to this equation. To derive separate solutions for P-waves and S-waves, we apply vector operations. For P-waves, the equation simplifies to:

$$\nabla^2(\nabla \cdot \mathbf{u}) - \frac{1}{\alpha^2}\frac{\partial^2(\nabla \cdot \mathbf{u})}{\partial t^2} = 0, \tag{3.3}$$

where α, the velocity of P-waves, is defined by:

$$\alpha = \sqrt{\frac{\lambda + 2\mu}{\rho}}. \tag{3.4}$$

The equation for S-waves, governed by shear deformations, is:

$$\nabla^2(\nabla \times \mathbf{u}) - \frac{1}{\beta^2}\frac{\partial^2(\nabla \times \mathbf{u})}{\partial t^2} = 0, \tag{3.5}$$

with β, the S-wave velocity, calculated as:

$$\beta = \sqrt{\frac{\mu}{\rho}}. \tag{3.6}$$

3.2.3 Related Work

Our work builds upon and extends research in several established fields:

(1) Acoustic Communication and Sensing: Acoustic waves have been extensively utilized for data transmission and environmental sensing in air [56,57], solids [58–64], and water [28, 65] to overcome the limitations posed by traditional wired or RF communication methods. Previous systems in solid media often required the deployment of acoustic transceivers either on the object's surface [60, 61, 66] or invasively inserting wired transceivers into materials like concrete [59], potentially compromising structural integrity. In contrast, EcoCapsule represents a significant advancement by embedding battery-free sensors directly within concrete, facilitating robust wireless connections with ultra-low power consumption.

(2) Backscatter Systems: Backscatter communication has seen increasing interest for its ability to harness the energy and enable communication via RF signals [67–69], light [70], and magnetic fields [71], with applications spanning over-the-air connectivity [67], underwater exploration [28, 31], and in-body communications [72]. EcoCapsule advances this technology by adapting it for use within solid-state materials, a novel approach not previously explored. This adaptation requires addressing specific challenges related to wireless charging and communication in environments where elastic waves exhibit multiple modes. Additionally, the EcoCapsule must withstand the harsh conditions of its operating environment, addressing significant structural challenges not faced by previous systems.

(3) Structural Health Monitoring: Our work also relates closely to extensive research in SHM, which typically categorizes systems into surface-mounted sensors, intrusive wired sensors, and wireless-connected embedded sensors. Surface-mounted sensors monitor structural health using technologies such as RF Radar [73], electrical signals [74], and acoustic waves [58]. While non-destructive, these methods often lack the sensitivity to detect minor internal changes like strain or humidity. Intrusive wired systems offer greater accuracy by directly interfacing with embedded sensors [75] or internal smart materials [76, 77]; however, their deployment can compromise structural integrity, limiting real-world applicability. Recent attempts

to implement RF-connected sensors [78–80] have faced challenges due to the severe attenuation of RF signals within concrete and the impractical size of RF antennas for embedding. EcoCapsule introduces a groundbreaking solution to these dilemmas by utilizing solid backscatter communication, enhancing the accuracy, flexibility, and scalability of SHM practices.

3.3 Wireless Charging and Wireless Communication in Concrete

The implementation of the PBS within the interior of solid materials marks a pioneering advancement. This section begins by delineating the characteristics of the wireless media employed—elastic waves—and subsequently addresses three fundamental issues crucial to the deployment of this technology.

3.3.1 Wireless Media: Elastic Waves

Elastic waves are disturbances that propagate through both solid and fluid materials, including surfaces, without inducing permanent structural or physical alterations. These waves manifest in various forms, each with distinct properties, and are broadly categorized into two main types: body waves and surface waves. Body waves traverse the interior of the media, making them particularly relevant for applications like EcoCapsule, where sensors are embedded deeply within concrete structures.

Body waves propagate in three dimensions and are capable of moving through the entire volume of a solid. These waves consist of two primary modes, illustrated in Fig. 3.3. The first mode, known as the primary wave or P-wave, compresses and expands the medium it travels through. P-waves are capable of moving through both solid and liquid materials, with their velocity varying depending on the medium's

properties. The second mode, known as the secondary wave or S-wave, generates a transverse waveform that shears the material sideways at right angles to the wave's direction of travel. Because liquids cannot support shear stresses, S-waves are absent in underwater environments, which simplifies the implementation of PBS systems in such settings.

Each mode of the body wave can be conceptualized as a distinct copy of the originating wave, differing in waveform and velocity. Notably, S-waves travel at a speed approximately 40% slower than that of P-waves within solid materials. For instance, the velocities of P-waves and S-waves in concrete are approximately $C_p = 3338\,\mathrm{m/s}$ and $C_s = 1941\,\mathrm{m/s}$, respectively [81]. Moreover, the attenuation coefficient for S-waves is significantly lower than that for P-waves [82], which implies that S-waves can propagate further within the medium. Given these characteristics, S-waves are considered preferable for wireless communication media in applications such as ours, where communication range and signal integrity are crucial.

3.3.2 Wireless Charging

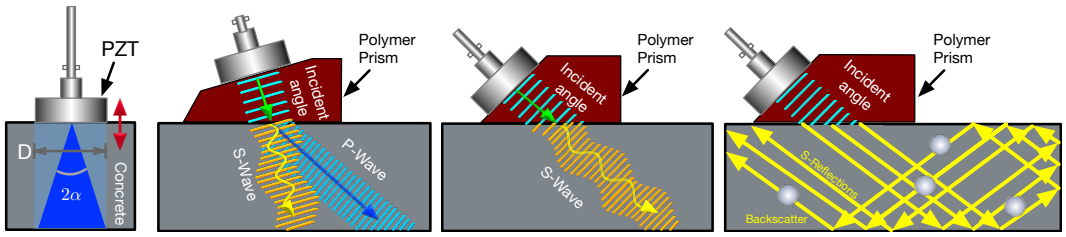

(a) 0° incidence (b) 15° incidence (c) 40° incidence (d) Wireless charging with S-reflections

Fig. 3.4: Injecting elastic waves into concrete with different means. (a) Transmission of body wave at a perpendicular plane boundary. (b) Both modes of body wave exist in the wall when the incident angle is less than the critical angle; (c) When the incident angle is beyond the critical angle, the P-wave no longer exists, and all refracted energy is contained in the S-wave. (d) The S-waves are reflected off the boundaries to create many reflections called S-reflections.

In order to supply power consistently to EcoCapsules embedded within structures, the reader emits a continuous body wave (CBW) into the target area, such as a

concrete wall. The transmitting PZT in the reader is designed as a piezoelectric round disc, which vibrates in a direction perpendicular to the disc's surface (i.e., in a push-pull pattern). This specific vibrational mode restricts the PZT to generating only P-waves, as it cannot vibrate in an up-and-down pattern.

When the PZT is directly attached to a wall, it initiates P-waves that propagate through the wall and continue until they meet the opposite surface. The propagation characteristics of these P-waves can be quantitatively described by the half-beam angle α, which is calculated as follows:

$$\alpha = \arcsin\left(\frac{0.514 C_p}{fD}\right), \tag{3.7}$$

where D represents the diameter of the PZT, f is the frequency of the wave, and C_p is the velocity of the P-wave in concrete. Given the parameters, $D = 40$ mm and $f = 230$ kHz, the computed half-beam angle α is approximately 11°. This results in the CBW covering only a small cone of about 132 cm^3 volume within the 15 cm depth of the concrete, as depicted in Fig. 3.4(a). Under these conditions, only the nodes directly beneath the PZT are capable of being powered up.

This configuration poses a significant challenge since the exact locations of EcoCapsules within the concrete are not predetermined. Therefore, attempting to energize the EcoCapsules necessitates an exhaustive search across the entire wall area, hoping to fortuitously activate the backscatter nodes. Such a method is clearly inefficient and impractical for reliable operation. This limitation highlights the need for developing a more effective approach to targeting and powering the EcoCapsules embedded within solid structures.

Reflection. *Thus, how can we power up multiple backscatter nodes inside a wall using a single transmitting PZT without knowing their locations?* This challenge brings us to the consideration of how body waves interact with boundaries between different media. When body waves, such as P-waves, encounter a boundary between dissimilar mediums like concrete and air, they are predominantly reflected. This reflection is

quantified by the reflection coefficient, defined as:

$$R = \frac{Z_{\text{con}} - Z_{\text{air}}}{Z_{\text{con}} + Z_{\text{air}}} \tag{3.8}$$

where Z_{con} and Z_{air} represent the acoustic impedances of concrete and air, respectively. According to studies [83], with $Z_{\text{con}} = 4.66 \times 10^6$ kg/m^{2}s and $Z_{\text{air}} = 4.15 \times 10^2$ kg/m^{2}s, the impedance difference is substantial, leading to a reflection coefficient near 100%, specifically $R = 99.98\%$. This means more than 99% of the body waves are completely reflected at the concrete-air boundary.

Inspired by this phenomenon, we use internal reflections to increase coverage by employing a polymer wedge, referred to as a *wave prism*, positioned between the PZT and the concrete surface. This setup is illustrated in Fig. 3.4(b). By adjusting the angle of the prism's inclined plane, we can direct the body waves into the concrete at various incident angles. The P-waves generated by the PZT, when transmitted through the inclined plane of the prism, enter the concrete and are designed to bounce off its internal boundaries multiple times. This action fills the interior with wave reflections, as depicted in Fig. 3.4(d), thereby energizing backscatter nodes located at arbitrary positions with minimal effort.

However, a complexity arises when P-waves cross the interface between the prism and the concrete. At this juncture, a portion of the wave energy continues to propagate forward as a P-wave, while another portion is converted into an S-wave, initiating a new propagation path. This results in two modes of body waves present within the concrete, a scenario we describe as *one mode in, two modes out*, visualized in Fig. 3.4(b). The receiving PZT faces a challenge in distinguishing the type of wave received, as both P-waves and S-waves induce mechanically indistinguishable vibrations on it. This overlap complicates the decoding process, particularly because S-waves, traveling 40% slower than P-waves, cause a 60% data overlap. This superposition of identical data carried by both wave types complicates the signal interpretation, demanding advanced strategies to effectively separate and decode the transmitted

information.

Refraction. According to Snell's Law, a wave is *refracted* when it travels through a boundary between two different materials at a non-zero angle. The refraction angle is determined using the following relation:

$$\frac{\sin\theta_i}{C_i} = \frac{\sin\theta_p}{C_p} = \frac{\sin\theta_s}{C_s} \tag{3.9}$$

where θ_i and C_i denote the incident angle and the wave velocity in the first material, respectively, while θ_p (or θ_s) and C_p (or C_s) represent the refracted angles and velocities of the P-wave (or S-wave) in the second material. Given that P-waves travel approximately 40% faster than S-waves, this difference in velocities leads to the following implication:

$$C_p > C_s \Rightarrow \theta_p > \theta_s \tag{3.10}$$

This inequality indicates that the refracted angle of the P-wave is larger than that of the S-wave, as visually documented in Fig. 3.4(b). Additionally, both refracted angles increase as the incident angle is raised, with the angle of the P-wave reaching 90° at what is termed the first critical angle. At this juncture, the P-wave effectively vanishes, leaving only the S-wave propagating within the concrete. Increasing the incident angle further to the second critical angle leads to the disappearance of the S-wave as well, resulting in the absence of body waves and the dominance of surface waves within the concrete.

The relative amplitudes of these two wave modes, as a function of the incident angle, are plotted in Fig. 3.5. The first and second critical angles are calculated to be approximately 34° and 73°, respectively. Within this range, only S-waves remain active in the concrete, facilitating what we refer to as S-wave-only reflections (S-reflections). By strategically positioning the wave injection at an incident angle within the range of $\theta_i \in [34°, 73°]$, as depicted in Fig. 3.4(d), we can effectively eliminate P-wave interference. This setup optimizes the environment for S-reflections to propagate extensively within the concrete, thereby enabling efficient wireless charging of Eco-

Capsules positioned arbitrarily within the structure. This method ensures that the P-waves are excluded from the process, enhancing the efficiency and range of energy transfer through S-wave reflections.

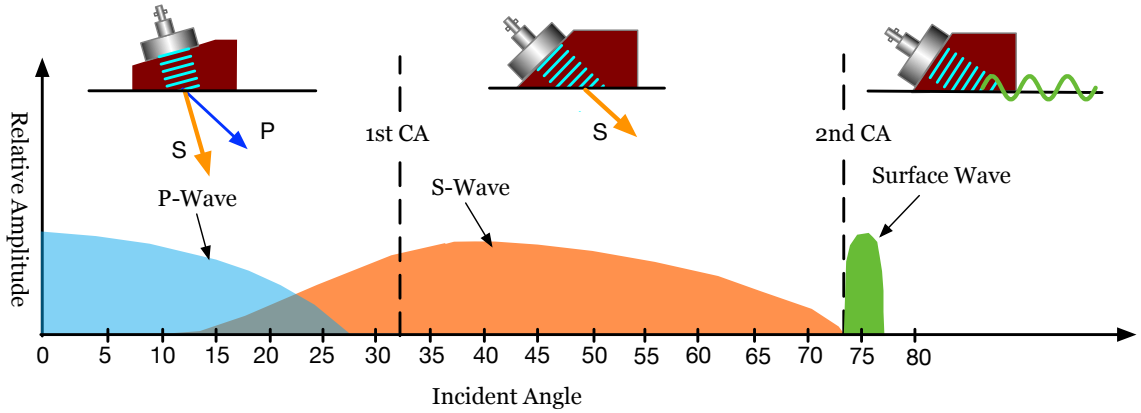

Fig. 3.5: Relative amplitudes of P and S waves vs. incident angle. The P- and S-waves dominate the body alternatively as a function of the incident angle. Beyond the first critical angle (CA), the P-wave disappears and only S-wave resides. Beyond the second critical angle, two models of waves disappear and no body waves present inside the concrete.

Material Selection for the Wave Prism. The choice of material for the wave prism is crucial, as it involves a careful balance to maximize the effectiveness of the wave transmission into concrete. The sound speed within the prism material plays a dual role in determining both the refraction angle and the energy transmission efficiency. On the one hand, the sound speed in the prism should be significantly lower than that in concrete to ensure that the refracted wave angles remain small, facilitating easier elimination of undesired wave modes at smaller incident angles. On the other hand, to minimize energy loss at the interface, the sound speed in the prism should also be sufficiently high to reduce the impedance difference between the prism and concrete, thereby allowing more energy to be transferred through the prism.

Given these considerations, we have selected polylactic acid (PLA) as the prism material. PLA offers an advantageous balance with a density roughly half that of concrete and a sound speed of approximately $C_{\text{prism}} = 1250$ m/s, compared to $C_{\text{con}} = 3700$ m/s in concrete. The reflection coefficient R, computed using the formula

$$R = \frac{(Z_{\text{con}} - Z_{\text{prism}})}{(Z_{\text{con}} + Z_{\text{prism}})} \tag{3.11}$$

where Z_{con} and Z_{prism} are the acoustic impedances of concrete and the prism, respectively, evaluates to approximately 33.43%. This coefficient implies that about 67% of the energy from P-waves generated by the PZT can effectively be conducted into the concrete. Additionally, the choice of PLA lowers the first critical angle to 34°, enhancing the range of incident angles that effectively facilitate wave transmission without significant losses. PLA's uniform sound velocity across different types of concrete further simplifies operational logistics, as there is no need to customize prism materials for different concrete environments. This universality makes PLA an excellent choice for the prism, combining practicality with performance to optimize the efficacy of the EcoCapsule system.

3.3.3 Wireless Communication: Downlink

The downlink is from the reader to backscatter with two purposes: energy supply and command delivery.

Concrete Frequency Response. *Which vibrating frequency optimally facilitates the propagation of body waves within concrete?* To address this question, we conducted a series of experiments aimed at measuring the frequency response of concrete. The frequency response of concrete is a quantitative measure of how the material's output spectrum reacts to a vibrational stimulus. In the research field of modern construction, three predominant types of concrete are used, each differing significantly in material composition and performance: normal concrete (NC) [84], ultra-high performance concrete (UHPC) [85], and ultra-high-performance fiber-reinforced concrete (UHPFRC) [86].

We tested four concrete blocks in our experiments: a 7 cm-thick NC block, a 15 cm-thick NC block, a 15 cm-thick UHPC block, and a 15 cm-thick UHPFRC block, as depicted in Fig. 3.6(a). Each block measures 15 cm in width and height, with detailed mix proportions and physical properties listed in Table 3.1. To conduct the

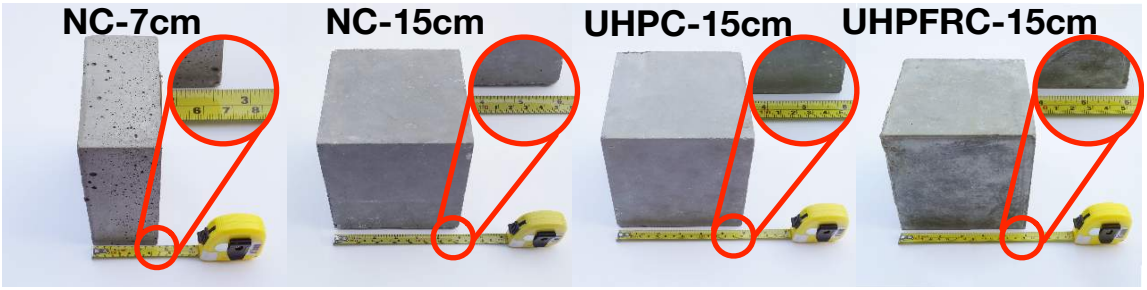

(a) Tested concrete blocks

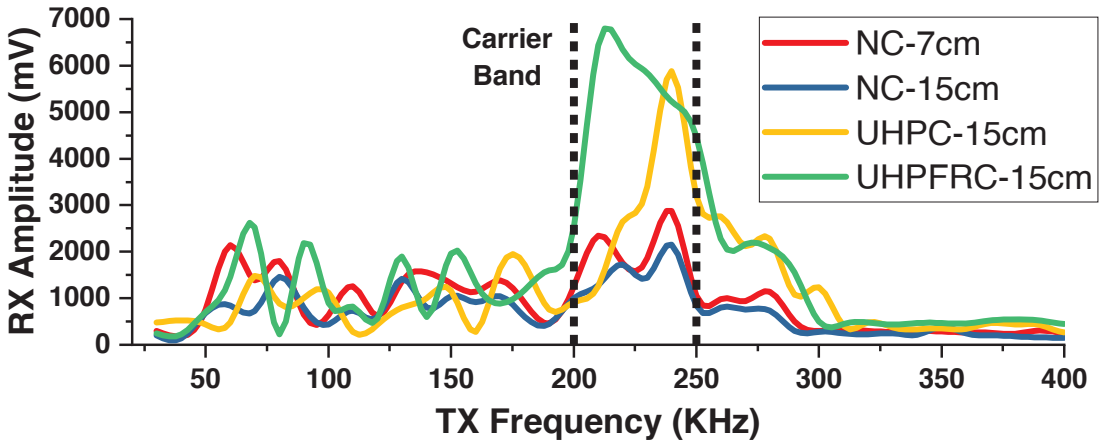

(b) Frequency response

Fig. 3.6: Concrete Frequency Response. We collected the the responses of four morden concrete blocks to the vibrating stimuli at various frequencies.

experiments, we attached a transmitting PZT equipped with a 45° wave prism to one side of each concrete block and a receiving PZT on the opposite side. This setup helps to nearly eliminate surface wave interference due to the blocks' sharp edges and corners.

The operational frequency range for the COTS PZTs spanned from 1 kHz to 1 MHz. We transmitted a sinusoidal signal at various frequencies, initiating at 20 kHz and incrementing in steps of 10 kHz up to 400 kHz, with each frequency setting tested ten times to ensure accuracy. The peak voltage applied was 100 V. The results of these tests are illustrated in Fig. 3.6(b), revealing several key insights.

Firstly, we observed that irrespective of the type of concrete, the resonance frequency—where wave propagation is most efficient—occurred between 200 kHz and

250 kHz. Beyond this range, wave propagation attenuated rapidly. Secondly, the peak responses recorded for UHPC and UHPFRC were significantly higher than those for NC. This difference can be attributed to the higher compressive strengths and reduced intermolecular spacing in UHPC and UHPFRC, which enhance the propagation of elastic waves through these denser materials.

Table 3.1: Mix proportions and properties of concretes used in our experiments. In the table, HRWR is the high range water reducers, f_{co} is the compressive strength, E_c is the concrete elastic modulus, ν is the Poisson's ratio, and ϵ_{co} is the corresponding strain.

#	Concretes	NC	UHPC	UHPSSC
Mix proportions	Cement	300	830	807
	Silica Fume	0	207	202
	Fly Ash	200	0	0
	Quartz Power	0	207	202
	Sand	796	913	888
	Granite	829	0	0
	Steel Fiber	0	0	471
	Water	175	164	158
	HRWR	9	27	29
Properties	f_{co}(MPa)	54.1	195.3	215.0
	E_c(GPa)	27.8	52.5	52.7
	ν	0.18	0.21	0.21
	ϵ_{co}(%)	0.263	0.447	0.447

Pulse Interval Encoding (PIE). In our study, we employ Pulse Interval Encoding (PIE), a widely utilized data coding scheme for downlink transmissions within backscatter communication systems. As depicted in Fig. 3.7, in PIE, a bit zero is represented by a high-voltage interval followed by a shorter low-voltage pulse. Conversely, a bit one is encoded as a long high-voltage interval followed by a brief low-voltage pulse. This encoding method is particularly advantageous in battery-free networks, such as those used in backscatter systems, where it is critical to maintain

energy delivery to the backscatter node regardless of the data being transmitted. The PIE scheme is designed to ensure that even during transmissions consisting of long sequences of zeros, at least 50% of the maximum power is continuously delivered to the backscatter node. This is achieved by balancing the duration of low and high voltage intervals for a bit zero. For instance, if the duration of the high voltage is three times longer than that of the low voltage in the encoding of a bit zero, a random sequence of binary data—with an equal mix of zeros and ones—will enable the backscatter node to receive approximately 63% of the peak power available from the carrier wave. This method of encoding ensures that the backscatter node can consistently harvest energy from the continuous body wave (CBW), even when command signals are piggybacked onto the carrier wave. As a result, PIE not only facilitates effective data communication but also enhances the overall efficiency and reliability of the energy harvesting process in backscatter systems, ensuring that the node remains operational even in the presence of data transmission variations.

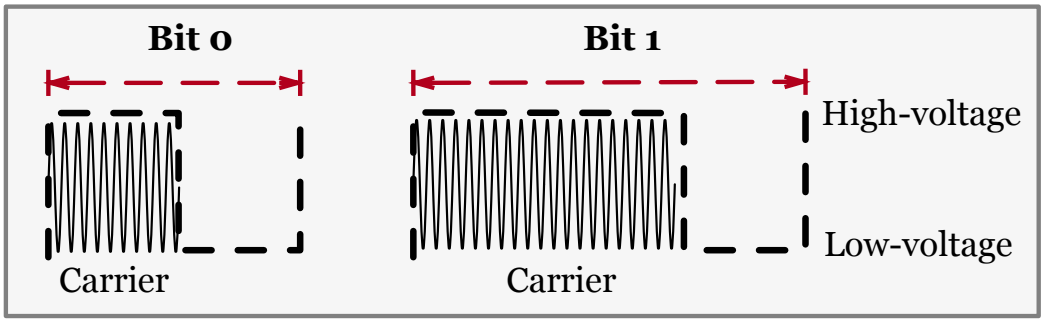

Fig. 3.7: Illustration of PIE symbols in baseband. Both symbols are composed of a high-voltage edge and a low-voltage edge to ensure that a backscatter can harvest energy during at least 50% time.

Ring Effect. In an ideal scenario within PIE, the waveform associated with a PIE symbol should be sharply confined to its high-voltage phase without spilling over into the subsequent low-voltage phase, thus avoiding intra-symbol interference as depicted in Fig. 3.7. However, in practice, the vibrating element, typically a PZT, continues to oscillate even after the deactivation of the driving voltage. This prolonged vibration is known as the *ring effect*, a phenomenon primarily attributed to the inertia of the

PZT—i.e., the material continues to oscillate for a period after the driving voltage is switched off, as noted in existing literature [26]. The Ring Effect in PZT materials stems from their inherent ferroelectric properties, which lead to spontaneous polarization under an applied electric field. This polarization change induces mechanical deformations that resonate, continuing even after the removal of the stimulus.

An illustrative example can be seen in Fig. 3.8(a), where a PIE symbol for a bit zero extends from 0.1 ms to 1.1 ms, with a transition designated at 0.6 ms. Although the power supply is cut at the transition point, the PZT vibration diminishes only gradually, taking an additional 0.3 ms to quell the residual motion. The traditional method to mitigate this ringing involves applying a reverse braking voltage at the end of the high-voltage phase to counteract the residual oscillations. However, accurately determining the optimal timing and magnitude of this braking voltage presents significant challenges. Applying the braking voltage too early or too late, or adjusting it too high or too low, can either prematurely weaken the end of the high-voltage phase or inadvertently elevate the start of the low-voltage phase. This resonant behavior can persist as a self-sustaining oscillation, akin to the ringing of a bell that continues to sound after being struck. Managing this effect is crucial for applications where precision and control over mechanical responses are necessary. In the context of PIE in backscatter communication systems, unmanaged ring effects can lead to significant data corruption due to misinterpretation of the signal's intended start and stop points. Effective control strategies must, therefore, be implemented to harness or mitigate this effect, ensuring reliable data transmission and energy harvesting in backscatter systems.

FSK in OOK out. The inherent material properties of concrete significantly affect the amplitude of body waves at different frequencies, as indicated by our concrete frequency response experiments (see Fig. 3.6(b)). This phenomenon is particularly pronounced at resonant versus non-resonant frequencies. We exploit this characteristic to mitigate the ring effect commonly observed in PZT systems. Instead of halting

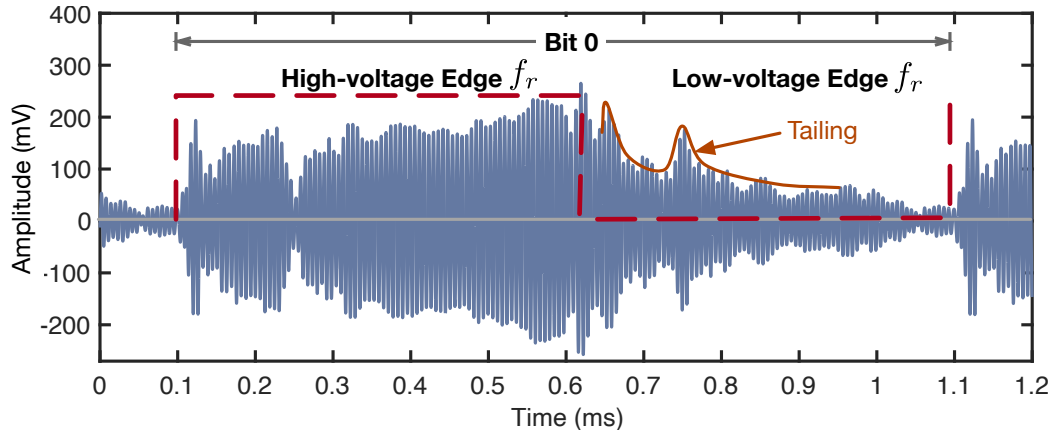

(a) Vibration tailing

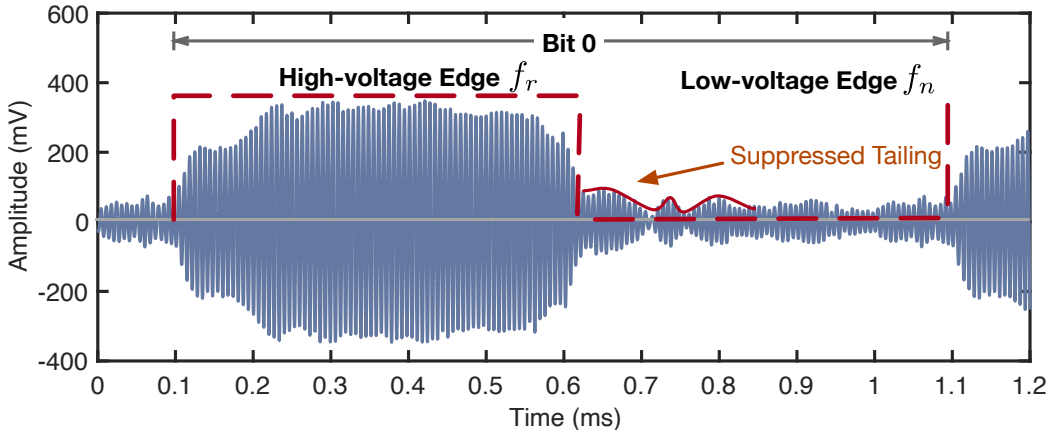

(b) Suppressed tailing

Fig. 3.8: Ring effect. (a) shows the PIE symbol zero without tailing suppression; (b) the tailing is suppressed by the concrete naturally due to the off-resonance effect.

the PZT's vibration to signify a low-voltage edge—which can lead to unwanted lingering oscillations (ring effect)—we adjust the PZT to oscillate at a non-resonant frequency.

Specifically, for the high-voltage edge, the CBW is transmitted at a resonant frequency, such as 230 kHz, where the concrete naturally amplifies the wave's amplitude. Conversely, for the low-voltage edge, we switch to a non-resonant frequency, like 180 kHz, where the amplitude is naturally dampened by the concrete due to non-resonant radiation damping. This strategy eliminates the need to start or stop the vibration abruptly, thus effectively reducing the mechanical inertia that typically causes the

ring effect.

Fig. 3.8(b) illustrates the effectiveness of this anti-ring-effect strategy, showcasing how the concrete's properties help suppress the tailing at non-resonant frequencies. Consequently, while traditional backscatter systems commonly employ OOK for downlink transmissions, our approach utilizes FSK in conjunction with the off-resonance damping effect of concrete to simulate OOK behavior at the backscatter nodes. This method allows for data decoding using a simple envelope detector, which is already equipped with EcoCapsules. By leveraging the FSK to manage wave amplitudes in relation to concrete's frequency response, we ensure that data transmission remains robust against the ring effect without the need for complex hardware adjustments. This approach not only maintains the integrity of data communication but also significantly reduces power consumption and manufacturing costs, aligning with the need for efficient and cost-effective structural health monitoring solutions.

3.3.4 Wireless Communication: Uplink

The uplink is initiated by an EcoCapsule to transmit sensing data to the reader through the backscatter communication.

Backscattering. To assess the viability of backscatter communication within concrete structures, we conducted an experiment using an EcoCapsule embedded in a 15 cm-thick block of UHPC. For this test, we transmitted a CBW at a frequency of 230 kHz, with a peak voltage of 100 V, to energize the EcoCapsule and serve as the carrier wave for backscatter communication.

The EcoCapsule was programmed to modulate this carrier by toggling its impedance switch at a frequency of 2 kHz. This modulation creates variations in the reflected wave, which are then detected and decoded. A separate PZT affixed directly to the opposite side of the concrete block, served as the receiver. This placement strategy ensures that the receiving PZT is integrally aligned with the concrete's structure,

optimally positioned to directly capture S-wave reflections without the need for a prism, thus maximizing the detection of the backscattered signals.

In line with established practices in backscatter communication, we employed the FM0 coding scheme to enhance the robustness of data transmission. FM0 coding differentiates between a bit zero and a bit one based on the presence or absence of a transition within the symbol window rather than relying solely on the duration of signal phases. This method is particularly suited to environments where signal integrity may be compromised by material properties or construction inconsistencies.

Self-interference Cancellation. Backscatter communication inherently operates in a full-duplex mode by utilizing the reflections of a downlink signal to transmit data. However, a significant challenge arises when the receiving Piezoelectric Transducer (PZT) tries to detect weak backscatter signals while simultaneously receiving a much stronger direct signal from the transmitting PZT. This direct signal often produces surface waves and S-reflections that are approximately 10× stronger than the backscattered signals, severely overwhelming the receiver and complicating the detection process.

Simply increasing the transmit power exacerbates the problem, as it not only enhances the downlink signal but also amplifies the backscatter response. This often leads to the saturation of the Analog-to-Digital Converter (ADC) at the receiver, preventing it from distinguishing the weak backscatter response, particularly when the backscatter node is nearby. To mitigate this issue, several strategies, such as filtering, synchronization, or advanced signal processing, are essential.

For example, in our experiment with an EcoCapsule implanted within a 15 cm-thick UHPC block, we transmitted a single-tone Continuous Body Wave (CBW) at 230 kHz with a peak voltage of 100 V. The EcoCapsule was programmed to modulate this signal by switching its impedance at 2 kHz. While this setup effectively transmits the uplink signal, the strong downlink signal could potentially mask the backscatter

due to self-interference.

To demonstrate this, consider the signal received by the PZT Rx:

$$y(t) \quad = \quad I\cos\left(2\pi f_c t\right) + hp(t)\cos\left(2\pi f_c t\right), \tag{3.12}$$

where I is the amplitude of the CBW, h is the channel gain from the backscatter node to the receiver, and $p(t)$ is the modulating signal of the backscatter node. Given $I \gg h$, self-interference significantly impacts the receiver's ability to discern the backscatter response.

To address this issue, EcoCapsule exploits the bandwidth of the PZT, shifts the backscatter response out-of-band, and filters out the strong in-band downlink signal as shown in Fig. 3.9. Specifically, rather than just applying $p(t)$ across the backscattering switch, it can apply $p(t)\cos\left(2\pi f_o t\right)$ to shift the response away from the downlink signal in the frequency domain. In such a scenario, the received signal by the hydrophone is given by the following equation:

$$y(t) = I\cos\left(2\pi f_c t\right) + hp(t)\cos\left(2\pi f_c t\right)\cos\left(2\pi f_o t\right) \tag{3.13}$$

$$= I\cos\left(2\pi f_c t\right) + 0.5hp(t)\cos\left(2\pi\left(f_c - f_o\right)t\right) + 0.5hp(t)\cos\left(2\pi\left(f_c + f_o\right)t\right) \tag{3.14}$$

So, the received signal contains the downlink frequency at f_c and the backscatter response at $f_c + f_0$ and $f_c - f_0$. Assuming $f_0 = 5$ kHz, then the backscatter response is at 225 kHz and 235 kHz, while the downlink signal remains at 230 kHz as shown in Fig. 3.9. To address the issue of the strong downlink signal overwhelming the weak backscatter response in backscatter communication, our solution is to apply a low-pass filter to the received signal. By setting the filter's cutoff frequency to 228 kHz, the downlink signal can be eliminated, leaving only the backscatter response at 225 kHz for the receiver to decode. This simple filtering technique can effectively enhance the signal-to-noise ratio and improve the overall performance of the backscatter communication system.

We adopt a similar solution used in the RFID system [87] or previous underwater PBS [28, 31] to overcome such self-interference. Thus, self-interference can be easily filtered out in the spectrum. We can also place signal amplification devices such as lock-in amplifiers or low-noise amplifiers after the filter and before the ADC to further amplify the weak backscattered signal. These devices can further increase communication distance.

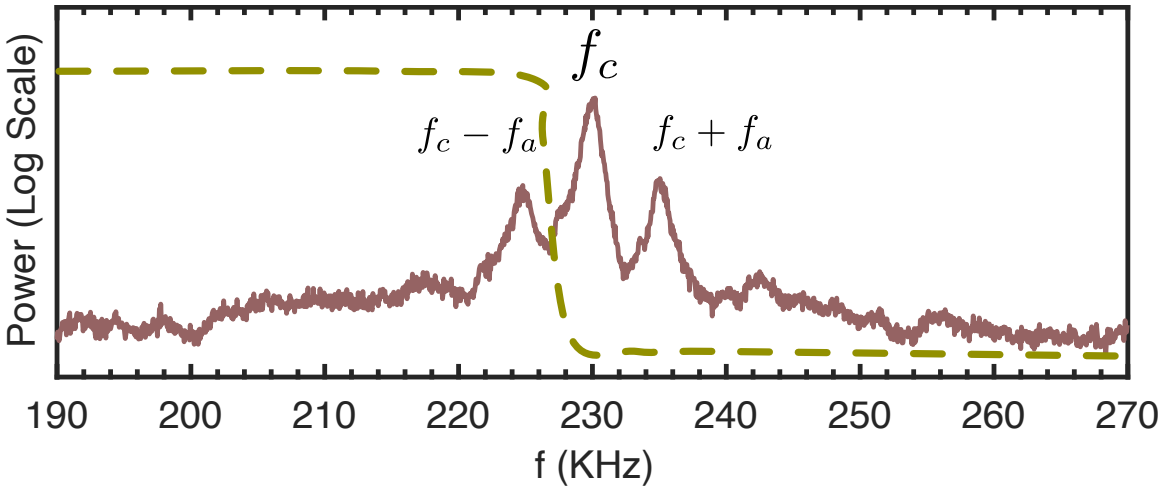

Fig. 3.9: Self-interference elimination

Fig. 3.9 illustrates the effectiveness of this approach, showing a clear spectrum of received signals with three distinct peaks: one from the CBW and the other two from the amplitude-modulated (AM) backscatter signals on either side of the main peak. Notably, no signal at non-resonant frequencies is detected during the backscatter period in the uplink, indicating effective isolation of the communication channels by the guard band between the signals.

Scaling to Multiple EcoCapsules. To efficiently manage multiple EcoCapsules embedded within a structure, we incorporate the Time Division Multiple Access (TDMA) protocol, akin to those used in the RFID Gen 2 standards. In this setup, each EcoCapsule is assigned a specific time slot during which it can transmit its data, minimizing the chance of signal collision and interference among devices. This approach is particularly suited to environments where the number of EcoCapsules is rel-

atively small and where SHM applications can tolerate delays—given that structural degradation typically progresses over days rather than seconds, the delay introduced by TDMA is acceptable.

For scenarios requiring denser installations of EcoCapsules, such as in large or complex structures, we can also integrate Frequency Division Multiple Access (FDMA) alongside TDMA to enhance system scalability. In FDMA, different frequency bands are allocated to different transmitters, allowing simultaneous transmission without interference. To facilitate FDMA, components such as capacitors, inductors, or resistors can be connected in parallel at both terminals of a PZT. This adjustment allows us to fine-tune the resonant frequency of each PZT, enabling it to operate effectively within a designated frequency band and achieve frequency division multiplexing.

3.4 Practical Discussion

3.4.1 Acoustic vs. RF Backscatter for In-Concrete SHM

Numerous studies have explored the integration of passive RFID tags for long-term in-concrete SHM, achieving varied levels of success [79, 80, 88]. These initiatives demonstrate that while RF-based backscatter systems are innovative, their communication ranges are severely limited—often to just a few centimeters—when embedded within concrete. This limitation stems from the substantial attenuation of RF signals by the dense, absorptive properties of concrete.

Conversely, concrete's ability to efficiently conduct mechanical vibrations presents a compelling alternative. Acoustic backscatter systems, or PBS, utilize these mechanical vibrations to achieve communication ranges that can extend several meters, far surpassing the capabilities of RF systems in similar settings. Given these advantages, PBS technology shows significant promise as the future standard for in-concrete com-

munications within SHM applications.

3.4.2 The Impact of the Concrete Structure

The internal structure of concrete can be highly variable and complex. Typical compositions may include steel reinforcement bars, irregular sand particles, gravel, and even cavities formed from entrapped air during the casting process [89]. These inclusions act similarly to reflectors in RF communications, causing acoustic waves to reflect, diffract, and ultimately alter in direction, frequency, and intensity as they propagate through the concrete.

Despite these potential obstacles, the relative proportion of such inclusions within the concrete is generally small, meaning that their impact on overall communication efficacy is typically minimal. In fact, our empirical data suggests that adjustments to the operational frequency of the PBS can significantly enhance communication quality in scenarios where the channel is degraded by these internal structures. Fine-tuning the frequency allows the PBS to adapt to specific conditions within the concrete, optimizing signal clarity and strength even in the presence of complex internal architectures.

In conclusion, while both acoustic and RF technologies offer potential for in-concrete SHM, the superior propagation characteristics of acoustic waves within concrete make PBS a more effective and promising approach for future applications. This method not only circumvents the severe limitations posed by RF signal attenuation but also provides a robust framework for overcoming the inherent challenges presented by the diverse and intricate internal structures of concrete.

3.5 Implementation of EcoCapsules

In this section, we describe our mechanical and hardware fabrication process for EcoCapsules. The detailed hardware and software design has been released on the

Github [90] and our project website [91].

3.5.1 Stressless and Resonant Shell

We have developed prototypes of our EcoCapsule, which are uniquely designed in the shape of spheres with small recessed areas for the PZT frontend. Each prototype measures approximately 4.5 cm in diameter, roughly the size of a standard ping-pong ball. This specific design serves dual functions: stress equalization and Helmholtz resonance.

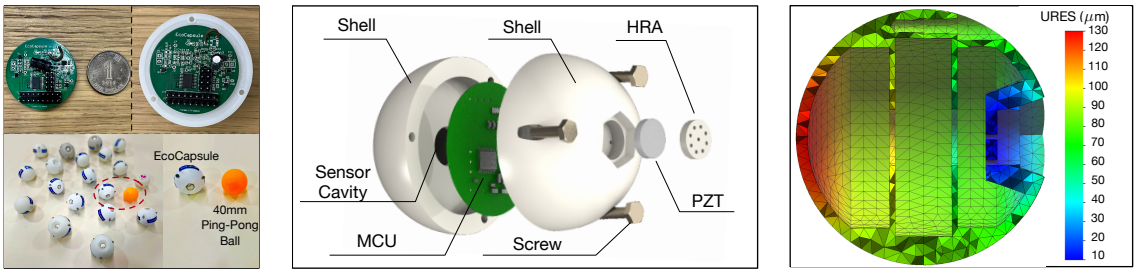

(a) EcoCapsules (b) Exploded view (c) Stress distribution

Fig. 3.10: Mechanical and hardware fabrication of EcoCapsules. (a) The EcoCapsule prototypes are depicted alongside a standard 40 mm ping-pong ball for scale. Their internal circuit board is nearly as small as a one-dollar coin. (b) An exploded view of an EcoCapsule showing its internal components. (c) The stress distribution within an EcoCapsule during operation.

Stress Equalization. The spherical shell design of the EcoCapsule is engineered to equalize the stress exerted by the surrounding concrete. Despite the shell's inherent capability to distribute external pressures evenly, additional measures are necessary to prevent it from cracking due to the significant pressure differential between the interior air and the external concrete. This pressure difference, denoted by $\Delta\mathcal{P}$, is described by the following equation:

$$\Delta\mathcal{P} = \rho g h - \mathcal{P}_{\text{air}} \tag{3.15}$$

where ρ represents the density of the concrete, h is the height of the concrete over the EcoCapsule, g is the acceleration due to gravity, and $\mathcal{P}_{\text{air}}$ is the standard atmo-

spheric pressure (101.325 kPa). Concrete density typically ranges from 1840 kg/m^3 to 2360 kg/m^3 [92].

The shell is manufactured using stereolithography (SLA) 3D printing technology, which uses a resin with a tensile strength of approximately 65.0 MPa and Young's modulus of approximately 2.2 GPa [93]. With a shell thickness set at 2.0 mm and allowing for a deformation tolerance of up to 5%, we utilized Solidworks [94] to conduct a finite element analysis (FEA) to determine the maximum pressure differential ($\Delta\mathcal{P}_{\max}$) the shell can withstand, which was found to be approximately 4.3 MPa. By inserting $\Delta\mathcal{P}_{\max}$ back into Equation 3.15, the maximum viable building height for embedding our EcoCapsules without risk of structural failure is calculated to be around 195 meters (approximately 55 floors).

For applications requiring installation in taller structures, substituting the resin with metal materials, such as alloy steel (with a $\Delta\mathcal{P}_{\max} \approx 115.2$ MPa), could extend the maximum height to 4985 meters, well beyond the height of any existing man-made structure.

The internal design of the EcoCapsule further enhances its robustness. As illustrated in Fig. 3.10(b), the sphere's interior is compartmentalized into three cavities by two clapboards. The PZT, measuring 10 mm in diameter, is secured at the end of the sunken mouth to ensure direct exposure to the concrete, while also being protected during the cement pouring process. The motherboard is centrally located between the clapboards, and the sensors are housed in the rear cavity to monitor environmental conditions within the concrete. Fig. 3.10(c) depicts the stress distribution around the EcoCapsule, demonstrating how the structural design effectively redirects most of the stress onto the shell and clapboards, thereby shielding the electronic components from external pressures and ensuring their operational integrity.

Helmholtz Resonance. A Helmholtz resonator (HR) is a device that consists of a container with a volume of moving media, such as air or a fluid-like concrete, and an

open neck. The principle of Helmholtz resonance involves the vibration of the media within and around the neck due to the 'springiness' or elasticity of the media inside the container. This phenomenon allows the resonator to act as a vibration amplifier, capturing minute vibrations at a specific frequency and significantly enhancing them through the resonance of the cavity.

Inspired by this physical principle, we have integrated a Helmholtz resonator array (HRA) into the design of our EcoCapsules, positioned at the front of the PZT as illustrated in Fig. 3.10(b). The detailed structures of the HRA and each individual HR unit are depicted in Fig. 3.11. Each HR within the array is constructed with a distinct neck and cavity. The media contained within each cavity behaves akin to a spring due to its compressibility, enabling it to store potential energy that contributes to the resonance effect.

The resonant frequency (f_r) of an undamped Helmholtz resonator is determined by the following formula:

$$f_r = \frac{C_s}{2\pi}\sqrt{\frac{3A_n}{4V_c H_n}} \tag{3.16}$$

where C_s represents the speed of S-waves in concrete, A_n is the cross-sectional area of the neck, H_n is the length of the neck, and V_c is the volume of the cavity.

For our EcoCapsules, targeting an operational resonant frequency around 230 kHz, we selected the geometrical parameters of the HR to optimize resonance at this frequency. Specifically, the dimensions chosen include a neck cross-sectional area (A_n) of 0.78 mm^2, a cavity volume (V_c) of 2.76 mm^3, and a neck length (H_n) of 0.8 mm. These parameters were carefully calculated to ensure that the HRAs effectively amplify vibrations at the desired frequency, thereby enhancing the sensitivity and responsiveness of the EcoCapsule in detecting and communicating via acoustic signals in concrete environments. This integration of Helmholtz resonance into the design not only improves the EcoCapsule's ability to capture and amplify relevant signals but also significantly boosts the overall efficiency of the backscatter communication

system by optimizing the energy transfer from the ambient vibrations within the concrete structure.

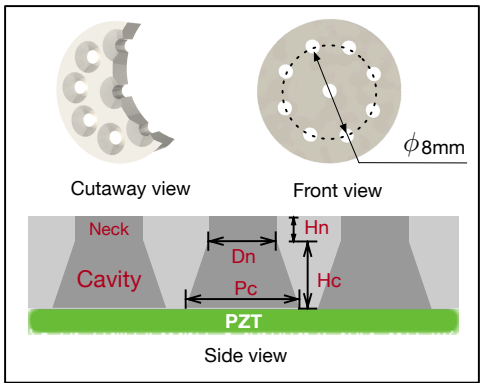

Fig. 3.11: Helmholtz resonator array

3.5.2 Circuitry

The heart of the EcoCapsule is its battery-free processing board, which is meticulously designed and assembled on a round two-layer printed circuit board (PCB) measuring 3.5 cm in diameter. This core component is depicted in Fig. 3.10(a) and represents a versatile and extensible computing platform tailored for long-term SHM. Fig. 3.12 illustrates the comprehensive schematic of our hardware design, drawing inspiration from pioneering work in the field, such as WISP [67] and PAB [28]. We have fabricated a total of 30 prototypes for a thorough evaluation, utilizing the specialized services of JLCPCB [95]. Each unit costs approximately 10 USD, with circuit components manually soldered onto the PCBs and subjected to individual testing.

The hardware is engineered to fulfill four critical functions: power harvesting, backscatter communication (uplink), signal receiving and decoding (downlink), and interfacing with various sensors. *(1) Power Management:* At the forefront of the energy management system is a four-stage voltage multiplier that captures weak acoustic signals and converts them into usable DC output. This is followed by a Ti low-dropout (LDO) regulator, specifically the LP5900SD-1.8 [96], which stabilizes the voltage at a constant 1.8V, ensuring reliable power supply to the microcontroller unit (MCU) and sensors.

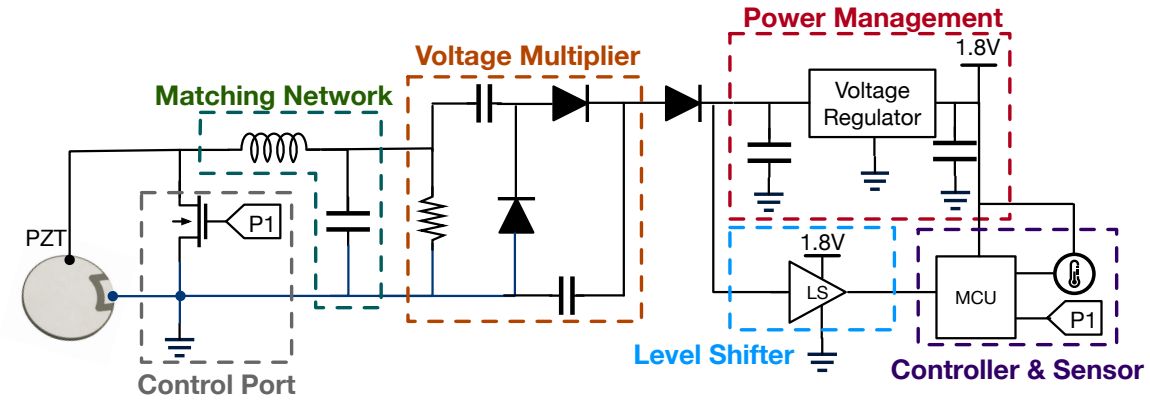

Fig. 3.12: Circuit schematic of the EcoCapsule.

A diode is strategically placed before the LDO to prevent any potential backflow of current into the supply system [97]. *(2) Demodulation:* The demodulation process utilizes the voltage multiplier as an envelope detector to separate the baseband signal from the carrier. Following the designs used in PAB [28], a TXB0302 level shifter [98] is employed to filter out high-frequency noise and to binarize the received signal, enhancing the clarity and accuracy of data interpretation. *(3) Controller and Sensor:* The control system is based around the Ti MSP430G2553 MCU [99], chosen for its ultra-low power consumption—414 μW in active mode and just 0.9 μW in sleep mode. This MCU is adept at decoding downlink PIE commands through timer interrupts, which accurately measure the intervals between each signal edge from the demodulator [28]. For sensor interfacing, the MCU utilizes its internal ADC for analog sensors and communicates with digital sensors via the I^2C protocol. *(4) Sensing Functions:* To monitor concrete's internal conditions, we have integrated sensors for measuring temperature, humidity, and strain. The AHT10 integrated temperature and humidity sensor [100] provides readings of the internal relative humidity and temperature. Additionally, a BFH1K-3EB full-bridge strain gauge [101] is mounted on the rear of the node shell to assess bidirectional internal strains within the concrete.

These integrated technologies and components make the EcoCapsule a robust tool for SHM, capable of providing detailed, real-time data on the health of concrete structures, thereby significantly advancing the field of civil engineering monitoring.

3.5.3 Lifetime and Durability

To ensure EcoCapsule's effectiveness as a long-term solution for SHM, it is crucial to discuss its lifetime and durability. Since the EcoCapsules are designed to be implanted into concrete structures, they must operate reliably for many years, ideally matching the lifespan of the architecture itself. To enhance the lifetime of the EcoCapsule for real-world applications, several strategies should be considered to ensure its durability and long-term functionality, aligning with the expected lifespan of the concrete structure.

First, the EcoCapsule's shell material can be optimized by selecting high-strength, corrosion-resistant composites or metals that can withstand prolonged exposure to harsh environmental conditions, such as moisture, temperature fluctuations, and pressure changes within the concrete. Materials with self-healing properties or anti-corrosive coatings could further extend the longevity of the device by mitigating the effects of environmental degradation. Employing advanced encapsulation techniques such as conformal coatings or hermetic seals would protect sensitive electronics from moisture, dust, and chemical exposure, further safeguarding the device's functionality.

Moreover, utilizing advanced PCB printing technology that is specifically designed to resist corrosion and penetration from the harsh concrete environment can significantly improve the longevity of the EcoCapsule. Techniques such as nano-coating or using ceramic-based PCBs would provide additional protection against moisture and aggressive chemical environments that could otherwise compromise the integrity of the circuit board. These improvements would ensure that the EcoCapsule's electronics remain fully functional for extended periods, even in challenging environments, contributing to its long-term performance without requiring frequent maintenance or replacement.

3.6 Evaluation

This section introduces the evaluation methodology and the results.

3.6.1 Methodology

First, we describe the experimental setup and methodology.

Reader Configuration *(1)Transmitter:* The transmitter setup includes a wave prism, a transmitting piezoelectric transducer (PZT), and a front-end system that translates baseband signals into PZT vibrations. The transmitting PZT is a 2 mm thick disc with a 40 mm diameter, operating at 230 kHz, designed to handle peak voltages up to 250 V. This larger PZT size enhances durability under high voltage conditions. The prism, fabricated from PLA via 3D printing, is positioned at a default incident angle of 60°. The transmission system is powered by a Rigol DG2052 signal generator [102], amplified through a Ciprian HVA-400-A power amplifier [103]. Additionally, a matching network optimizes power transfer from the amplifier to the PZT. The signal generator is controlled by a Lenovo Thinkpad PC via a serial connection, with downlink signals modulated by Pulse Interval Encoding (PIE) using MATLAB, adhering to the EPC UHF Gen2 protocol [104] for packet structure *(2)Receiver:* The receiver utilizes a PZT identical to the transmitter's but without a prism. This receiving PZT connects to an OWON XDS3000 oscilloscope [105], which captures the signal at a sampling rate of 1 MS/s. Signal decoding is performed using a MATLAB-based program, which begins by estimating the carrier frequency to adjust for any frequency shifts during transmission. It then employs digital downconversion to isolate the baseband backscatter signal, followed by a maximum likelihood approach to decode the FM0 data.

Concrete Casting To evaluate the effectiveness of our embedded systems within a realistic construction environment, we cast several self-sensing concrete blocks using

standard molds, as illustrated in Fig. 3.14 (a). The composition and properties of these blocks, encompassing four different types of concrete, are detailed in Table 3.1. These blocks represent typical building elements such as walls or columns. In practical applications, EcoCapsules can be directly integrated into load-bearing structures during the pouring process. After curing, the integrity and placement of the EcoCapsules within the concrete are assessed using a YXLON FF35 CT scan machine [106], as shown in Fig. 3.14 (b). The resulting CT images, displayed in Fig. 3.14 (c), confirm the structural integrity of the capsules and provide a visual verification of the robustness of the design and the successful embedding of the nodes within the concrete block.

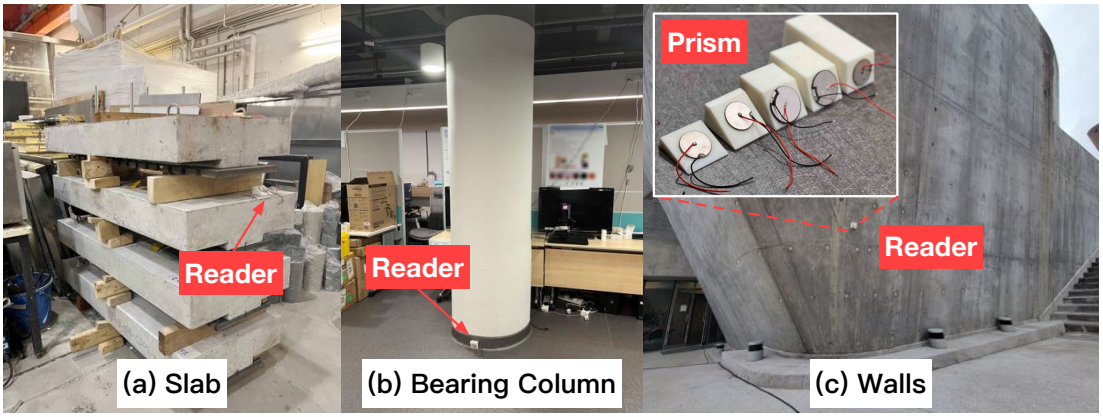

Fig. 3.13: Tested concrete structures and wave prisms

Experiment Settings: To conduct a thorough evaluation of the EcoCapsule's performance within realistic building structures, we fixed constructed concrete blocks onto an existing building using concrete glue. This method ensures minimal damage to the building while potentially causing an approximate 3% loss in wave energy transmission due to the properties of the glue.

Experimental Structures: The experiments are carried out on a variety of concrete structures to assess the system's adaptability and effectiveness in different construction contexts:

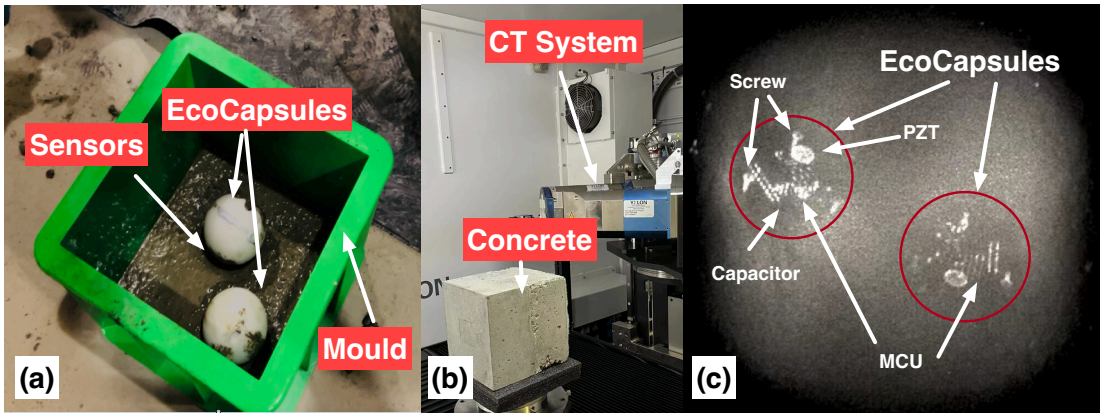

Fig. 3.14: Concrete production and CT examination

- S1: A concrete slab measuring 150 × 50 × 15 cm [107].
- S2: A load-bearing column with a height of 250 cm and a diameter of 70 cm.
- S3: A common wall with dimensions of 2000 × 2000 × 20 cm.
- S4: A protective wall with dimensions of 2000 × 2000 × 50 cm.

These structures are depicted in Fig. 3.13, illustrating the diverse testing environments.

Distance and Communication Setup: The distance between the transmitting and receiving PZTs of the reader system is consistently maintained at approximately 20 cm. The distances from the embedded EcoCapsules to the reader vary across different experimental trials to test the system's range and reliability under varied conditions. The default prism angle for wave transmission is set at 60° unless specified otherwise.

Data Transmission Settings: The bitrate for the uplink communication is set at 1 kbps, a rate that balances efficiency and data integrity for structural health monitoring applications.

Baseline Comparison: For comparative analysis, we use the parameters of the PAB system, a recognized underwater backscatter system that operates at 15 kHz [28], as a

baseline. This comparison is intended to highlight the advancements and performance enhancements achieved by the EcoCapsule in terrestrial concrete environments.

Evaluation Metrics: The effectiveness of the EcoCapsule system is evaluated based on several key performance aspects:

- **Wireless Charging:** Assessing the efficiency and consistency of power delivery to the EcoCapsules embedded within concrete.
- **Uplink Performance:** Measuring the bitrate, signal integrity, and reliability of data transmission from the EcoCapsules to the reader.
- **Downlink Communication:** Evaluating the clarity and accuracy of command and control signals sent from the reader to the EcoCapsules.

These experimental settings and evaluations are designed to rigorously test the capabilities of the EcoCapsule in a variety of structural environments, ensuring that the technology can be effectively applied in real-world construction and monitoring scenarios.

3.6.2 Wireless Charging Performance Evaluation

The efficacy of wireless charging was assessed by evaluating the range and power efficiency across different structural setups designated as S1 to S4. The primary goal was to determine the maximum distance at which an EcoCapsule node could be effectively powered under varying conditions.

Maximum Range: We systematically increased the distance between the reader, transmitting at a consistent voltage, and the EcoCapsule node until the node could no longer be powered. This test was conducted using the highest possible voltage output of our amplifier, set at 250 V, across all four concrete structures (S1-S4). Additionally, we compared these results with those obtained from two different pools

used in the PAB experiments [28]. The results are illustrated in Fig. 3.15, highlighting the performance variability across different materials and structural dimensions.

For clarity, the data points for S1 and S2 are capped at their respective maximum lengths of 150 cm and 250 cm. Observations indicate a diverse range of maximum effective distances, reflecting the interaction between structural properties and wave propagation dynamics: At 50 V, maximum ranges were observed to be 130 cm for S1, 56 cm for S2, 134 cm for S3, 60 cm for S4, and 19 cm for PAB Pool 1. At 200 V, the ranges extended significantly to 235 cm in S2, 500 cm in S3, 385 cm in S4, and 200 cm in PAB Pool 1. PAB Pool 2 required a higher starting voltage of 84 V to power a node at a short distance of 23 cm, but the range increased substantially with voltage, achieving 6.5 m at 125 V.

From these experiments, we derive three key insights:

- **Increased Power, Increased Range:** Higher voltages enhance the transmission power, enabling EcoCapsule nodes to harvest more energy and operate at greater distances.
- **Structural Influence on Range:** Narrower structures tend to focus energy more directionally, similar to a directional RF antenna, which aids in extending the effective range. This phenomenon explains why cylindrical columns (S2) with larger diameters do not perform as well as narrower walls (S3 and S4). The reflections of S-waves between the narrower confines of walls enhance energy transmission efficiency.
- **Material Density and Wave Propagation:** Generally, elastic waves propagate further in denser materials like concrete compared to less dense materials such as water. This general rule aligns with our findings in Pool 1; however, Pool 2 stands out as an exception. The elongated shape of Pool 2, acting like a corridor, facilitates energy focusing through excessive reflections and multipath effects, demonstrating an anomaly in typical propagation behavior.

These findings underscore the complex interplay between structural geometry, material properties, and energy transmission dynamics in wireless charging systems for SHM applications. They provide valuable insights for optimizing EcoCapsule placement and configuration in various construction environments.

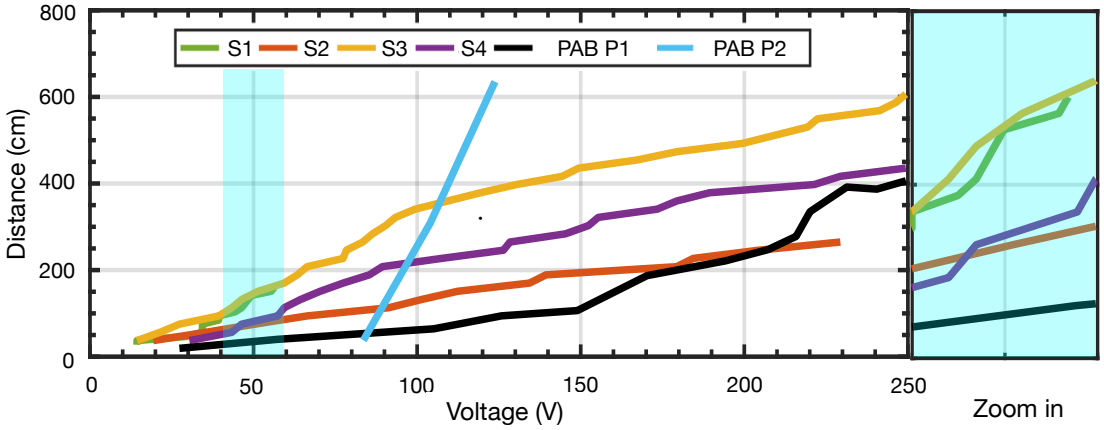

Fig. 3.15: Charging distance changes with applied voltage in different scenarios

Power Consumption: To evaluate the efficiency of the EcoCapsule under various operational conditions, we analyzed its power consumption across different bitrates. Utilizing the Ti MSP-FET hardware programming tool equipped with EnergyTrace technology [108], we precisely measured the power consumption of both the microcontroller unit (MCU) and its peripherals. The results are displayed in Fig. 4.23. Notably, when the bitrate is set to 0 kbps, indicating that the node is in standby mode (waiting to receive and decode downlink signals), the node operates in low power mode (LMP3). In this state, the node exhibits exceptionally low power consumption, drawing only 80.1 μW, attributed to the efficient power management of the MSP430 and the optimized circuit design. As the bitrate increases from 0 kbps to 8 kbps, the total power consumption remains relatively stable, averaging around 360 μW, demonstrating that the node's power draw is minimally affected by changes in the data transmission rate.

Cold Start: The initial activation of each EcoCapsule node, termed a *cold start*, typically requires a longer duration to power up the MCU fully. To quantify this initial activation time, we utilized an oscilloscope to track the duration of the cold start

process under varying voltage levels. The findings, illustrated in Fig. 3.17, indicate that a minimum of 500 mV is necessary to activate the MCU, with the activation process taking approximately 55 ms at this voltage level. Significantly, when the voltage is increased to 2 V or higher, the time required for a cold start decreases dramatically to just 4.4 ms. This rapid activation at higher voltages highlights the EcoCapsule's responsive startup capabilities, which are crucial for situations where quick initialization and readiness are required.

These analyses provide critical insights into the EcoCapsule's power efficiency and readiness for operation, which are crucial factors for its deployment in real-world structural health monitoring scenarios. The results demonstrate the system's low energy consumption during standby and its capability to become operational swiftly under adequate power conditions, ensuring reliability and effectiveness in field applications.

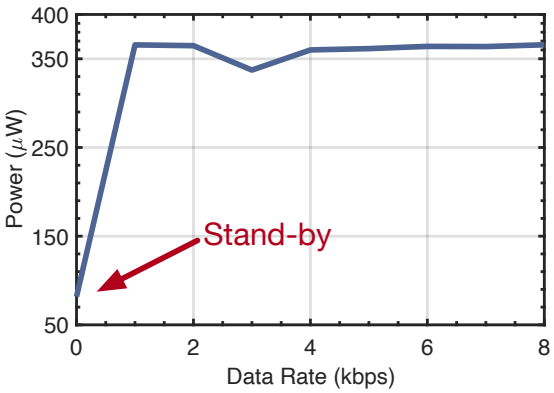

Fig. 3.16: Power Consumption

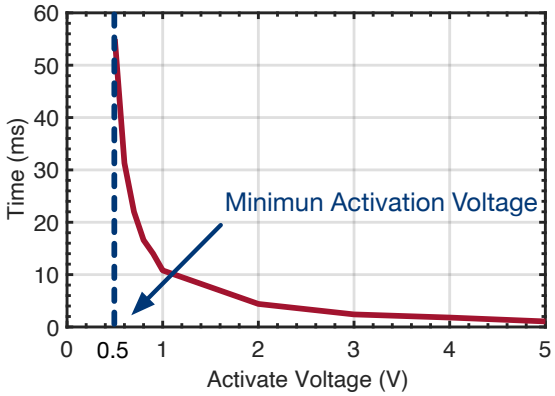

Fig. 3.17: Cold start

3.6.3 Uplink Performance

We explore the uplink performance of EcoCapsules using the NC block as follows:

BER vs. SNR: To assess the reliability of data transmission through EcoCapsules, we conducted an analysis focusing on the Bit Error Rate (BER) as a function of the Signal-to-Noise Ratio (SNR). This relationship is critical in evaluating the robustness

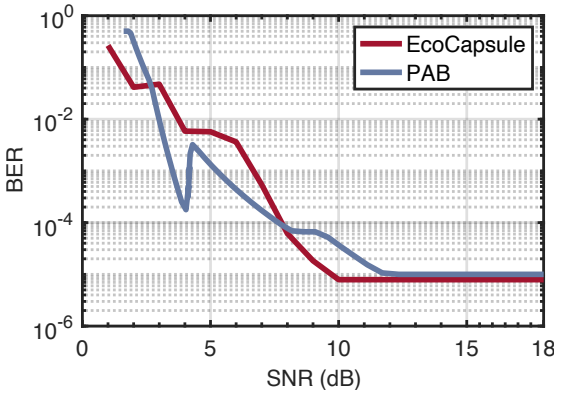

Fig. 3.18: BER vs. SNR

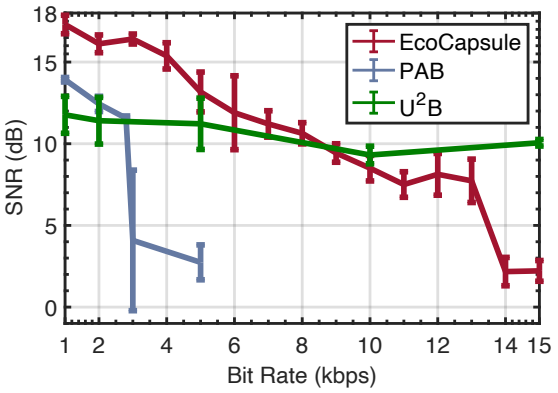

Fig. 3.19: SNR vs Bitrate

of communication systems, especially in challenging environments such as within concrete structures. The experiment involved adjusting the SNR by varying the input peak voltage to the transmitting PZT of the reader, simulating different levels of signal strength relative to background noise. Fig. 3.18 presents the BER, plotted on a logarithmic scale, against the SNR values obtained during the tests. In this setup, the BER is calculated as the ratio of incorrectly decoded bits to the total number of transmitted bits from an EcoCapsule node to the reader. This metric provides a quantitative measure of the transmission accuracy under various noise conditions. The results demonstrate a clear trend consistent with both underwater and in-concrete piezoelectric backscatter systems: the BER decreases as the SNR increases. Notably, the reader system is capable of tolerating a minimum SNR of about 2 dB, at which point the BER approaches 0.5. As the SNR improves beyond this threshold, there is a significant enhancement in performance, with the BER dropping to a minimum of 10^{-5} at SNRs exceeding 8 dB. This level of performance is quite comparable to that of the PAB system, which shows optimal performance at an SNR of 11 dB.

SNR vs. Bitrate: Understanding the impact of bitrate on the SNR of an uplink signal is crucial for optimizing data transmission efficiency. To explore this, we systematically varied the bitrates from 1 kbps to 15 kbps by adjusting the MCU clocks. Each setting was tested across ten trials, and the results, including average SNRs with standard deviations, are depicted in Fig. 3.19. We observed that the SNR for

the EcoCapsule drops sharply to 3 dB as the bitrate exceeds 13 kbps. This performance surpasses that of the PAB system, which is limited to a maximum bitrate of 3 kbps, likely due to our use of a higher carrier frequency (230 kHz), which supports a broader data bandwidth. Conversely, another underwater backscatter system, U^2B [31], demonstrates superior SNR at bitrates above 9 kbps due to its use of an even wider bandwidth.

Throughput vs. Concrete: The type of concrete material plays a significant role in the performance of embedded EcoCapsules, particularly in terms of data throughput. We measured the throughput across EcoCapsules embedded in three types of 15 cm thick concrete blocks—NC, UHPC, and UHPFRC—as shown in Fig. 3.6(a). The results, displayed in Fig. 3.20, show that throughputs exceed 13 kbps with deviations around 2 kbps. Consistently, blocks made of UHPFRC and UHPC, which have higher densities and, therefore, greater impedance, support better propagation of elastic waves, resulting in about 2 kbps higher throughput compared to NC.

SNR vs. Position: Positioning of EcoCapsules within concrete structures significantly affects channel quality due to variations in wave reflection. We conducted tests by affixing NC blocks containing nodes near the top, middle, and bottom margins of a wall, maintaining similar distances between the reader and the nodes. Fig. 3.21 presents the Cumulative Distribution Functions (CDFs) of SNR for these positions. Nodes near the margins achieved higher SNRs—11 dB and 8 dB—compared to those in the middle at 7 dB, attributed to enhanced power harvesting from S-wave reflections at the edges. However, these reflections can also introduce challenges such as increased self-interference and complicating signal decoding. Adjusting the position of the reader's transmitting TX may help mitigate destructive superposition effects caused by these reflections, optimizing signal clarity and overall system performance.

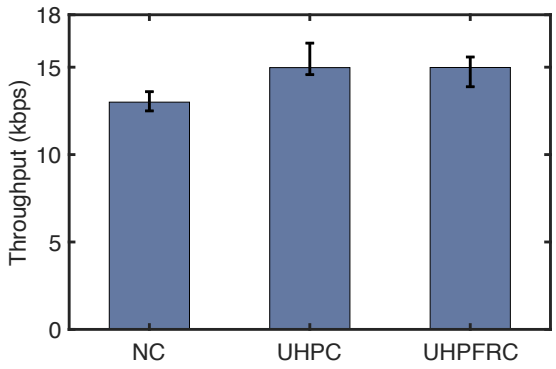

Fig. 3.20: Throughputs

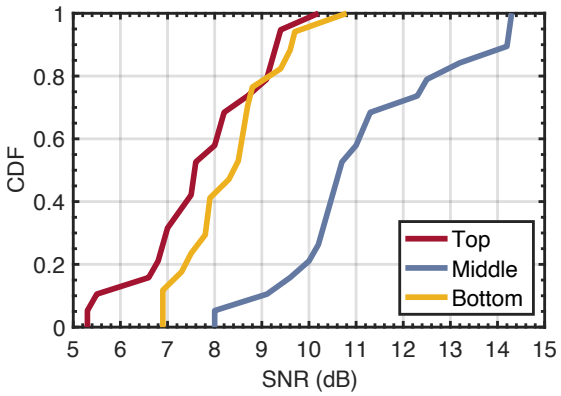

Fig. 3.21: SNR vs. position

3.6.4 Downlink Performance Evaluation

To comprehensively understand the downlink performance of our system, particularly regarding the effectiveness of the wave prism and the modulation scheme, we conducted controlled experiments using only the transmitting and receiving PZTs on either side of a 15 cm thick concrete wall. This setup ensures the exclusion of interference from surface waves and the uncertainty of the EcoCapsule nodes.

Prism Effectiveness: In these tests, we explored the impact of different incident angles of the wave prism on the SNR of the received signal. Fig. 3.13(c) illustrates various prism designs with different incident planes used in the experiment. The experimental results, presented in Fig. 3.22, confirmed our theoretical predictions regarding optimal incident angles. Specifically, the SNR peaked at 15 dB around the 50° and 70° incident angles, aligning well with the theoretically advantageous range of $[34°, 73°]$. At lower incident angles, such as 15° and 30°, the SNR significantly decreased by 73% and 30%, respectively, likely due to the simultaneous triggering of both P-waves and S-waves. Notably, a high SNR was also observed at a 0° incident angle, where the transmitting PZT was directly adhered to the wall without a prism, thus only introducing P-waves into the wall and avoiding the generation of S-waves. This set of results highlights the prism's capacity to enhance SNR by $30 \sim 70\%$ depending on the angle of incidence.

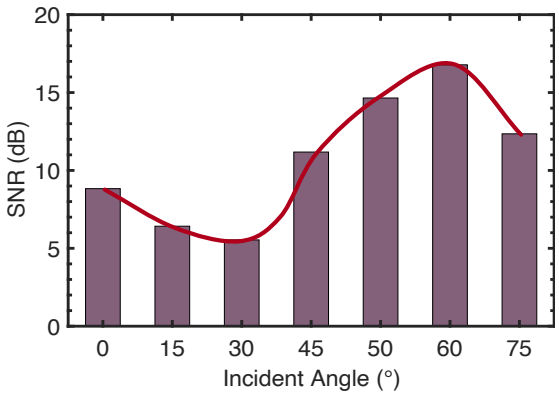

Fig. 3.22: Effect of prism

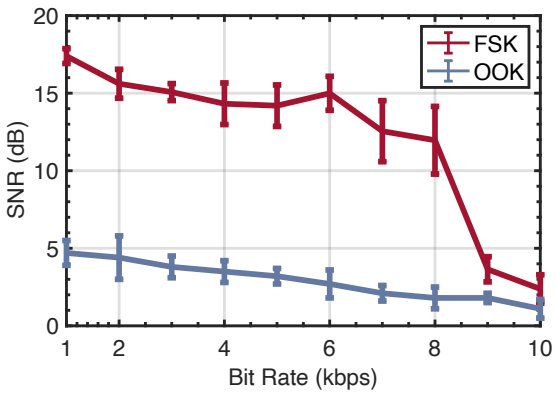

Fig. 3.23: SNR vs. modulation

Anti-ring-effect: Further, we assessed the effectiveness of the anti-ring-effect technique in improving downlink signal quality. This approach involves transmitting PIE-encoded bits using FSK while the receiver decodes the signal using OOK. Fig. 3.23 illustrates how the SNR of the downlink signals varied with bitrate. The results indicated that the FSK method, by leveraging the off-resonance effects, significantly suppressed the signal tailing, leading to an SNR improvement of approximately $3 \sim 5$ times compared to the traditional OOK method. This substantial enhancement confirms the utility of FSK in mitigating the effects of prolonged signal decay typically observed in OOK systems.

3.6.5 Pilot Study: Long-Term SHM of a Real-Life Footbridge

We collaborate with the Department of Civil and Environmental Engineering at the Hong Kong Polytechnic University and have been conducting a pilot study on long-term structural health monitoring of a real-life footbridge [2]. Fig. 3.25 shows the structure of the footbridge [2]. The footbridge links two large-area two campuses. The bridge has a total length of 84.24 m, consisting of a 64.26 m-long main span that straddles the highway underneath and a 19.98 m-long side span. The bridge deck is constructed with two butterfly-shaped steel tube arches and two crossing columns.

The maximum vertical acceleration and lateral acceleration of the bridge deck do not exceed 0.7 m/s^2 and 0.15 m/s^2, respectively. The maximum strength of steelwork is 355 MPa. The limitation of deflection at mid-span is 0.1083 m. The maximum average pedestrian area occupancy must be less than 1 m^2/ped. Once these structural thresholds are exceeded, the whole bridge must be damaged or even collapsed. To conduct the SHM, 88 conventional SHM sensors of 13 types are installed on the bridge, as shown in Fig. 3.25. Fig. 3.24 (a) and (b) show the samples of the two kinds of measurements (i.e., acceleration and stress) during July 2021. Particularly, we observe the exceptions during the window from 15th to 23rd July when the city experienced almost one week-long stormy and tropical weather according to the records of the astronomical observatory. The similar patterns shown in the two data types mutually verify that the two sensors are running functionally.

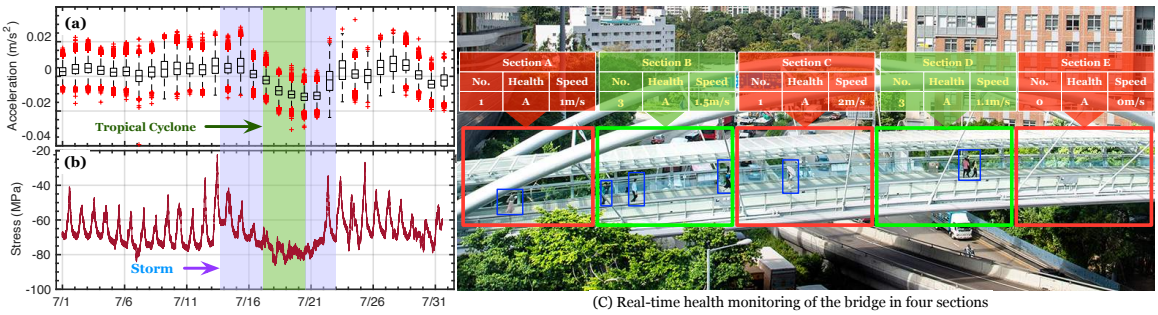

Fig. 3.24: A pilot study of real-time SHM on a footbridge. (a) and (b) shows the collected acceleration and stress measurements in July 2021. The sign of the data depends on the posture of the sensor; (c) shows the picture of the footbridge and the real-time analysis results of bridge health regarding different sections.

Conventional Sensors vs. Self-sensing Concrete: The conventional sensors totally cost over 10 M USD, and they collect external structural parameters only. Nevertheless, our EcoCapsule sensors cost less than 1K USD in total and are the sole ones that can measure the acceleration and stress from the inside. To validate their functionalities, we deployed five EcoCapsules on the concrete for preliminary tests. Since EcoCapsules are supposed to be implanted into the bridge, they do not receive negative influence from weather conditions or man-made interference.

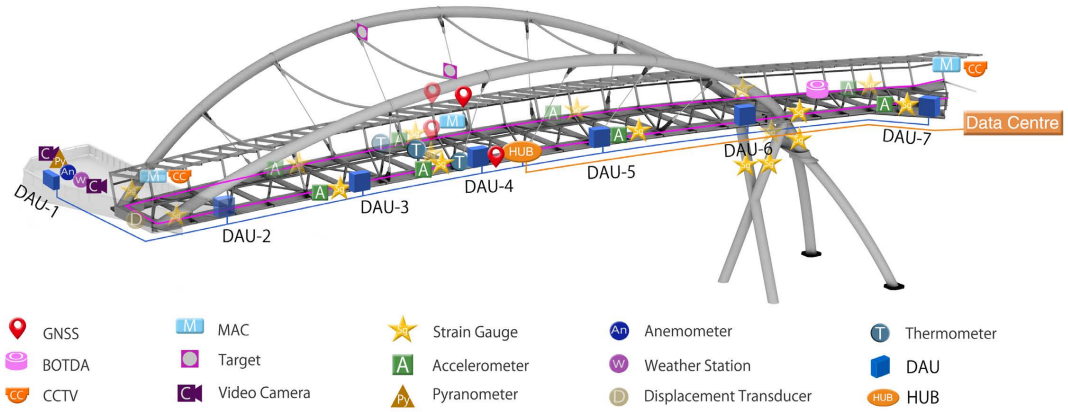

Fig. 3.25: Layout of sensors deployed on the bridge [2]

Table 3.2: Level of structural health based on pedestrian area occupancy. (m^2/ped). This table shows the relationship between average area on the bridge occupied by each pedestrian and the degree of health of the bridge in different regions or countries.

Health	United States	Hong Kong	Bangkok	Manila
A	>3.85	>3.25	>2.38	>3.25
B	3.85-2.3	3.85-2.16	2.38-1.60	3.25-2.05
C	2.30-1.39	2.16-1.40	1.60-0.98	2.05-1.65
D	1.39-0.93	1.40-0.80	0.98-0.65	1.65-1.25
E	0.93-0.46	0.80-0.52	0.65-0.37	1.25-0.56
F	<0.46	<0.52	<0.37	<0.56

Therefore, they are more trustworthy than conventional sensors and benefit from reducing false positives. Fig. 3.26 plots the received and demodulated baseband signal. The EcoCapsule starts to backscatter from 4 ms. In the following, a standard square signal comprises two alternative amplitudes caused by the impedance switch. Each of the high- and low-voltage edges takes 0.5 ms. It can be seen that the reader can successfully establish communication with the EcoCapsule when placed inside the concrete. This study verifies that EcoCapsules can work as well as the conventional ones for long-term monitoring but at a lower price. In the future, we will continue to conduct more structural analysis in sophisticated cases using EcoCapsules.

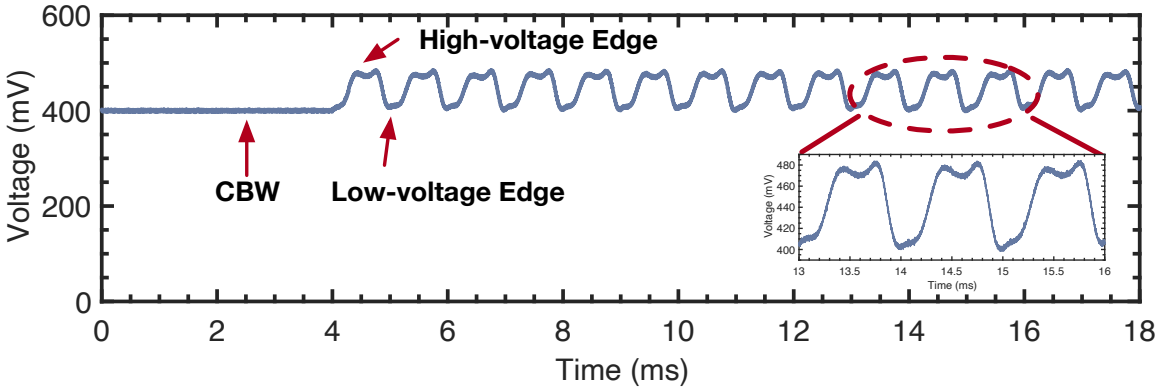

Fig. 3.26: Received and demodulated backscatter signal.

Assessing Bridge Health Through Pedestrian Area Occupancy: One critical metric for evaluating the structural health of bridges is the pedestrian area occupied (H), measured in square meters per pedestrian. As detailed in Table 3.2 and defined in recent research [109], this metric helps classify bridge health into six distinct grades from A to F, with specific thresholds that indicate varying levels of structural integrity and safety. When $H > 2$, the bridge is considered in excellent health, indicating sufficient space per pedestrian and minimal stress on the structure. As H decreases below 2, the bridge is increasingly categorized from good to poor health, suggesting rising levels of crowding and potential for structural stress. When $H \leq 1$, the bridge is deemed overloaded and at imminent risk of collapse due to excessive pedestrian load.

Traditional methods such as Closed-Circuit Television (CCTV) systems are often insufficient for accurate pedestrian counting, as their effectiveness can be compromised by blockages, inadequate lighting, and adverse weather conditions. To address these limitations, our approach integrates data from multiple sources, including real-time measurements from acceleration, stress, and displacement sensors, along with visual data from CCTVs, to compute H accurately. This comprehensive method ensures a more reliable assessment of the bridge's health by considering both structural and usage parameters.

Fig. 3.24 (c) presents a visual analysis of the bridge, segmented into five sections

with corresponding health ratings over the past year. Remarkably, the health grades have consistently remained at level B or above. This sustained level of health is largely attributed to the reduced pedestrian traffic following public health policies on social distancing during the COVID-19 pandemic. Such measures have inadvertently relieved structural stress by reducing the number of users on the bridge, thereby maintaining higher H values and preventing degradation of the bridge's integrity.

By leveraging a combination of sensor data and CCTV analysis, this methodology not only enhances the accuracy of real-time health monitoring but also supports proactive maintenance strategies. It allows for timely interventions that can prevent structural failures, ensuring the safety and longevity of critical infrastructure like bridges.

Sensor Deployment and Data Acquisition: To facilitate detailed monitoring and accurate health grading, a comprehensive sensor network is installed on the bridge. As shown in Fig. 3.25, the deployment comprises 88 conventional external sensors that monitor a range of environmental parameters, structural loads, and bridge responses. Environmental Parameters include air temperature, air pressure, humidity, precipitation, and solar radiation. These factors can significantly affect the material properties of the bridge and its load-bearing capacity. Loads, including wind and structural temperature, are monitored to assess external forces and thermal effects that may influence bridge behavior. Bridge responses include critical structural responses such as stress/strain, displacement, and acceleration, which are continuously recorded to evaluate the physical state of the bridge under various load conditions.

Additionally, specific response data collected in July 2021 is illustrated in figures from Fig. 3.27 to Fig. 3.37. This data provides valuable insights into the dynamic interactions between environmental loads and structural responses, facilitating a comprehensive understanding of the bridge's behavior under typical operational conditions.

By integrating real-time data from these diverse monitoring sources, the implemented sensor network not only supports the PAO-based grading system but also enhances

the predictive maintenance capabilities of bridge management systems. This approach ensures that potential issues can be identified and addressed before they escalate into serious structural concerns, thereby extending the lifespan of the infrastructure and ensuring the safety of its users.

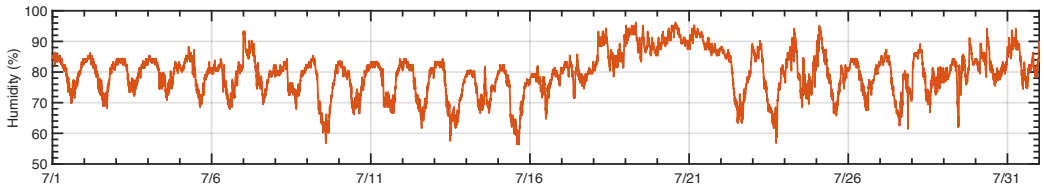

Fig. 3.27: Humidity Sensor

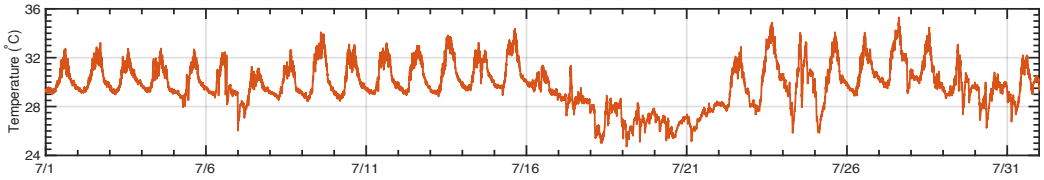

Fig. 3.28: Temperature Sensor

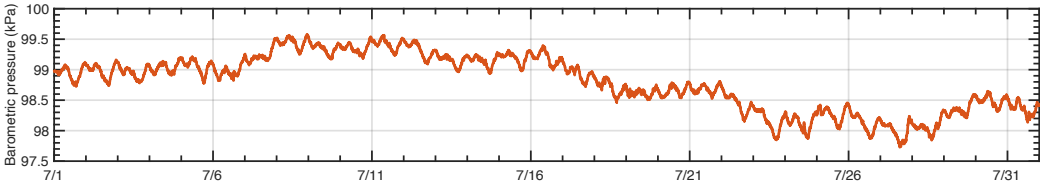

Fig. 3.29: Barometric Pressure Sensor

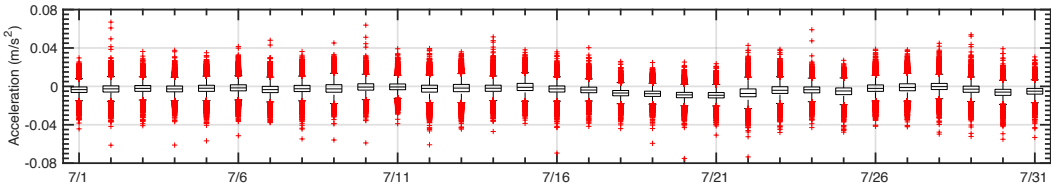

Fig. 3.30: Acceleration from Sensor #1

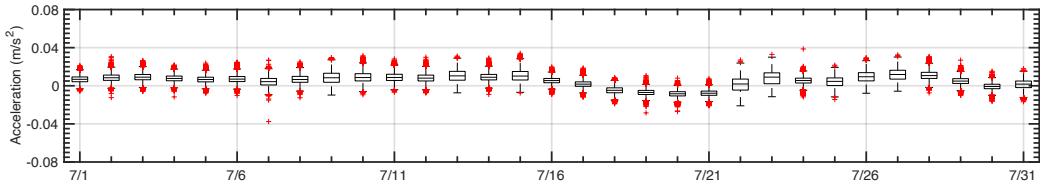

Fig. 3.31: Acceleration from Sensor #2

3.6.6 Future work

In-concrete Destruction and Damage Imaging: While our current system effectively detects various SHM-related indicators, the coverage area is constrained by the

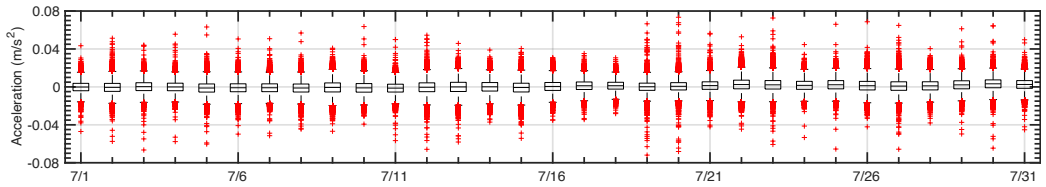

Fig. 3.32: Acceleration from Sensor #3

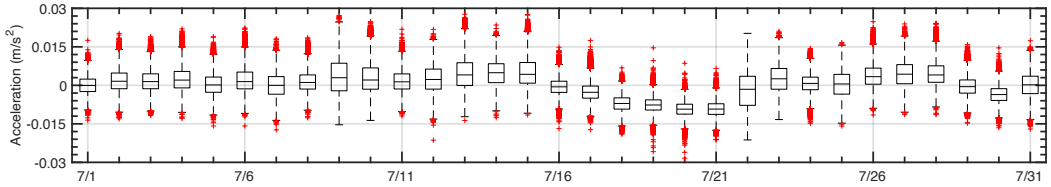

Fig. 3.33: Accelerometer from Sensor #4

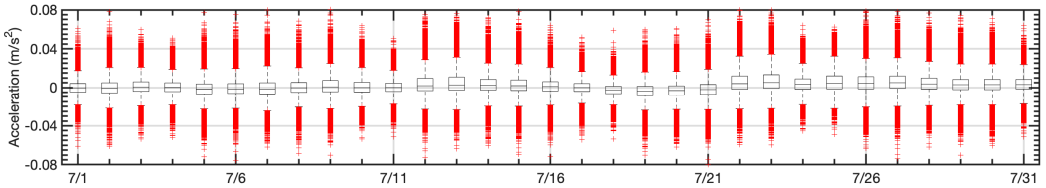

Fig. 3.34: Acceleration from Sensor #5

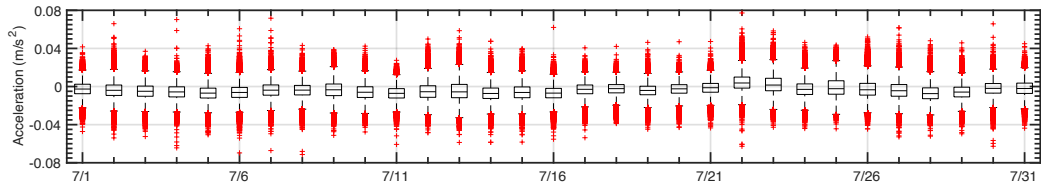

Fig. 3.35: Acceleration from Sensor #6

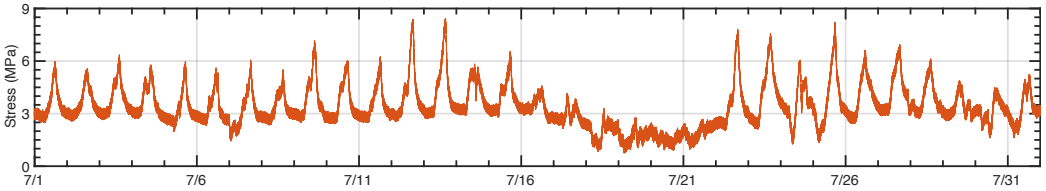

Fig. 3.36: Stress measurements from Sensor #1

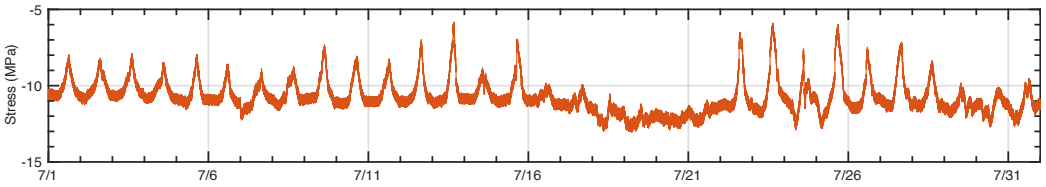

Fig. 3.37: Stress measurements from Sensor #2

limited working range of the sensors. In practical SHM applications, relying solely on sensor data may not suffice. Construction experts often employ nondestructive imaging techniques to ascertain the type and location of structural damage more precisely, enabling them to implement the most cost-effective repair strategies.

To enhance the diagnostic capabilities of our system, we plan to integrate imaging technology that utilizes variations in the backscattered signal to detect and localize damage. By analyzing changes such as time delays in the time domain or spectral energy variations in the frequency domain, we can pinpoint damage locations more accurately. Furthermore, imaging the internal structure of concrete can be achieved by superimposing signals from multiple EcoCapsules, providing a comprehensive visualization of the damage.

This integrated approach not only augments the effectiveness of current SHM practices but also sets the stage for more advanced applications in environments where traditional monitoring systems may fall short. By continuing to develop and refine these technologies, we aim to provide robust tools for infrastructure maintenance and safety, ultimately contributing to the longevity and resilience of built environments.

Chapter 4

Cross-medium Networking via Mechanical Antenna

4.1 Introduction

The imminent deployment of 6G wireless networks is poised to revolutionize global connectivity by achieving universal accessibility, ultra-high-speed data transfer, and minimal latency, essential for the seamless integration with the Internet of Everything (IoE) [110, 111]. This transformative vision requires the facilitation of seamless network integration across various physical mediums including terrestrial, aerial, subterranean, in-body, and aquatic environments. However, the development of cross-medium networks is hindered by substantial challenges such as severe signal attenuation, asynchronous propagation delays, unexpected interference, and the necessity for specialized hardware configurations.

Recent advancements have been focused on enhancing cross-medium communication capabilities, vital for interconnecting disparate transmission environments. This thesis concentrates on air-to-water communication modalities. Conventionally, communication across these mediums has relied on the utilization of relay devices that

are strategically placed at the interface—partially submerged—to bridge the communication gap. These devices collect data from underwater sensors through acoustic transmissions and relay this information to terrestrial stations via radio frequencies [112, 113]. However, the susceptibility of these relays to displacement by oceanic currents necessitates frequent recalibrations, which escalates operational costs and introduces complexities that hinder scalability.

In response, recent innovations have shifted towards establishing direct air-to-water communications. Notable examples include TARF, which employs millimeter-wave technology to sense displacements on the water surface caused by subsurface acoustic signals [48]. Similarly, AmphiLight utilizes bidirectional laser communications between aerial drones and aquatic robots to facilitate data transfer [114], while Shrimp leverages circularly polarized light for visible light communication across mediums [115]. Despite the ingenuity of these approaches, they are often constrained by limitations in range, data throughput, cost-efficiency, alignment precision, and environmental impact.

Furthermore, there is an increasing imperative to monitor the structural health of architectural frameworks by assessing parameters such as temperature, humidity, and structural stresses [116–118], as well as to capture critical physiological signals from within the human body.

What prevents us from utilizing RF signals for cross-medium communication without a relay? The principal challenge lies in the inherent properties of the water medium, particularly salt water, which exhibits high conductivity and an elevated dielectric constant. These characteristics lead to the rapid attenuation of RF signals as they traverse through water, significantly limiting communication range and degrading performance. The interaction of RF signals with water involves not only absorption by water molecules but also scattering from suspended particles and reflection off boundaries like the water surface and seafloor. This attenuation is notably more severe at higher frequencies, which impedes the practical application of RF signals

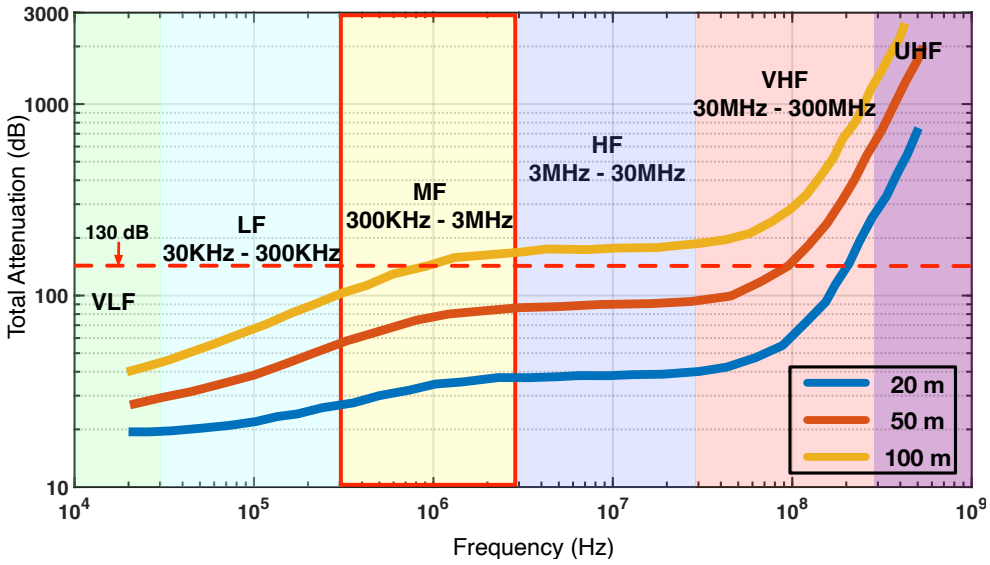

Fig. 4.1: Attenuation of RF signals as a function of frequency. The receiver is positioned above the water surface, whereas the transmitter is submerged underwater at varying depths of 20, 50, and 100 m. The original data are reformed from [3].

for underwater communication scenarios.

Considering a maximum TX power of 30 dBm (i.e., 1 W) and a RX sensitivity of approximately −100 dBm, signals experiencing attenuation greater than 130 dB become indistinguishable. As illustrated in Fig. 4.1, RF signals undergo more than 1000 dB of attenuation within just 50 m at the UHF band, specifically around 915 MHz within the unlicensed ISM band. A similar degree of signal degradation occurs at both VHF and HF bands, thus challenging the feasibility of direct RF communication across air-to-water interfaces.

Upon examination of Fig. 4.1, it is evident that, even at depths up to 50 m underwater, the attenuation within the medium-frequency (MF, 300 kHz - 3 MHz) band remains below 130 dB. The average attenuation at this depth is approximately 80 dB, which is comparably close to the RF attenuation experienced in air (e.g., approximately 78 dB at 2.4 GHz over a distance of 100 m). Given these observations, the MF band emerges as a potentially suitable choice for underwater or air-to-water communication. Medium-frequency radios, with a historical lineage extending back to the early 20th century, are capable of transmitting signals over distances up to 300 km,

penetrating buildings, and spanning seas. Due to their extensive range and profound penetration capabilities, MF radios have been traditionally utilized for nationwide AM broadcasting.

However, conventional wisdom posits that the size of the electrical antenna (EA) should be commensurate with the MF wavelength. The Chu–Harrington limit [119, 120] stipulates that an EA measuring 10-100 m in length would be required to effectively operate within the underwater MF band. Even with a compact antenna design, where the length is reduced to one-tenth of the wavelength (i.e., approximately 1 m), the size remains prohibitively large for applications in compact underwater robotics or wireless sensor networks (WSN). Thus, the feasibility of achieving direct air-to-water communication using MF electromagnetic (EM) signals is severely limited by these substantial antenna size requirements.

In this study, we explore the potential of the MF band to facilitate a cross-medium communication solution by challenging the constraints imposed by antenna size. The underlying principles of electromagnetic fields, as formulated by James Clerk Maxwell's equations, suggest that any time-varying electric fields engender magnetic fields and vice versa. Theoretically, any regular oscillation of electric charges can generate fluctuating electric and magnetic fields that propagate as EM radiation through various mediums. Leveraging this principle, we introduce the concept of a *mechanical antenna* (MA). This innovative antenna type utilizes continuous mechanical motion to oscillate charges, thereby inducing time-varying EM waves. By circumventing the size limitations inherent in traditional EAs, this approach enables the realization of MF radio transmission using a miniaturized MA.

With this innovative approach in mind, we developed *MeAnt*, a versatile IoT platform engineered specifically for direct cross-medium communication utilizing piezoelectric-based mechanical antennas (Piezo-MAs). This platform is designed to transmit across a diverse array of mediums, including water, soil, concrete, biological tissue, and more, capitalizing on the exceptional penetration capabilities of MF radios facilitated

by MAs.

However, transforming this concept into a practical system presents three primary challenges:

- **Interference Mitigation:** The communication bandwidth of MeAnt coincides with the frequency range of civilian AM broadcasts, which increases the likelihood of interference. To counteract this, we implement a chirp spread spectrum (CSS) modulation scheme, which mitigates narrowband AM channel interference.

- **Collision Management:** Although CSS effectively addresses symbol-level collisions, its performance is impeded by the physical characteristics of the Piezo-MA. To resolve this, we introduce a novel carrier sense multiple access with collision avoidance (CSMA/CA) protocol at the link layer. This protocol capitalizes on the unintended vibrational leakage from Piezo-MAs—where a portion of the energy disperses as mechanical fluctuations—as a means for carrier sensing, thus adapting to the unique challenges posed by the unidirectional nature of Piezo-MA.

- **Enhancing Data Integrity:** The integrity of data transmission is jeopardized by factors such as noise, interference, high attenuation, and other channel anomalies, particularly in error-prone environments like water-air interfaces. To address this, we integrate polar codes into the MeAnt system. Polar codes are a state-of-the-art forward error correction (FEC) technique that utilizes the polarization of virtual channels in opposing directions to ensure that informative bits are transmitted through the most reliable channels.

Contribution. In this study, we introduce *MeAnt*, a versatile platform designed for cross-medium communication that harnesses the distinctive capabilities of Piezo-MAs. This comprehensive system is supported by theoretical frameworks and vali-

dated through meticulous experimental procedures. It represents a novel contribution to the field by enhancing the practical understanding of Piezo-MAs within real-life scenarios. Through the development and deployment of MeAnt, we demonstrate the feasibility of using mechanical motion to generate and propagate EM waves across various mediums, thus offering a groundbreaking approach to overcoming traditional barriers in wireless communication.

4.2 From Vibration to Radiation

This section provides an overview of the basic radiation principles of MAs, with a specific focus on the Piezo-MAs. We delve into the operational mechanisms that enable these antennas to generate and radiate electromagnetic waves through mechanical oscillations. Additionally, we present preliminary experiments conducted to verify the feasibility of using Piezo-MAs for cross-medium communication. These experiments are designed to assess the performance and reliability of Piezo-MAs in transmitting signals across different mediums, thereby substantiating their potential in practical applications.

4.2.1 Mechanical Antennas

Unlike traditional EAs that rely on oscillating electronic currents to generate EM radiation, MAs utilize mechanical energy to drive the regular movement of charges or magnetic dipoles, thus producing EM radiation. Current implementations of MAs can be broadly categorized into three groups based on the materials used in their fabrication: electret-based MAs, magnet-based MAs, and piezoelectric-based MAs [121]. An electret-based MA employs a dielectric material to store space charge or maintain an electric dipole orientation, whereas a magnet-based MA uses a permanent magnet. Both types typically involve mechanical rotation, often via a motor, to facilitate EM

radiation generation. In contrast, a piezoelectric-based MA, or Piezo-MA, leverages the vibrations produced by piezoelectric materials (PZMs) as the primary mechanism for EM radiation [122–127]. Due to its capability to achieve higher radiation frequencies, the Piezo-MA is particularly noted for its potential to support faster communication rates [121]. Consequently, this study primarily focuses on the Piezo-MA, exploring its application and effectiveness in cross-medium communication scenarios.

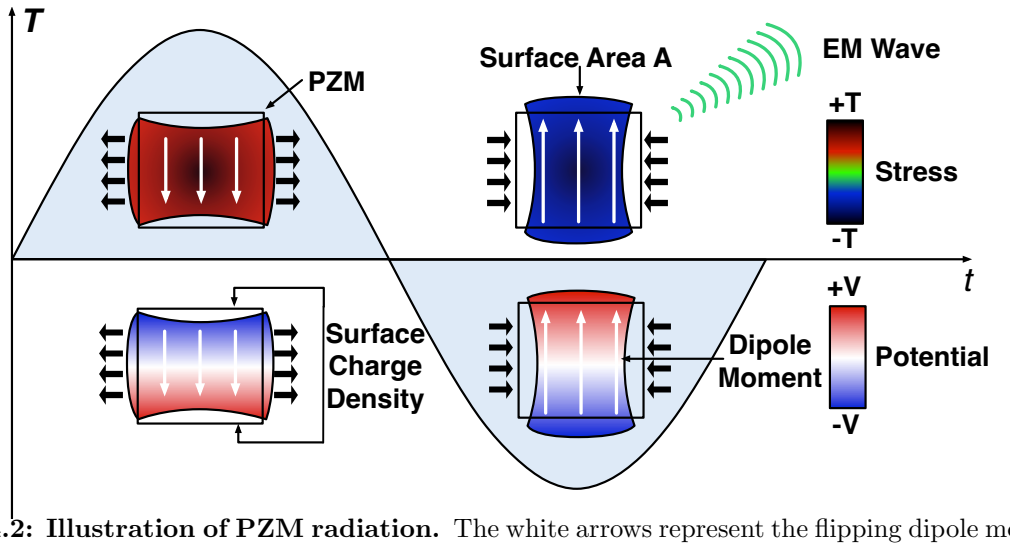

Fig. 4.2: Illustration of PZM radiation. The white arrows represent the flipping dipole moment within the PZM. Continuous flipping yields continuous EM waves.

Piezoelectricity, the conversion between mechanical and electrical energy within dielectric substances, was initially elucidated by the brothers Pierre Curie and Jacques Curie in 1880 [128]. When a sinusoidal mechanical force is applied to a PZM, it induces a cyclic movement of positive and negative electric charges between its electrodes, thereby causing a periodic alteration in the dipole moment. As depicted in Fig. 4.2, during the first half of the cycle, the PZM expands outward, pushing the positive (or negative) charges toward the bottom (or top) surface, thus creating a downward-facing dipole moment. Subsequently, in the latter half of the cycle, the PZM compresses inward, prompting the charges to move toward the opposite surfaces, resulting in an upward-facing dipole moment. This cyclical displacement of charges under a time-varying mechanical force results in a time-varying dipole mo-

ment that oscillates back and forth, thereby generating EM radiation akin to that produced by an EA [129].

To achieve the desired EM radiation, an ultrasound exciter can be utilized to drive the PZM in the following sequence:

$$\text{Power} \overset{\text{Electricity}}{\longrightarrow} \text{Exciter} \overset{\text{Ultrasound}}{\longrightarrow} \text{PZM} \overset{\text{Vibration}}{\longrightarrow} \text{Radiation}$$

However, this process inherently incurs energy losses during the ultrasound's propagation from the exciter to the PZM. To optimize this, we exploit the *inverse piezoelectric effect*:

$$\text{Power} \overset{\text{Electricity}}{\longrightarrow} \text{PZM} \overset{\text{Vibration}}{\longrightarrow} \text{Radiation}$$

When a sinusoidal voltage is applied directly to the PZM, it initiates vibrations through the inverse piezoelectric effect. These vibrations, in turn, activate the piezoelectric effect, leading to the generation of EM radiation. Throughout this transformation, the initial electrical energy is converted to mechanical energy, with a portion further transformed into EM energy, while the remainder dissipates as vibrations. To validate this theoretical model, we simulate the above process using COMSOL Multiphysics [130]. The simulation results are depicted in Fig. 4.3. Fig. 4.3(a) illustrates the surrounding electric field (E-field) strength and direction when a sinusoidal voltage is applied to a PZM, confirming our theory. Fig. 4.3(b) displays the stress response on the PZM subsequent to the application of the sinusoidal voltage.

Initially, the operational principle of a Piezo-MA might appear similar to that of an electrical dipole antenna (EDA), where both antenna types connect their ends to positive and negative terminals, respectively. However, their underlying radiation mechanisms differ significantly. A conventional EDA consists of two *conductive* elements, each of equal length and arranged in parallel. In this configuration, the current within the EDA propagates at the speed of light, necessitating a length that corresponds to a quarter or half of the EM wave's wavelength to achieve resonant frequency and thus enhance radiation efficiency.

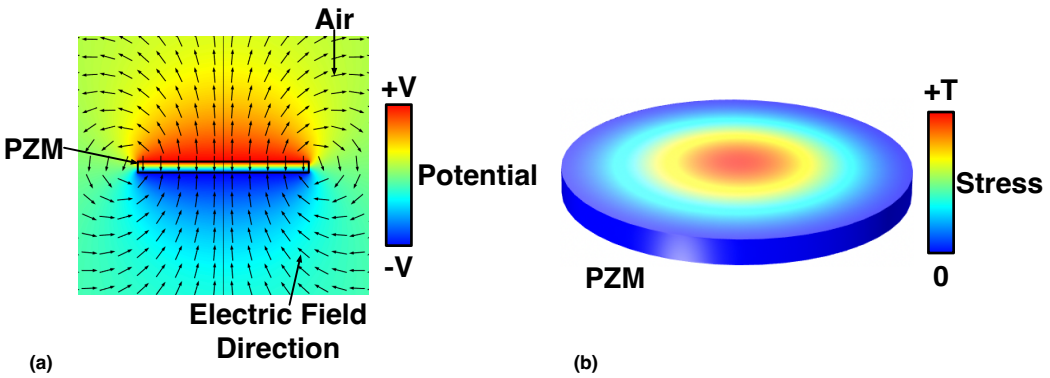

Fig. 4.3: COMSOL Multiphysics Simulation.(a) shows the electric field potential and direction around a working Piezo-MA. (b) shows the stress on the PZM when an electric excitation is applied to it.

Conversely, a Piezo-MA is composed of *non-conductive* piezoelectric materials (PZM), where the movement of charges is governed by mechanical vibrations instead of the speed of light. The mechanical waves within the PZM propagate at the *sound velocity*, which is significantly slower—approximately 10^5 times slower—than the speed of light. This vast difference in propagation speeds means that the resonant frequency of the Piezo-MA is also 10^5 times lower than that of a conventional EDA, making it feasible to size the antenna appropriately for MF EM radiation. Additionally, the resonant impedances of Piezo-MAs are more easily matched to their driving electronics, which obviates the need for the bulky and often inefficient matching circuits typically required by EDAs [123].

Furthermore, it is crucial to address the *unidirectionality* of mechanical antennas (MAs) in terms of communication capabilities. The process of converting mechanical to electrical energy in an MA is inherently non-reversible. Specifically, incoming EM radiation does not induce detectable vibrations in the PZM due to insufficient power levels, thus demonstrating a significant insensitivity of the PZM to vibrations caused by EM signals [131, 132]. Although the PZM is equipped with dual surface electrodes on opposing sides, resembling a parallel plate capacitor, this configuration is primarily effective only for detecting very low-frequency signals (e.g., 50/60 Hz EM leakage from power transmission lines), which predominantly originate as interferences from power

transmission lines. This inherent limitation in the reception capability confines the MA to applications where only transmission is required, rendering Piezo-MA devices predominantly unidirectional and unable to receive MF EM signals. Despite this limitation, the unidirectional nature of Piezo-MA makes it an ideal choice for WSN scenarios, where the focus is primarily on transmitting important uplink sensor data. The advantages of using Piezo-MA in such contexts include energy efficiency, reduced size, and efficient data management, which are critical for the successful deployment of numerous WSNs.

4.2.2 Radiation Model

The Piezo-MA can be effectively modeled using the Butterworth Van-Dyke (BVD) equivalent circuit, which is commonly employed to represent acoustic resonances [51]. As illustrated in Fig. 4.4(a), the left segment of the diagram represents the voltage input, the middle portion corresponds to the piezoelectric equivalent circuit intrinsically linked to the antenna's physical properties, and the right segment signifies the attenuation of the EM wave during propagation, akin to a static resistance. When the MA operates at the mechanical resonance point, the circuit can be further simplified, as shown in Fig. 4.4(b). In this simplified model, the transformer is disregarded, mechanical damping is condensed into a single resistor denoted as R_{m}, and the radiative impedance is represented as R_{rad}. This streamlined representation facilitates a clearer understanding of the antenna's behavior at resonance and helps in optimizing its design for enhanced performance.

Additionally, for comparison, the equivalent circuit for a conventional electrical antenna (EA) operating at 1 MHz is shown in Fig. 4.4(c). According to the Chu–Harrington limit [119, 120], the physical size of the EA is inherently related to the Q factor, which is indicative of the antenna's bandwidth and efficiency. An effectively radiating EA typically possesses dimensions exceeding $\frac{1}{10}$ of the electromagnetic (EM)

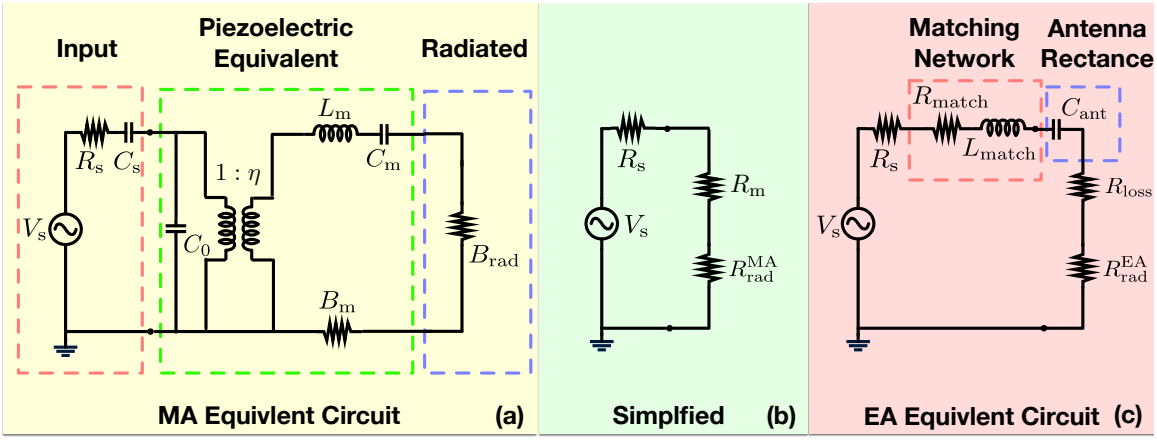

Fig. 4.4: Equivalent circuit of the (a) Piezo-MA, (b) Piezo-MA at mechanical resonance point, and (c) electrical antenna (EA).

wavelength, denoted as λ. However, if the EA size (e.g., 8 cm long) is significantly smaller than 0.1λ (e.g., 30 m), the reactive component of the EA impedance, C_{ant}, increases significantly [133]. To counterbalance the diminutive radiative impedance R_{rad} and substantial reactance C_{ant}, the EA necessitates an extensive tuning network comprising R_{match} and L_{match} to ensure efficient impedance matching. However, this becomes impractical due to the substantial size and lossy nature of the matching circuit at frequencies below 1 MHz, where the physical dimensions of the components and associated energy losses significantly hamper performance.

Following the analysis model proposed in [123, 134], the radiation power of a MA and a comparable EA (denoted by $P_{\text{rad}}^{\text{MA}}$ and $P_{\text{rad}}^{\text{EA}}$, respectively) operating at 1 MHz can be expressed as:

$$\begin{cases} P_{\text{rad}}^{\text{MA}} = \dfrac{|V_s|^2}{2} \dfrac{R_{\text{rad}}^{\text{MA}}}{\left(R_{\text{rad}}^{\text{MA}} + R_m + R_s\right)^2} \\ P_{\text{rad}}^{\text{EA}} = \dfrac{|V_s|^2}{2} \dfrac{R_{\text{rad}}^{\text{EA}}}{\left(R_{\text{rad}}^{\text{EA}} + R_{\text{loss}} + R_{\text{match}} + R_s\right)^2} \end{cases} \tag{4.1}$$

where $R_{\text{rad}}^{\text{MA}}$ and $R_{\text{rad}}^{\text{EA}}$ correspond to the radiation resistances of the MA and the EA, respectively; R_m denotes the mechanical losses of the MA; R_{loss} denotes the conduction or dielectric losses in the EA; R_{match} denotes the tuning network resistance

resulting from the finite Q factor of the matching inductor; R_{s} represents the source resistance, and V_{s} is the input voltage. The matched total antenna efficiency ratio, which is the ratio of radiated power from an MA to radiated power from an EA using the same source, is expressed as follows:

$$\xi = \frac{P_{\mathrm{rad}}^{\mathrm{MA}}}{P_{\mathrm{rad}}^{\mathrm{EA}}} = \frac{R_{\mathrm{rad}}^{\mathrm{MA}}}{R_{\mathrm{rad}}^{\mathrm{EA}}} \frac{\left(R_{\mathrm{rad}}^{\mathrm{EA}} + R_{\mathrm{loss}} + R_{\mathrm{match}} + R_{\mathrm{s}}\right)^2}{\left(R_{\mathrm{rad}}^{\mathrm{MA}} + R_{\mathrm{m}} + R_{\mathrm{s}}\right)^2} \tag{4.2}$$

As a consequence, despite the utilization of matching networks in EAs, which typically comprise low-frequency inductors with quality factors not surpassing a few hundred, the matched impedance perceived by the source remains significantly high, typically within the kilo-ohms range (e.g., $R_{\mathrm{match}} = 23409\,\Omega$). Following the parameters previously proposed [123], such as $R_{\mathrm{rad}}^{\mathrm{MA}} = 6.337 \times 10^{-7}\,\Omega$, $R_{\mathrm{rad}}^{\mathrm{EA}} = 6.126 \times 10^{-8}\,\Omega$, $R_{\mathrm{m}} = 893.39\,\Omega$, $R_{\mathrm{loss}} = 1.726 \times 10^{-5}\,\Omega$, and $R_{\mathrm{s}} = 50\,\Omega$, the substitution of these settings into Eq. 4.2 reveals that an MA with a diameter of 7 cm can radiate 6400× more power than an 8 cm-long EA. This disparity stems from the significant energy consumption of the cumbersome matching circuits required for EAs of similar size operating in the same frequency band, surpassing the energy losses due to vibration leakage in MAs. While EAs are passive and do not directly consume energy, the substantial resistors within their matching circuits incur significant energy loss in the form of heat [135]. For an EA operating in the MF band, the heat power loss due to the matching resistor is represented as $R_{\mathrm{match}} = 23409\,\Omega$, according to Eq. 4.2. Conversely, for the MA, the additional energy expenditure due to vibration leakage is modeled as $R_{\mathrm{m}} = 893.39\,\Omega$, which is far less than the heat loss experienced by a similarly sized EA.

Discussion. One might wonder why an AM radio receiver [136] can effectively utilize a relatively short EA for signal reception. In the realm of AM broadcasting, a crucial disparity exists between transmitting and receiving antennas. Transmitting antennas, such as radiating towers, are typically quite large and are designed to optimize

the Voltage Standing Wave Ratio (VSWR) to ensure efficient energy radiation while minimizing heat generation [135]. These antennas are engineered to maximize their effectiveness in emitting EM waves across vast distances. In contrast, receiving antennas can be significantly smaller. The primary concern of a receiving antenna is the SNR rather than the efficiency of EM wave capture. Although their efficiency in capturing MF EM waves is relatively low, the inherent noise within this frequency band is minimal, allowing for a consistently high SNR. Furthermore, signal enhancement can be achieved through various hardware and software methods, including filtering and amplification [137]. As a result, small commercial AM receiving antennas, such as those used in AM radios, are not suitable and efficient for AM transmission. Conversely, the Piezo-MA offers a mechanically driven MF transmitting paradigm and represents a miniaturized module capable of transmitting efficiently in that band, albeit lacking the ability to receive MF EM waves. This distinction highlights the specialized roles of antennas in broadcasting and their tailored designs to suit either transmitting or receiving functions effectively. Table. 4.1 discusses the transmitting and receiving capabilities of three antennas in this work, where the Piezo-MA is the only one that maintains both small size and good transmitting capability.

Table 4.1: Transmitting and Receiving Capabilities of Three Antennas in Fig. 4.5

	Piezo-MA	Small EA on AM Radio	Loop Antenna
Transmitting	Very Good	Poor	Poor
Receiving	Poor	Good	Very Good

4.2.3 Feasibility Verification

We conducted a series of feasibility experiments to verify the viability of Piezo-MA for cross-medium communication, as depicted in Fig. 4.5. The experiments employed a commercial off-the-shelf PZT-5 ceramic transducer as the Piezo-MA, designed as a flat cylinder with a volume of $4 \times \pi \times 25^2\,\mathrm{mm}^3$. Operating at a frequency of 550 kHz

with a bandwidth of 20 kHz, the PZT transducer was connected to a Rigol DG2052 50MHz Function Generator [138]. This function generator produced a chirp signal ranging from 470 kHz to 630 kHz with a peak voltage of 20 V, expected to be emitted by the coupled Piezo-MA into the air.

Penetration Test: For reception, we utilized a passive loop antenna [139] with a diameter of up to 56.8 cm. Integrated with an oscilloscope and a narrowband low-noise amplifier, the loop antenna was positioned 2 m away from the Piezo-MA. It was configured to capture EM radiation from the Piezo-MA placed in various environments—airborne, submerged underwater, buried in soil, and concealed behind a concrete wall. In all scenarios except airborne, the Piezo-MA was maintained at a distance of 1 m from the medium's boundary, as illustrated in Fig. 4.6(a). We conducted ten trials for each setting, and the mean result was reported. The outcomes derived from these experiments are illustrated in Fig. 4.6(b), leading to the following findings:

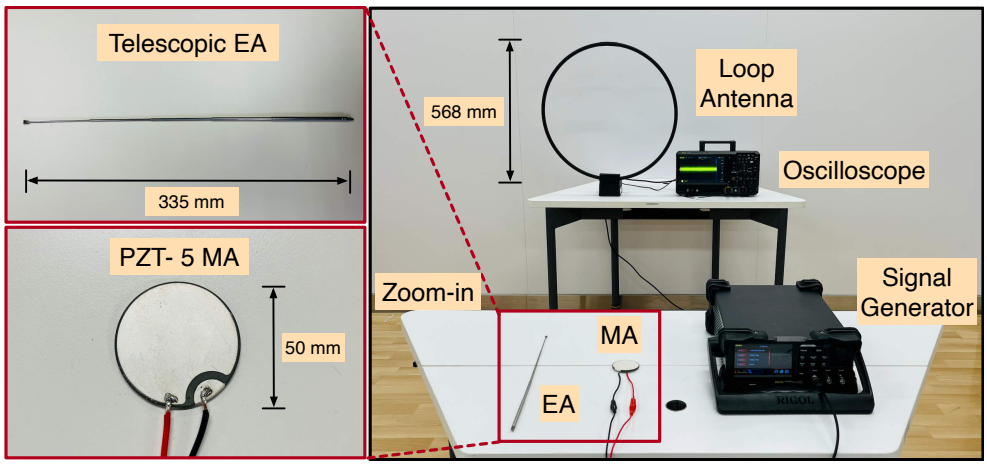

Fig. 4.5: Cross-medium Feasibility Setup

- The Piezo-MA emits EM waves precisely within the resonant band, akin to a conventional wavelength-matched EA. However, its compact size adeptly meets the stringent size limitations of IoT devices, making it especially suitable for embedded applications where space is at a premium.

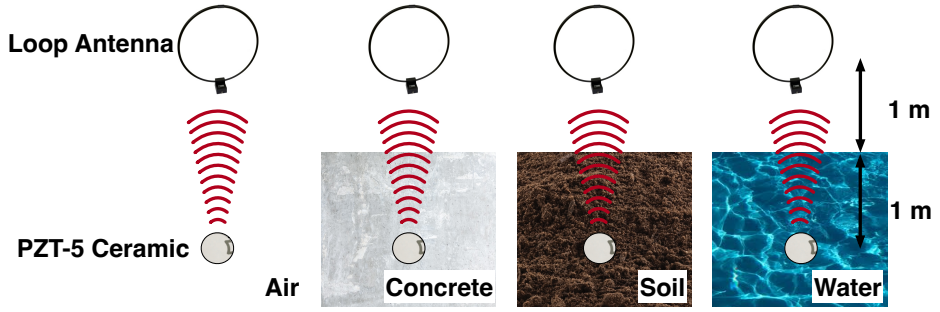

(a) Tested cross-medium scenarios

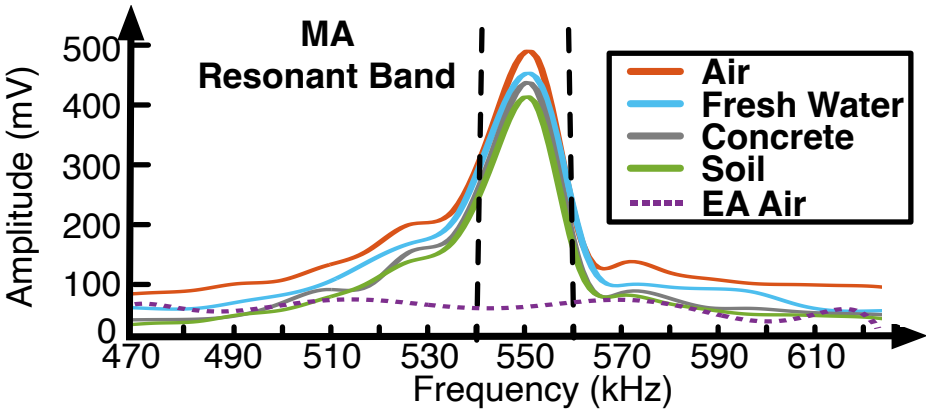

(b) Frequency response

Fig. 4.6: Cross-medium Frequency Response. We collected the frequency responses of four MA-based cross-medium communication scenarios.

- In contrast, a telescopic EA installed on an AM radio receiver (Sony ICF-P36 radio [136]) was also utilized to radiate the MF EM signals. The amplitude of the signals emitted by the EA was found to be nearly 10% of that produced by the Piezo-MA, highlighting the inefficiency of the EA due to the absence of matching circuits. This comparison underlines the superior efficiency of the Piezo-MA in situations where size and power are critical constraints.

- Due to the robust penetration capabilities of medium waves, signals emitted by a Piezo-MA can effectively traverse various mediums. Notably, the attenuation of these signals exhibits minimal fluctuations compared to in-air propagation, indicating consistent propagation characteristics across diverse mediums. This uniformity is particularly beneficial in addressing inherent complexities in cross-

medium communication, such as asynchronous propagation delays.

4.3 MeAnt Design

Despite the innovative concept of MAs, their integration into compact and practical communication networks remains a challenge, primarily due to a spectrum of unique obstacles that span from the physical to application layers. To address these challenges, we introduce MeAnt—a wireless platform that leverages MF EM waves to tackle the complexities posed by harsh environments such as underwater, in-body, and underground settings. The applications of MeAnt are diverse, encompassing domains, including underwater robotics, soil detection, structural health monitoring, and in-body implants. Subsequently, we have formulated a series of protocols, ranging from the Physical Layer (PHY) to the Transport Control Layer (TCL). These protocols are tailored specifically for MeAnt to effectively mitigate the various challenges encountered in these rigorous environments. This holistic approach not only enhances the robustness of the communication system but also ensures its adaptability and efficiency in real-world applications.

4.3.1 PHY: Chirp Spread Spectrum

Using the MF band for communication facilitates robust signal penetration but also presents two significant challenges when actualized in practice.

1. The center frequency utilized by MeAnt, unfortunately, may coincide with the AM radio band. Most AM stations globally operate within the 535 - 1605 kHz range. Taking the Piezo-MA, which works at 550 kHz, as an instance, available data indicate that there are over 100 AM broadcast channels between 500 kHz and 560 kHz, encompassing most of the United States. Such overlap

significantly deteriorates the SNR at the receiver end, resulting in low signal strength and high interference during decoding.

2. The radiations emitted by MAs are excited by mechanical forces, hence subject to the inertia effect. This effect implies that the Piezo-MA continues to vibrate for a certain duration even after the driving voltage is switched off [140, 141]. This lingering vibration, referred to as the "ring effect," causes a prolonged tail at the end of a symbol, leading to severe inter-symbol interference.

These challenges necessitate specific design considerations and operational strategies to optimize MeAnt at the physical layer for effective performance in environments where traditional communication systems might fail.

Modulation. To counteract the aforementioned challenges, we propose the adoption of the CSS modulation scheme. CSS [142–144] enhances communication range and resistance to interference through its distinctive characteristics. In CSS modulation, the transmitted signal is spread across a wide bandwidth using a linearly modulated frequency sweep, known as a chirp. We employ up-chirp, down-chirp, and their sweep time to represent different symbols. Formally, suppose f_1 and f_2 are the starting and ending frequencies, respectively, the time-domain function for the up-chirp and the down-chirp is given by:

$$C(t) = e^{j2\pi\left(f_1 \pm \frac{v}{2}t\right)t} \tag{4.3}$$

where $0 \leq t \leq T$, $v = \frac{f_2 - f_1}{T}$ is the rate of frequency increase (or decrease), and T is the time it takes to sweep from f_1 to f_2. Different symbols are defined by controlling the direction (up or down) of the chirp and the duration T. In our implementation, we define three types of symbols: long-up-chirp (e.g., 4 ms), short-up-chirp (e.g., 1 ms), and short-down-chirp (e.g., 1 ms). Fig. 4.7 presents an example of a received packet, including the preamble, payload, and guard interval. Unlike LoRA's approach of manipulating the initial chirp frequency, we utilize simple up and down chirp modulation due to the Piezo-MA's nature, mitigating heightened intersymbol interference

resulting from frequent frequency mutations. This approach ensures communication robustness through smooth transitional frequency changes within individual symbols.

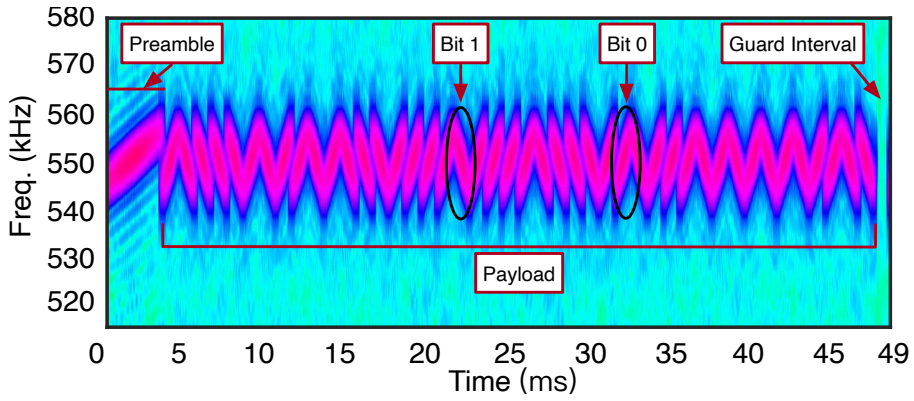

Fig. 4.7: Received Packet of MeAnt

Demodulation. On the receiver side, we first employ a long-down-chirp template to correlate the incoming signal until the apex of the correlation surpasses a pre-established threshold, denoted as δ_{prm}. This surpassing of the threshold indicates the presence of a packet and allows us to determine when the packet starts. Following the detection of the preamble, we proceed to decode the subsequent symbols one by one. Each symbol, with a constant width, is subjected to correlation against the short-up-chirp and short-down-chirp templates. We denote the peak values of these two resultant correlations as C_{up} and C_{down}, respectively. The symbol is considered as bit one if C_{up} exceeds C_{down} and C_{up} is greater than δ_{sym}, which is another user-defined threshold. Conversely, if C_{down} exceeds C_{up} and C_{down} surpasses δ_{sym}, then the symbol is considered to be bit zero. If neither condition is met, the symbol will be erased due to intense interference or noise, denoted by Λ. Hence, the outcomes of the demodulated symbols can be one of three possibilities: 0, 1, or Λ. In other words, we model the cross-medium channel as a binary erasure channel (BEC), with the assumption that the transmitter sends a bit (a zero or a one), and the receiver either receives the bit correctly or, with some error probability p, receives a message that the bit was not received ("erased"). This channel model will be employed later in our analysis to incorporate the forward error correction technique.

Reasons to Choose. CSS-based modulation offers several key advantages for challenging communication settings. By spreading signals across a broad frequency range, CSS inherently reduces the system's vulnerability to specific frequency disturbances. Its unique time-varying 'chirp' signals aid in distinguishing intended communications from potential ambient narrowband interference, such as modulated voices on AM radio. This feature ensures stable communication even under adverse conditions, making CSS particularly suited for environments where signal integrity is frequently compromised. Note that the exemplary performance of CSS comes at the expense of the bitrate. While it provides robustness against interference, the spread-spectrum nature of CSS requires a lower bitrate compared to narrower bandwidth transmissions. It is also feasible to use other modulation schemes, such as Amplitude Shift Keying (ASK) and Frequency Shift Keying (FSK), for specific communication demands that require higher bitrates. These alternatives, while offering faster data transmission rates, may not provide the same level of interference resistance as CSS, highlighting a fundamental trade-off between communication speed and reliability in the design of transmission systems.

4.3.2 DLL: mediums Access Control

Incorporating a mediums Access Control (MAC) protocol (e.g., ALOHA) in the data link layer (DLL) is crucial to allow multiple devices to share the same wireless channel without causing collisions, as shown in Fig. 4.8(a).

Challenges: As detailed in Section 4.2, nodes within the MeAnt network are primarily unidirectional communicators with severely constrained capabilities to receive EM signals, either from gateways or adjacent nodes. Our empirical data reveal that the practical downlink range is limited to approximately 0.5 meters, which poses a formidable challenge for the MAC layer protocol. The absence of downlink feedback mechanisms, crucial for acknowledging packet reception, facilitating retransmissions,

and coordinating access, renders collisions undetectable and retransmission mechanisms non-functional. This deficiency significantly hampers effective channel management and jeopardizes the integrity of transmitted data.

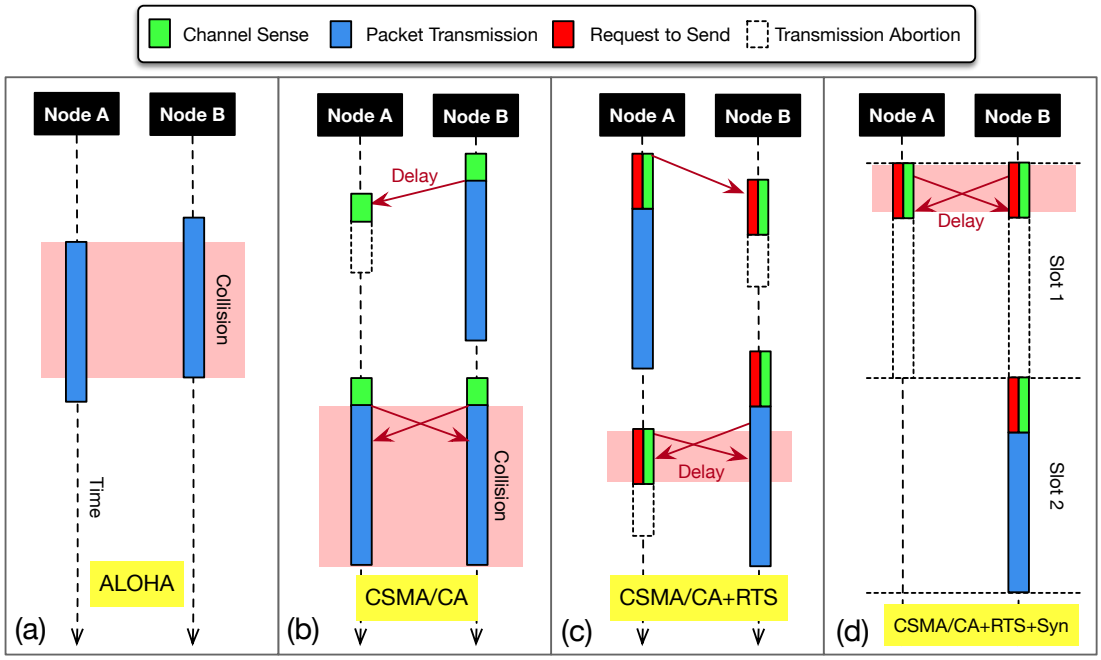

Fig. 4.8: The illustration of mediums access control at the data link layer (a) depicts a potential collision scenario when two nodes initiate packet transmission concurrently. (b) utilizes CSMA/CA to diminish the collision probability, yet collisions might persist when two nodes concurrently assess channel availability. (c) introduces the use of an RTS packet to address the issue of simultaneous channel detection successfully, but it may give rise to brief collisions. (d) introduces synchronization, in which each node must send the RTS packet and perform channel availability checks at the outset of synchronized time slots.

Novel MAC Protocol Implementation: In the design of the MAC protocol for MeAnt, a unique approach is employed by utilizing *vibration leakage* as a means for carrier sensing. As identified earlier, when the Piezo-MA transmits EM radiation, a portion of the energy dissipates as mechanical vibrations. Importantly, PZT transducers are employed as the primary interface for communication between nodes in non-gaseous mediums such as underwater and underground environments. Although the Piezo-MA lacks the capability to directly detect EM signals, it can effectively sense these residual vibrations. This ability signifies underlying EM signal activities, thereby facilitating a novel method of carrier sensing. Our empirical research demonstrates that the Piezo-MA can detect vibration leakage over distances up to

approximately 10 meters underwater, significantly enhancing its carrier sensing capabilities and thereby improving the efficiency of the MAC protocol in challenging environments.

CSMA/CA Protocol Implementation: The adoption of the Carrier Sense Multiple Access with Collision Avoidance (CSMA/CA) protocol in our MAC design is driven by a dual-mode transmission strategy (EM and vibration), aiming at minimizing collision probabilities when multiple nodes attempt simultaneous transmissions. Specifically, each node initiates communication by assessing the availability of the transmission medium. This is achieved by utilizing the Piezo-MA to detect ultrasonic signals indicative of active transmissions within the vicinity. This preemptive sensing is crucial for averting potential collisions. The protocol dictates that if the channel appears busy, the node postpones its transmission for a randomly determined duration, known as the backoff period, which is managed by a backoff counter. The node continuously monitors the channel's status during this interval. If the channel is free when the backoff counter reaches zero, the node proceeds to transmit the packet. Conversely, if the channel remains busy at this juncture, the backoff counter is reset, and the node repeats the assessment and waiting process. This method of dynamically adjusting transmission times based on channel conditions effectively reduces the likelihood of collisions. The detailed operational mechanics of the CSMA/CA protocol are illustrated in Fig. 4.8(b).

CSMA/CA with RTS Enhancement: The implementation of the CSMA/CA protocol often encounters challenges due to the slower propagation speed of ultrasound compared to EM signals, which can lead to synchronization issues among nodes. As illustrated in Fig. 4.8(b), Node A may incorrectly perceive the channel as free due to the absence of detected ultrasound signals within its sensing window. Concurrently, Node B might have commenced its packet transmission, but the ultrasound signal's delay prevents Node A from detecting this in time, resulting in a collision. Extending the sensing window is one potential solution to ensure Node A detects Node B's

activity. However, this approach does not resolve issues when nodes initiate their collision detection simultaneously, and the delay in ultrasound propagation exceeds the difference in their sensing windows, as depicted at the bottom of Fig. 4.8(b). To address these synchronization and detection failures, we introduce the Request to Send (RTS) mechanism. This mechanism involves nodes broadcasting "warning bits" in a brief RTS packet before the actual data transmission begins. The purpose of the RTS packet is to explicitly signal other nodes about a pending transmission. This strategy, showcased at the top of Fig. 4.8(c), effectively mitigates the risk of collisions by improving the coordination between nodes and ensuring more reliable detection of concurrent transmissions.

Centralized Synchronization and Slotted ALOHA Protocol: While the RTS mechanism effectively mitigates many collision issues, it can still inadvertently trigger brief overlaps with ongoing transmissions, as depicted at the bottom of Fig. 4.8(c). To comprehensively address this challenge, the implementation of a centralized control device becomes essential for synchronizing the actions of all nodes within the network. This leads to the adoption of the slotted ALOHA access protocol, where time is divided into discrete slots. Each node is required to initiate transmissions strictly within these designated slots to ensure orderly communication. As illustrated in Fig. 4.8(d), RTS packets are dispatched at the beginning of each slot. This timing prevents the RTS packets from interfering with the ongoing data transmissions, thereby minimizing the risk of collisions. If a node detects an RTS packet from another node during its designated slot, it automatically postpones its transmission to a later slot, chosen randomly, thereby avoiding a direct collision. Additionally, a specific node within the MeAnt system may be assigned the role of a synchronizer. This node emits periodic impulsive signals to delineate the start of each slot, ensuring all nodes align their transmissions accordingly.

This centralized synchronization strategy not only streamlines transmissions but also significantly reduces the likelihood of collisions. The use of predefined time slots,

coupled with centralized control, enhances the overall efficiency and reliability of the communication process. This method is particularly advantageous in environments like underwater or other liquid mediums, where ultrasound propagation plays a critical role in node communication.

Discussion. Throughout this discourse, a tacit assumption has been that all nodes are deployed within the same close-knit medium, ensuring that a node's vibrations are universally detectable by all other network nodes, i.e.,, universal carrier sense is assumed. Naturally, this assumption may not hold in larger deployment areas, leading to what is known as the "hidden node problem." This issue arises when two distant nodes fail to detect each other's presence, potentially leading to simultaneous transmissions that result in collisions. The hidden node problem can be effectively addressed through the implementation of clear-to-send (CTS) signals. These signals enhance communication protocols by ensuring that all nodes within a potentially affected network segment are aware of ongoing transmissions, thereby avoiding collisions. For a detailed exploration of this solution, readers are referred to [145]. Additionally, when two MeAnt networks operating in distinct mediums are deployed in close proximity, there exists a risk of undetectable collisions due to overlapping operational frequencies. To mitigate this issue, we recommend the adoption of different center frequencies for the Piezo-MAs in each network. This frequency separation strategy ensures that the networks operate on distinct bands, reducing the likelihood of interference and enhancing overall network performance.

The MAC protocol designed for the MeAnt network, which operates without downlink communication, presents a significant divergence from traditional WSNs, where downlink support is integral for acknowledging packet reception, retransmissions, and coordination. As a result, this protocol is inherently incompatible with existing WSN protocols that rely on bidirectional communication. To incorporate the MeAnt MAC protocol into existing WSN protocols, a hybrid approach could be considered, where the existing bidirectional communication framework is adapted to handle unidirec-

tional links. One potential solution would involve introducing a new layer or interface that allows for the integration of vibration-based carrier sensing, such as the MeAnt's vibration leakage detection, alongside traditional downlink communication. This would enable compatibility by allowing the MeAnt nodes to function as specialized end devices within a larger WSN infrastructure. In this setup, while the MeAnt nodes would not require downlink communication for packet acknowledgment, the network's gateway or central controller could manage data aggregation, synchronization, and retransmission tasks. This could be achieved through scheduled uplinks from MeAnt nodes, minimizing collisions and allowing the WSN protocol to handle tasks like retransmissions and error corrections through other channels, effectively bridging the gap between the unidirectional MeAnt design and existing WSN systems.

4.3.3 TCL: Transport Integrity

Despite incorporating various mechanisms at both the physical and link layers, packets may still be vulnerable to ambient noise or partial collisions—a challenge inherent to cross-medium communication channels characterized by significant attenuation, instability, and diverse interference sources. To tackle this issue, we introduce an advanced strategy at the transport control layer by integrating forward error correction (FEC) into the packet structure. FEC is a method that involves embedding additional redundant bits into the packet, enabling the correction of bits that become corrupted during transmission.

For our FEC scheme, we select *Polar Codes*, which were introduced by Erdal Arikan in 2009 and have since been recognized for their capacity to approach the Shannon limit [146]. The choice of Polar Codes for the MeAnt system is driven primarily by two considerations. Firstly, Polar Codes achieve near-optimal capacity while maintaining a relatively low computational complexity. This efficiency is crucial for IoT devices, where processing power and energy consumption need to be minimized. Sec-

ondly, Polar Codes are exceptionally effective in managing the complex types of noise typical of cross-medium communication channels, thereby enhancing the robustness and reliability of data transmission.

By employing Polar Codes, we significantly bolster the integrity of data transmitted across our diverse communication environments, ensuring that the MeAnt system remains resilient against the various challenges posed by ambient noise and interference.

Channel Polarization in Polar Codes: In the MeAnt communication model, the PHY is conceptualized as a Binary Erasure Channel (BEC). Polar Codes leverage a transformative technique known as "channel polarization" to enhance communication reliability. This method systematically converts a series of BECs into a set of "virtual" channels, each possessing distinct reliability levels. Specifically, the channel polarization process involves performing XOR operations among different channel bits, which dynamically categorizes these channels into varying probabilities of transmission success. Through this polarization, certain channels emerge as "highly reliable," exhibiting strong probabilities of successful transmission. Conversely, other channels become "less reliable," manifesting weaker transmission success probabilities. During the encoding process, the encoder strategically places more critical data bits onto the highly reliable channels. In contrast, less critical bits, known as frozen bits, are allocated to the less reliable channels. At the receiving end, the decoder utilizes a technique known as successive cancellation to reconstruct the original data. This method effectively deciphers the transmitted bits by approximating the likelihood of bit sequences facilitated by the polarized channel properties. The effective use of channel polarization is grounded in the chain rule of information theory, which expands the mutual information between the transmitted and received sequences, thereby optimizing data recovery even in challenging communication environments.

Fig. 4.9 visually illustrates the channel polarization process. Assume that a physical BEC W has an erasing rate of $p = 0.4$ (or, equivalently, an original channel capacity $I(W) = 0.6$). Note that the channel capacity can be regarded as the successful

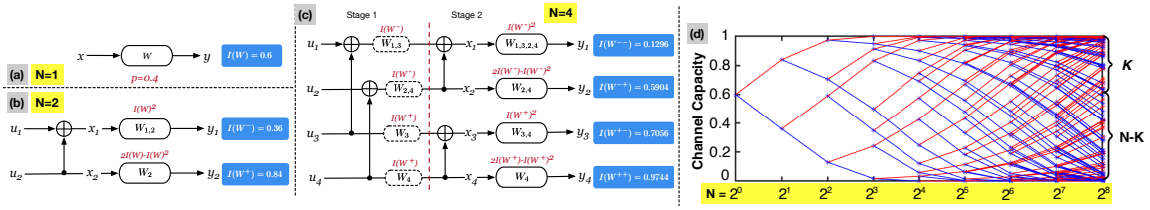

Fig. 4.9: Illustration of Polar Codes. (a) shows the physical channel with a capacity of 0.6. (b) and (c) shows the channel polarization when $N = 2$ and 4, respectively. (d) shows the channel capacity as a function of N. Particularly, the top K most reliable channel can be used to transmit K informative bits, while the remaining less reliable channels are used to transmit frozen bits.

decoding probability. If we have two bits (u_1 and u_2) to transmit, we can generate two virtual channels W^+ (reliable channel) and W^- (unreliable channel), each tasked with transmitting one bit. Fig. 4.9(b) shows that $x_1 = u_1 \oplus u_2$ is transmitted via the W^- channel and $x_2 = u_2$ via the W^+ channel, where $\oplus$ denotes XOR. The probability of successful decoding of the u_1 and u_2 changes due to the XOR operation. Let $I(W^{-(+)})$ denote the channel capacity. Then, u_1 is decoded only when *both* y_1 and y_2 are correctly received, i.e., $I(W^-) = I(W)^2 = 0.36$. Similarly, u_2 is decoded when *either* y_1 or y_2 is correctly received, i.e., $I(W^+) = 2I(W) - I(W)^2 = 0.84$. This transformation process results in the reliable channel having a higher capacity than the original channel (i.e., $2I(W) - I(W)^2 > I(W)$) and the unreliable channel having a lower capacity ($I(W)^2 < I(W)$). The principle of polar codes is to put the information bit on the high-capacity channel W^+ and the known frozen bit on the low-capacity channel W^-. Now, u_1 is fixed to a frozen bit. The receiver aims to decode u_2 through the received codes y_1, y_2 and known u_1, thus achieving higher decoding confidence.

Fig. 4.9(c) extends the transmission scenario to involve four bits (u_1-u_4). This case can be viewed as a cascade of two reliable and two unreliable channels. Initially, u_1 and u_3 are transmitted using a pair of channels, denoted as $W^-_{1,3}$ and $W^+_{1,3}$, while u_2 and u_4 are transmitted via another pair, labeled as $W^-_{2,4}$ and $W^+_{2,4}$. In the subsequent stage, the two pairs of channels form additional combinations: an unreliable channel $W^{--}_{1,2}$ and a reliable channel $W^{-+}_{1,2}$, along with channels $W^{+-}_{3,4}$ and W^{++}, respectively. The probability formulas governing the behavior of these four new virtual channels

are presented in Fig. 4.9(c). Notably, there's an observable polarization of channel capacities, whereby the most reliable channel achieves a capacity of 0.9744, and the least reliable channel diminishes further to 0.1296. Consequently, we designate u_1 and u_2 as frozen bits due to this disparity in channel capacities. This strategic allocation prioritizes critical data transmission over channels with lower error probabilities, thereby fortifying the resilience of the overall data transmission system.

The concept of channel polarization in Polar Codes can be generalized to encompass $N = 2^n$ virtual channels, where $n = 2, 3, 4, \ldots$. This generalization employs a cascading technique that effectively categorizes channels based on their reliability as N increases. As illustrated in Fig. 4.9(d), the capacity of these virtual channels progressively polarizes towards the extremes of 0 or 1 with increasing N. In the theoretical limit of an infinite sequence, the capacities of these channels converge asymptotically to these extremes. This polarization exemplifies a typical Matthew effect: "The good channels become better, and the poor channels become worse." To optimize data transmission efficiency, data bits are strategically allocated across these channels based on their reliability. The most reliable channels, the top K, are utilized for transmitting 'informative bits,' which carry the actual data. Conversely, the less reliable channels are designated for transmitting 'frozen bits'—these are redundant bits with predetermined fixed values that do not carry unique information but are crucial in enhancing the likelihood of successful decoding of the informative bits. This allocation strategy maximizes the efficiency and reliability of data transmission by exploiting the inherent differences in channel capacities. For more detailed insights into the encoding and decoding processes utilized in this framework, please refer to [147].

Encoder. Let us consider a formal scenario where the code length $N = 2^n$ and K informative bits require transmission. The binary source block $\mathbf{u} = (u_1, u_2, \ldots, u_N)$ comprises K information bits and $N-K$ frozen bits. The codewords $\mathbf{x} = \{x_1, x_2, \ldots, x_N\}$

have a code rate $R = K/N$. The codewords $\mathbf{x}$ can be computed as follows:

$$\mathbf{x} = \mathbf{u}\mathbf{G}_N = \mathbf{u}\mathbf{B}_N\mathbf{F}_2^{\otimes n} \text{ and } \mathbf{F}_2 = \begin{bmatrix} 1 & 0 \\ 1 & 1 \end{bmatrix} \tag{4.4}$$

Here, $\mathbf{G}_N$ represents the generation matrix, $\mathbf{B}_N$ symbolizes the bit-reversal permutation matrix, and $\mathbf{F}_2^{\otimes n}$ is the n^{th} Kronecker power of $\mathbf{F}_2$. Further details regarding this can be found in Arikan's work [146]. Considering that $K = 152$, possible code rates can be represented as 152/256, 152/512, 152/1024, 152/2046, ... or in approximate terms, 0.98, 0.30, 0.15, 0.07, ..., extending the payload length to 256, 512, 1024, ... respectively. MeAnt dynamically adjusts R according to the SNR of the scenario to achieve higher goodput.

Decoder. The decoding of Polar Codes at the receiver end involves calculating the log-likelihood ratios (LLRs) for each received bit. These LLRs quantify the probability that each bit is a 0 or a 1 based on the received channel symbols. The LLR for a bit is a measure of confidence in the bit's value derived from the statistical likelihood of the received symbols given the noise characteristics of the channel. The process of computing these LLRs is recursive, leveraging both the outputs from the communication channel and bits that have been previously decoded. This recursive calculation is essential for the decoding strategy because it utilizes the structured nature of Polar Codes, where each set of bits influences the decoding of subsequent bits. Polar Codes employ the belief propagation (BP) algorithm for decoding, as detailed in [148].

The BP algorithm is an iterative message-passing technique that operates on a binary tree structure, which represents the relationships and dependencies among the bits encoded by Polar Codes. Each node in this binary tree corresponds to a particular combination or transformation of the encoded bits. During decoding, each node updates the belief about its bit based on the LLRs computed for its children nodes. These updated beliefs are then passed as messages up to the parent nodes in the tree. This iterative process continues until it converges, typically when the messages stabilize and no further significant changes in LLRs are observed, or until

a predefined number of iterations are reached. The final beliefs at the nodes of the binary tree then determine the most likely value for each bit, effectively decoding the received message. A more comprehensive exploration of this decoding scheme, including specific algorithms and theoretical underpinnings, can be found in [147].

Interleaving Technique for Error Mitigation: Interleaving is a robust technique employed to mitigate transmission errors by breaking a packet into independent symbols and rearranging them before transmission. This process effectively disperses potential errors across the entire message rather than allowing them to concentrate in specific locations, thereby enhancing the overall reliability of the communication system. In our implementation within the MeAnt system, the symbols encoded by Polar Codes are transmitted through distinct packets using an interleaving matrix. The interleaving matrix reorders the encoded symbols in a systematic manner before they are sent over the communication channel. This rearrangement ensures that any errors introduced during transmission are spread out across the entire data sequence, minimizing the likelihood of concentrated error bursts that could severely impact the message integrity. Upon reception, the symbols are de-interleaved using the inverse of the interleaving process, restoring them to their original order. This de-interleaving helps in distributing the errors, making them more manageable for the error correction mechanism, specifically the Polar Code decoding process. By dispersing errors, interleaving enhances the effectiveness of the Forward Error Correction (FEC) techniques, such as those utilizing Polar Codes, thereby improving the overall robustness of data transmission in cross-medium channels that are susceptible to interference and noise.

The implementation of interleaving within MeAnt not only ensures a higher level of data integrity but also complements the existing error correction strategies by providing an additional layer of error distribution. This synergy between interleaving and Polar Code-based FEC significantly contributes to the system's ability to maintain reliable communication in challenging environments.

4.4 Implementation of MeAnts

This section presents the hardware prototypes developed for the nodes and gateway within the MeAnt. Our objective was to create a proof-of-concept model using cost-effective, easily obtainable components. This approach was chosen to enable other researchers to replicate and adapt the platform for their specific experiments.

4.4.1 Material Choice for Optimal Radiation

This discussion aims to identify the most suitable PZMs for constructing a Piezo-MA and guarantee a larger power radiation efficiency while remaining economically affordable for a large-scale deployment. Numerous PZMs, including quartz, PZT, barium titanate, PVDF, lithium niobate, gallium orthophosphate, and aluminum nitride, are commercially available.

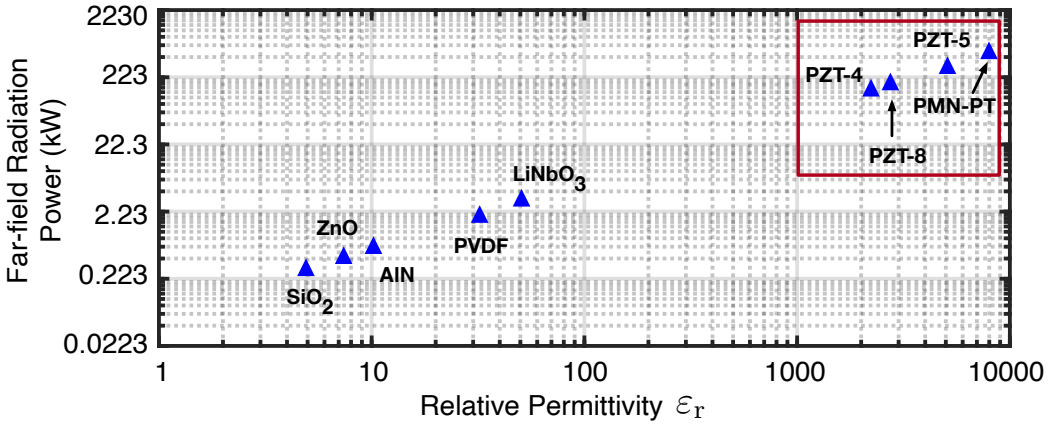

Fig. 4.10: Comparison of far-field radiation power across different piezo-materials when the largest electric field $E_{\max}$ is applied.

When an alternating electric field E with an angular frequency ω is applied to an MA, the antenna emits EM waves of the same frequency. The total power radiated can be computed by integrating the Poynting vector over a sphere in the far field. This integration yields the following equation:

$$P_{RX}^{\mathrm{MA}} = \frac{\sigma_q^2 V^2 \omega^4}{6\pi\varepsilon_0 c^3} \approx \frac{E^2 \omega^4 \varepsilon_0}{6\pi c^3} \varepsilon_r^2 \tag{4.5}$$

where σ_q represents the charge density within the material volume V, approximately given by $\sigma_q \approx \frac{E \cdot \varepsilon_r \varepsilon_0}{V}$, where ε_0 denotes the vacuum permittivity and ε_r signifies the relative permittivity of the material. c is the speed of light. The maximum allowable value of E is approximately 3 MV/m (denoted by $E_{\max}$), beyond which the electrical insulation of air would abruptly collapse, leading to rapid material short-circuiting known as air-breakdown.

To assess the effectiveness of different materials, we computed the far-field radiation power of cylindrical MAs (with a volume of $1 \times \pi \times 4^2$ cm^3) across various materials using Eq.4.5. The resulting data are illustrated in Fig.4.10. Unfortunately, materials such as quartz, AlN, $LiTaO_3$, and $LiNbO_3$ displaying low or moderate relative permittivity yield inadequate radiation power, thereby limiting the communication range. Conversely, materials with high relative permittivity, namely PZT-4, PZT-8, PZT-5, and PMN-PT ($\varepsilon_r > 1000$), effectively address this issue.

PMN-PT, boasting an impressive permittivity of up to 7400 F/m, emerges as the most suitable material. However, its high cost, approximately 4000 USD/kg, limits its widespread use. On the other hand, PZT-5 offers performance akin to PMN-PT at a significantly lower cost of approximately 25 USD/kg. In conclusion, we identify PZT-5 as the optimal material for MA fabrication due to its commendable blend of performance and cost-effectiveness.

4.4.2 Mechanical Structure

Fig. 4.11(a) presents a deconstructed view of the MeAnt node, ingeniously crafted to form a compact mechanical structure. This design not only ensures robust protection of the internal circuitry from water and external pressures but also adheres to a cylindrical shape with dimensions of approximately 16 cm in height and 13 cm in diameter. The node comprises a waterproof shell, which encases an internal compartment housing the motherboard. Strategically positioned on the cylinder's ceiling, the Piezo-MA

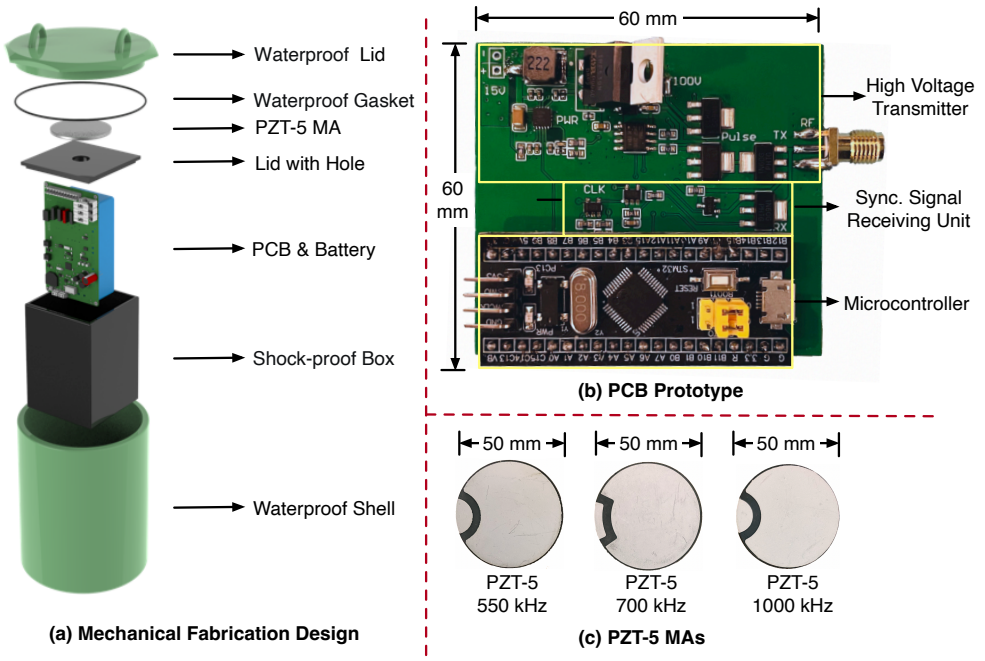

Fig. 4.11: Mechanical Fabrication of MeAnt

facilitates efficient conduction of vibrations to and from the surrounding medium, a critical feature for the effective implementation of the anti-collision protocol. The entire mechanical structure was meticulously designed using SolidWorks [94] and realized through advanced 3D printing techniques. For our evaluation, a total of 10 MeAnt nodes were fabricated, each at an approximate cost of 30 USD per node. This cost-effective manufacturing process allows for scalable production while maintaining the integrity and functionality of each unit.

4.4.3 Circuit Design and Functionality

The central component of a MeAnt node is the motherboard, represented by a 6 × 6 cm^2 two-layer PCB, as depicted in Fig. 4.11(b). This board serves three primary functions: handling the uplink, managing the MAC protocol, and controlling the logic of the system. For an overall view of the system's circuitry, refer to Fig. 4.12.

(1) Ultra-High-Voltage Driver: Traditionally, PZT transducers require high driving voltages, typically in the hundreds of volts, which often necessitate the use of bulky

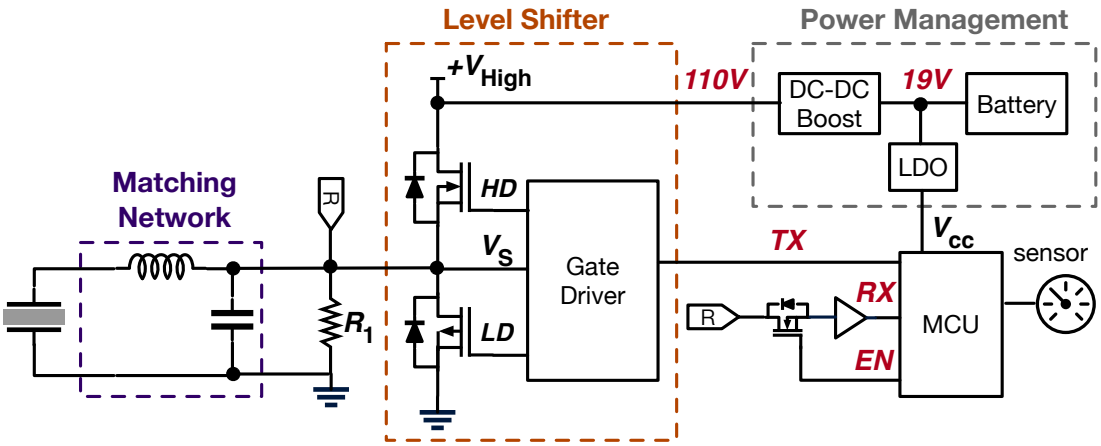

Fig. 4.12: Hardware Schematic

and expensive voltage amplifiers like the Ciprian HVA-400 [149]. Such devices have been utilized in previous studies to generate continuous acoustic waves within gateways [140,150]. However, this approach is not economically feasible for our nodes due to its high cost and size. To overcome this, we have developed a specialized driver circuit that can amplify a weak MCU output voltage by a factor of 22×.

As illustrated in Fig.4.12, our design incorporates a DC-DC booster (TPS40210DCR [151]) to raise the input voltage from 19 V to 110 V. We then designed a UHV driver circuit, which includes a dual NMOS (IRS21867STRPBF [152]) and a dual-MOSFET gate driver (NCE0102 [153]). This setup achieves rise and fall times of 170 ns, accommodating a maximum frequency of 5 MHz. The driver circuit functions as an amplifier, taking a 5 V input signal and boosting it to a 110 V output, while connected to the 110 V DC output from the booster, effectively amplifying the 5 V MCU signal to approximately 110 V. The amplified signal is then directed to drive the PZT through a carefully tuned matching network.

Concerning the total power consumption $P = VI$ by the Piezo-MA due to the high voltage, our practical measurements indicate that the Piezo-MA draws less than 1 mA of current, largely because of its high impedance. Thus, the power dissipated by the Piezo-MA remains around 100 mW, making it a low-power component. Importantly, this configuration does not significantly affect the antenna's radiation efficiency. The

primary factor influencing the deformation and radiation characteristics of the Piezo-MA is the applied voltage, rather than the power dissipation.

(2) Frontend: The frontend of our system integrates the Piezo-MA with a matching network, serving dual functions of EM radiation and vibration sensing. Utilizing the pulse width modulation (PWM) technique described in [154], we simulate the CSS-based carrier signal. PWM is particularly adept at generating digital square waves with variable widths, making it ideal for our application. To emulate an up-chirp signal, we generate a sequence of 10 square waves with frequencies incrementally ranging from f_1 to f_2 in steps of $(f_2 - f_1)/10$. Fig. 4.13 illustrates the chirp signal produced by the PWM controlled by the MCU.

In addition to its role in signal generation, the Piezo-MA also acts as an acoustic frontend, detecting RTS packets from other nodes by sensing vibrations induced in the Piezo-MA. To mitigate self-interference, logic gates are employed to alternately activate the RTS window and the channel sense window, thus enabling concurrent operations without overlap. Another approach involves dispatching the RTS prior to conducting channel sensing, a strategy that addresses potential conflicts in simultaneous sensing as outlined in Sec. 4.3.2.

Detection of an RTS packet is triggered when the cumulative vibration—or, in some implementations, the voltage change across the Piezo-MA's electrodes—exceeds a predefined threshold. This change is indicative of other nodes' RTS causing vibrations that affect the Piezo-MA's own transmitting RTS, evident through altered voltage amplitudes. Upon signal reception, an initial amplification and filtering stage is applied to eliminate any noise originating from the frontend itself, ensuring the detection of RTS is reliable and accurate. This methodology not only ensures effective RTS detection but also optimally manages concurrent operations within the system.

(3) Power Management: The node is powered by a 19 V lithium-ion battery. Voltage regulation is achieved using a low-dropout (LDO) regulator, specifically the

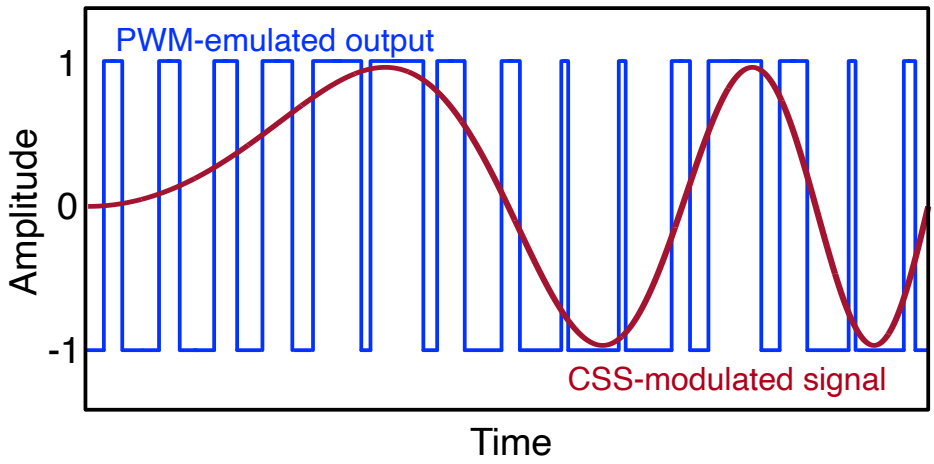

Fig. 4.13: PWM-emulated chirp signal. By varying the frequency and duty cycle of the PWM, we can generate a CSS-modulated carrier.

TI AMS1117 [155], which efficiently converts the 19 V input into a stable 3.3 V output to power the MCU and sensors. Additionally, the DC-DC booster previously mentioned is utilized to supply the necessary voltage to the Piezo-MA.

(4) Controller: For the system's controller, we have opted for an MCU, specifically the STM32F103 [99], which features a 72 MHz frequency CPU. This MCU supports a low-power mode, adding a layer of versatility in power management that is crucial for energy conservation in mobile applications. In active mode, the MCU's power consumption is approximately 4.4 mW, which dramatically decreases to 0.9 μW in deep sleep mode. This efficiency is pivotal in extending battery life without compromising functionality. The MCU also utilizes its internal PWM module to modulate the baseband bit effectively, crucial for precise signal manipulation. For data acquisition, particularly analog vibration data from other nodes, the MCU's internal ADC pin is employed. Additionally, it utilizes the SPI protocol for seamless communication with various sensors, facilitating streamlined data exchange and integration within the system.

4.4.4 Regulatory Compliance

The operational frequency band for our MeAnt system is situated within the MF band, which spans from 300 kHz to 3 MHz. This frequency range is regulated stringently due

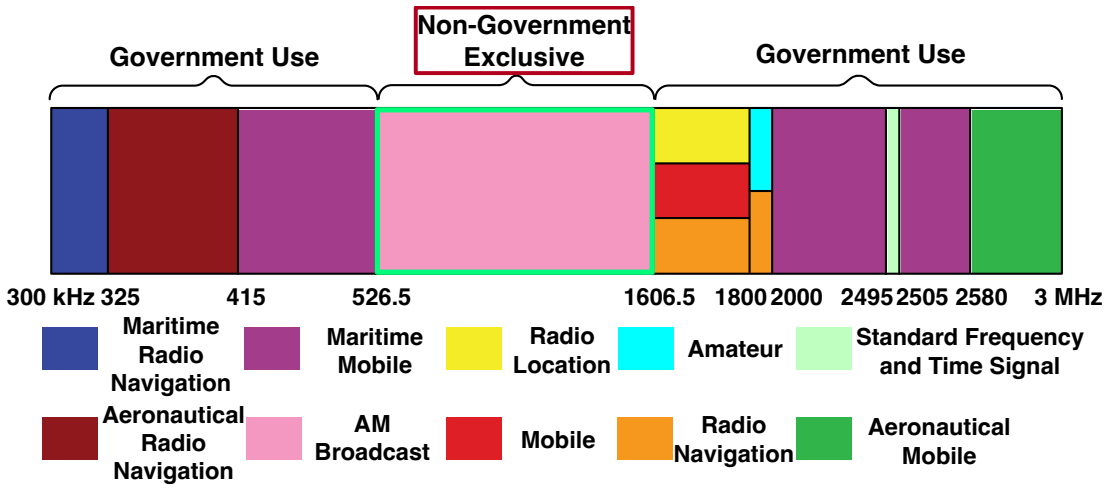

Fig. 4.14: Medium Frequency Band Allocation According to FCC Regulations.

to its widespread use in public broadcasting, maritime communications, and various government operations. Fig. 4.14 depicts the allocation principle for this band.

Fortunately, within this range, the AM broadcasting band (526.5 - 1606.5 kHz) is available for use by amateur radio operators under FCC regulation OET Bulletin No. 63 [156], which allows operation without a license under certain conditions. Specifically, the regulation mandates that the transmission power must not exceed 100 mW, and the coverage radius should be limited to less than 0.5 miles. This provision does not require a public announcement and even permits the broadcast of business commercials [157].

Moreover, the emission frequency of MeAnt's acoustic signals begins at 530 kHz, which effectively avoids interference with marine and soil life. Research indicates that most marine and soil organisms perceive frequencies only up to 200 kHz [158], ensuring that our system's operation does not adversely affect these environments.

4.5 Evaluation

In this section, we introduce the evaluation methodology and the results of MeAnt.

4.5.1 Methodology

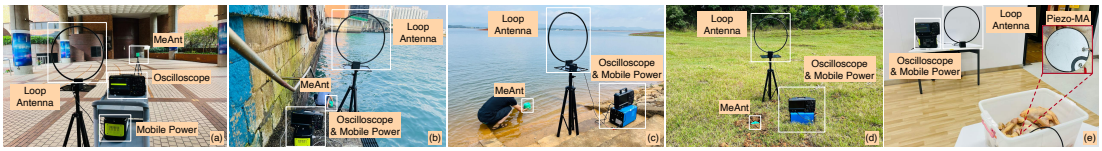

Fig. 4.15: Experimental setups. (a) shows air-to-air communication. (b) shows the seawater-to-air communication. (c) shows the freshwater-to-air communication. (d) shows soil-to-air communications. (e) shows tissue-to-air communication. In (b), (c), and (d), since the MeAnt will become invisible after we have completely placed it in the mediums, we choose to demonstrate the experimental scenario where the in-medium distance is 0.

We utilize the A.H. Systems SAS-565L Passive Loop Antenna [139] as the gateway for receiving EM radiation emitted by the MeAnt nodes. This antenna is characterized by a frequency range of 20 Hz to 1 MHz, making it well-suited for our application. The loop antenna is connected to a low-noise bandpass amplifier, which is specifically configured to remove extraneous noise while retaining signals within the desired frequency band. The signal collection is performed using a RIGOL MSO5204 Digital Oscilloscope [159], set to a sample rate of 200 MS/s. This high sampling rate ensures accurate capture of the fast-changing signals emitted by the MeAnt nodes. For signal decoding and further analysis, we have developed a MATLAB-based program. This custom software efficiently processes the signals post-collection, applying sophisticated decoding algorithms to interpret the data transmitted by the nodes.

Experiment Settings: The experimental setups employed to evaluate the cross-medium communication capabilities of MeAnt nodes are illustrated in Fig. 4.15. Our experiments are designed to encompass a variety of mediums to test the versatility and robustness of the communication system. Specifically, MeAnt nodes are embedded 10 cm deep in animal tissues, such as pork and chicken, submerged 1 m deep in both freshwater and seawater and buried 50 cm within solid materials, including concrete and soil. Unless otherwise specified, the gateway is consistently positioned in the air, approximately 2 m from the boundary of the medium being tested. For concrete-air communication experiments, the transmitter and receiver are directly aligned on opposite sides of a 50-cm-thick concrete wall. Additionally, to establish a baseline for

performance comparison, we assess the effectiveness of MeAnt nodes in an air-to-air setting. Overall, this comprehensive series of tests investigates the communication efficacy across multiple scenarios, including air-to-air, water-to-air, tissue-to-air, and concrete-to-air, to determine the system's adaptability and effectiveness in various environmental conditions.

4.5.2 Physical-Layer Performance

First, we evaluate the physical layer performance of MeAnt in terms of the experimental settings.

• **SNR vs. Bitrate**. The bitrate in our communication system represents the number of bits conveyed each second and determines the width of each transmitted symbol (i.e., its duration). Theoretically, with a symbol width of 1 ms, the maximum attainable bitrate would be 1 kbps. In our experiments, different symbols correspond to different start frequencies for frequency sweeping. An increased bitrate accelerates the sweep rate, which can amplify the tailing phenomena in the signal, making each symbol more challenging to decode and leading to a diminished SNR at the gateway. These observations are detailed in Fig. 4.16. The figure highlights several critical insights: 1) As expected, there is a noticeable decrease in SNR with an increase in bitrate, attributable to the heightened decoding challenges. Across various mediums, the SNR reaches a decoding threshold at a bitrate of 10 kbps, likely due to the restricted bandwidth of the Piezo-MA. 2) The SNR varies across different mediums at a consistent bitrate, reflecting their distinct electromagnetic attenuation ratios. These ratios correlate with each medium's electrical conductivity, dielectric properties, and density. Mediums with higher attenuation ratios typically exhibit higher conductivity and density, as well as increased dielectric losses. 3) The performances in tissue mediums (chicken and pork) are notably similar, primarily because the MeAnt nodes are positioned only 10 cm deep, a depth that is insufficient to demonstrate inherent diversities between these mediums. In summary, our experimental results reaffirm the

viability of cross-medium communication using the Piezo-MA across a broad range of applications despite the challenges posed by higher bitrates.

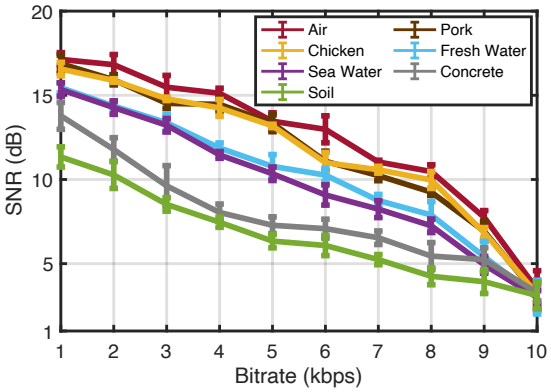

Fig. 4.16: SNR vs Bitrate

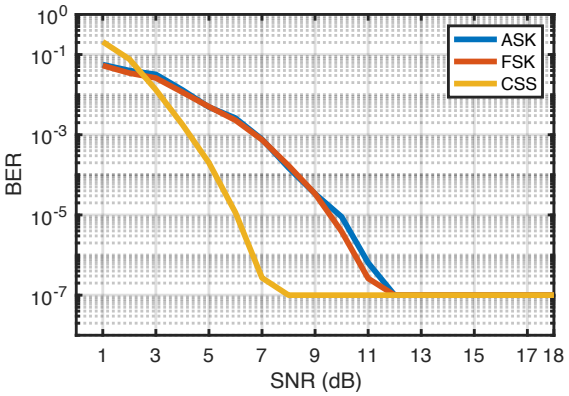

Fig. 4.17: BER vs SNR

• **BER vs. SNR**. We investigate the efficacy of four modulation techniques—Amplitude Shift Keying (ASK), Frequency Shift Keying (FSK), and CSS—in a single MeAnt node. The efficiency of these schemes is primarily gauged through the bit error rate (BER), which represents the percentage of incorrectly decoded bits. To assess the relationship between BER and the SNR, we progressively distance the gateway from the MeAnt node, effectively reducing the SNR. These observations are detailed in Fig. 4.17. At SNR values below 2.5 dB, the BERs for the three modulation schemes appear indistinguishable. However, as the SNR increases, the BER of the two CSS-based schemes decreases significantly steeper than that observed for ASK and FSK. Notably, CSS-based modulation achieves a BER of 10^{-7} at an SNR of approximately 7.5 dB, which is a 5 dB improvement over the other techniques. This superior performance is attributed to the enhanced resilience of CSS to noise, an advantage that is particularly beneficial in cross-medium communication scenarios.

• **Maximum Depth**. We explore the depth and range capabilities of the MeAnt system across various mediums, including freshwater, seawater, soil, and air. Superficial tissues are not considered as they do not show any signal changes throughout the medium. The maximum effective communication depth or range for each medium is defined by the point at which the SNR of the received signal declines to 2.5 dB.

To determine this, the MeAnt node is progressively relocated from the boundary of each medium using a submerged pole for aquatic environments and a soil auger for terrestrial settings. These findings are graphically illustrated in Fig. 4.18. In aerial conditions, the maximum communication reach of the MeAnt system is recorded at 12 meters, roughly one-tenth of the range achievable by technologies such as Zigbee in airborne environments. This limitation is largely due to the Piezo-MA's reduced efficiency in converting incoming energy into electromagnetic radiation compared to an EA operating within the ISM band. In terms of cross-medium communication, the MeAnt system demonstrates notable capabilities with a reach of 10 meters in both freshwater and seawater and 7 meters in soil. The soil medium presents the greatest challenge, exhibiting the highest EM wave attenuation due to its significant conductivity, porous structure, and mineral-water composition. Conversely, with their lower conductivity and salinity, freshwater and seawater manifest similar and comparatively lower levels of attenuation. It is important to note that the water in both saltwater and freshwater real-world experiments was not calm; it exhibited significant waves and ripples, with the water remaining entirely fluid. While this dynamic environment exacerbates the complex multipath effects, the use of polar codes enables our packets to still be successfully decoded despite these challenges. These performance metrics are well-suited to meet the predominant requirements of the IoT domain, where conventional communication protocols like Zigbee and 5G struggle to maintain functionality beyond a depth of approximately 1 meter in aquatic environments.

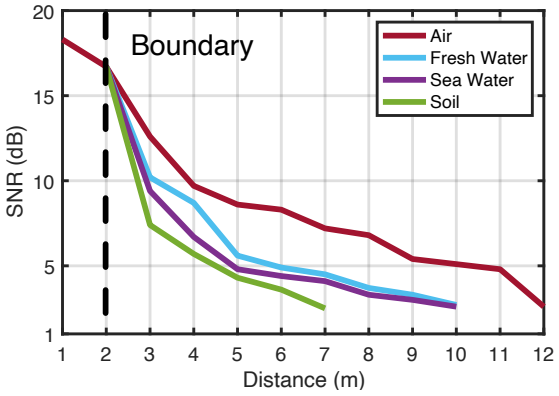

Fig. 4.18: Maximum Depth

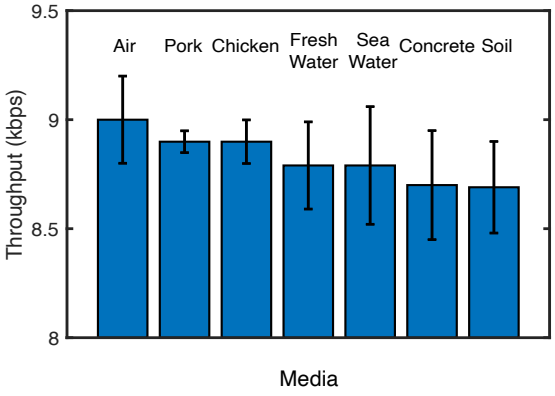

Fig. 4.19: Throughput

• **Throughput vs. Material**. We test the throughput of the MeAnt in air and five cross-medium scenarios. The result is plotted in Fig. 4.19. Throughput is defined as the number of bits correctly decoded by the reader per second. The following observations were made from our experiments: (1) The air-water throughput is 8.9 kbps, while that of the SOTA System (TARF) [48] is merely 400 bps. Our system's throughput is 22 times greater than that of SOTA, showcasing its significant performance advantage in this context. (2) The throughput across all mediums scenarios is remarkably consistent, with an average of 8.824 kbps. This uniformity in throughput can be attributed to the closely matched attenuation rates for MF waves across different mediums.

4.5.3 Link-Layer Performance

Next, we assessed the efficacy of various anti-collision techniques in a setting where five nodes competed for channel access, with packet sizes fixed at 256 bits and both the channel sensing window and the RTS in CSMA/CA defined at 52 bits. We conducted tests involving the transmission of 1,000 packets to determine the packet success rate (PSR) at the gateway. The performance metrics, as depicted in Fig. 4.20, show PSRs for various schemes: ALOHA at 0.3, standard CSMA/CA at 0.65, CSMA/CA with RTS at 0.7, and synchronized CSMA/CA with RTS at 0.99. The limited performance of the ALOHA scheme is due to its absence of carrier sensing, which leads to higher collision rates. In contrast, CSMA/CA with RTS outperforms pure CSMA/CA as it limits the duration of collisions to the RTS length, which can be managed with polar codes. The synchronized CSMA/CA+RTS approach demonstrates exemplary PSR, indicative of its superior capability in collision mitigation, albeit potential synchronization misalignments or hardware clock drifts could still lead to infrequent packet failures.

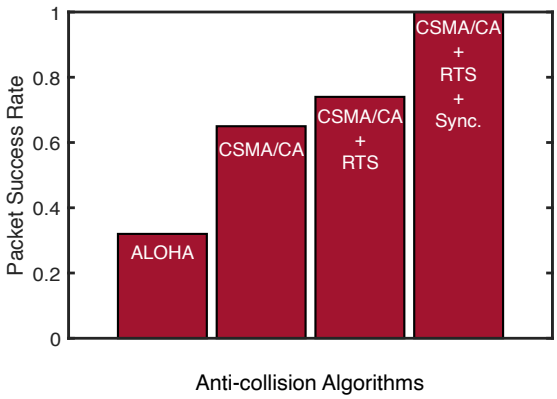

Fig. 4.20: Packet Success Rate

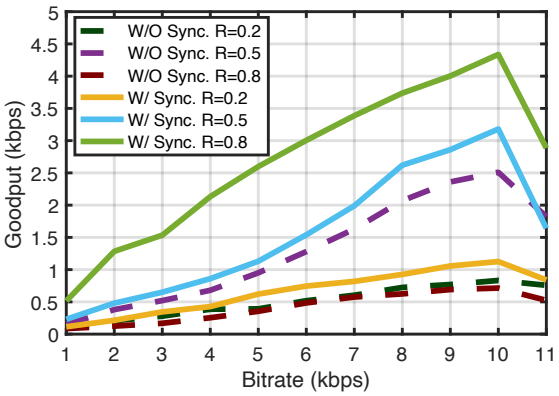

Fig. 4.21: Goodput

4.5.4 Transport-Layer Performance

We investigate MeAnt's goodput, analyzing various code rates and their impact under synchronized and non-synchronized CSMA/CA + RTS conditions. The relationship between bitrate and goodput is explored in Fig. 4.21. It is observed that as the bitrate increases, goodput also escalates. The highest goodput, recorded at 4.3 kbps, is achieved with a coding rate of 0.8 under synchronized conditions. However, increasing the bitrate beyond 10 kbps results in a decline in goodput due to a significant increase in the BER. In non-synchronized settings, moderate coding rates achieve the best goodput. High coding rates in these conditions lead to reduced goodput, primarily due to increased collision rates, highlighting the vulnerability of non-synchronized environments to conflicts. This suggests the importance of balancing error correction capabilities with coding efficiency. In synchronized settings, a higher coding rate is recommended to maximize goodput, benefiting from the lower collision rate.

4.5.5 Power Consumption

Then, we evaluate the power consumption by MeAnt nodes.

• **Maximal Range vs. Voltage**. We adjust the DC-DC booster to produce 0 V to 110 V voltages. The node was positioned at a depth of 1 m within the chosen medium. In every scenario, we determined the maximal communication distance by

progressively distancing the gateway from the node or the medium boundary until the SNR of the received signal diminished to 2.5 dB. We conducted these tests in various mediums. The data are captured in Fig. 4.22. Predictably, the maximal range is enhanced as the applied voltage to the Piezo-MA rises. Without using the booster and our UHV driver circuit, the default 5 V signal output from the MCU barely triggers the Piezo-MA. Mediums with lower EM attenuation also tend to support more extended ranges, which aligns with our previous observations.

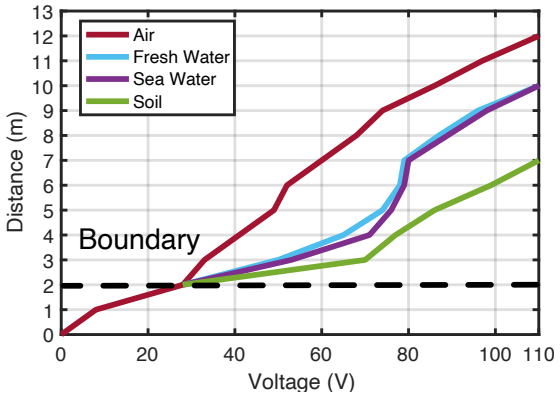

Fig. 4.22: Range vs Voltage

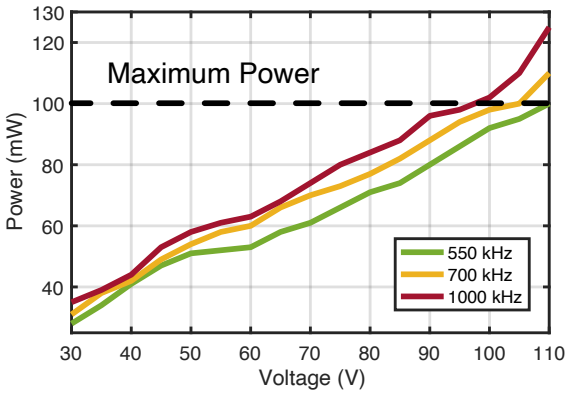

Fig. 4.23: Power Consumption

• **Power Consumption.** Energy efficiency remains paramount for sensor networks. To quantify power use, we employ the Keysight Technologies B2900A Source Meter [160] to gauge the supply voltage and current drawn by the MeAnt node. Fig. 4.23 shows power as the voltage spans from 30 V to 110 V. We witness a near-linear surge in total power consumption corresponding to the voltage increment, primarily attributed to the substantial energy draw of the Piezo-MA. Nonetheless, the cumulative power hovers around 100 mW at an input of 110 V to the Piezo-MA operating at 550 kHz. We further assessed two alternative Piezo-MA configurations operating at 700 and 1000 kHz, respectively. The outcomes, albeit analogous, exhibited minor variances. For these 2 Piezo-MAs, the voltage should be controlled to keep the overall power below the FCC regulations [156]. Factoring in a battery rated at 2 A with a 1000 mAh capacity, a MeAnt node can continuously broadcast signals for an estimated 1100 hours or 45.83 days. By leveraging more advanced miniaturized chip tape-out technology, we can further reduce the power consumption of the driving circuit, allowing

it to theoretically operate for up to 300 days.

4.5.6 Antenna Directionality

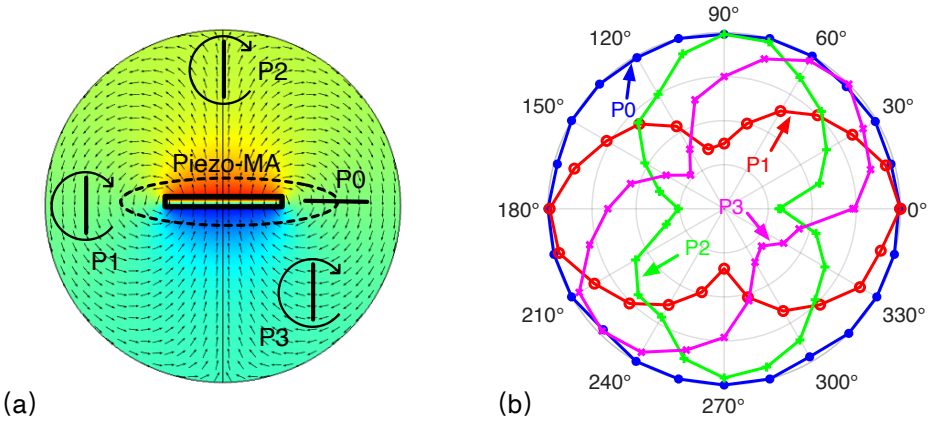

Fig. 4.24: Directionality of Piezo-MA.

Finally, we assess the directionality of the Piezo-MA on MeAnt nodes within an RF anechoic chamber. The setup is illustrated in Fig. 4.24(a), where the Piezo-MA is centrally placed, and the loop antenna is positioned at location P_0. Here, the surface of the Piezo-MA and the entire loop are aligned on the same plane. We then rotate the loop in a circular motion around the Piezo-MA, which serves as the pivot. Radiation measurements on the H-plane are detailed in Fig. 4.24(b), showing that the maximum quantity of intersecting lines through the loop occurs at P_0, yielding peak receiving efficiency. This observation aligns with our simulation EM field model, which predicts maximal signal intensity across all angles without significant variation.

To assess radiation within the E-plane, the loop antenna is subsequently fixed at positions P_1, P_2, and P_3. At each position, the loop is rotated around its primary axis. Initially, a reduction in the number of intersecting lines through the loop is observed during this rotational movement. However, this is followed by a dual-peak surge, forming a distinctive figure-eight pattern as depicted in Fig. 4.24(b). The pronounced directionality of the Piezo-MA along the E-plane suggests that adjusting the loop antenna's placement angle is crucial. Properly positioning the loop antenna in

Table 4.2: Comparison with current direct cross-medium communication methods

Type	Approach	Direction	Data Rate	Distance	[1] Mediums	Volume	Misalignment	Cost	Env.-Friendly
Acoustic-RF	Vibration Sensing [48]	Uplink	400 bps	3.9 m	Water	Large	×	High	×
Laser	Water Dynamics Measure [44, 114]	Bidirection	5.04 Mbps	6.1 m [2]	Water	Compact	×	High	×
	Circularly Polarized Light [115]	Bidirection	200 kbps	2.5m	Water	Compact	×	Medium	×
Magnetic	Magnetic Induction [161, 162]	Bidirection	∼10 bps	10 m	Water & Soil	Large	×	High	×
	Magnetic Backscatter [9]	Uplink	8 kbps	0.03 m	Tissue	Compact	×	High	×
RF	Direct MF (MeAnt)	Uplink	10 kbps	10 m	All	Compact	√	Low	√ [3]

[1] Distance here refers specifically to the total distance in water-air communication for a fair comparison.

[2] The maximum communication range is limited by their experimental setup.

[3] The vibration leakage will not be perceived by marine organisms since they can only hear acoustic signals up to 200 kHz [163].

advance can ensure that the SNR is optimized for effective cross-medium communication.

4.6 Related Work

Our work is related to prior works in the following fields:

(1) Direct Cross-Medium Communication: The quest to establish direct cross-mediums networks has attracted considerable interest within the wireless community. We list the detailed comparison with current direct cross-medium communication in Table 4.2. Existing solutions are broadly categorized as follows:

- Magnetic Induction: Utilizes the penetration capabilities of magnetic fields for communication across various mediums, including water [161,164] and soil [162]. However, this method requires perfectly aligned and large transmitter coils, which pose challenges for real-world applications due to their size and alignment requirements.

- Laser: These systems employ refracted lasers to establish air-water links [44,114, 115]. While innovative, they are highly sensitive to water surface fluctuations and suffer from limited range due to significant attenuation. State-of-the-art works [114] have achieved maximum distances of only 3.1 m, whereas MeAnt achieves depths three times greater.

- Acoustic-RF: The TARF system [48] uses radar to detect underwater acoustic vibrations, achieving a communication range of 3.9 m and a throughput of 400 bps. In stark contrast, our proposed MeAnt system utilizes low-frequency electromagnetic (EM) waves, successfully achieving a range of 10 m across water boundaries with a throughput of 10 kbps. This marks a two-fold increase in range and a twenty-five-fold increase in throughput compared to TARF.

Additionally, MeAnt demonstrates remarkable resilience against environmental factors such as sea surface wind and waves, further underscoring its advantages over traditional methods in challenging communication scenarios.

(2) Mechanical Antenna (MA): The MA represents a significant area of interest in the field of low-frequency communications [165, 166], noted for its compact size and high efficiency. Mechanical Antennas can be categorized into three primary types based on their operational mechanisms: electret-, magnet-, and piezo-MAs [121].

- Electret-based MA: This type of MA operates on the radiation emitted through the motion of polarized electret materials [167–170].
- Magnet-based MA: It involves the rotation of a magnet to generate magnetic field radiation [171–174].
- Piezo-MA: Radiation in Piezo-MAs is achieved through vibrations in piezoelectric materials [122, 124, 125] or a combination of magnetic and piezoelectric materials [175, 176].

Our research focuses on the Piezo-MA, which stands out due to its size, simplicity, and effective radiation intensity. While existing studies on MAs are primarily preliminary experiments that utilize bulky, power-intensive signal transmitters and amplifiers to establish physical layer connections, our work with MeAnt advances this concept by proposing a comprehensive, full-stack compact communication system. This system

is designed to explore the potential of MAs in facilitating cross-medium networks, significantly enhancing their applicability and effectiveness in diverse environmental conditions.

4.7 Conclusion

This paper introduces a novel cross-medium sensor networking technology, utilizing innovative Piezo-MAs to facilitate connectivity via MF EM waves. This advancement represents a significant step toward practical and scalable cross-medium communications, which are crucial for a broad range of applications. The utilization of Piezo-MAs enables efficient transmission across different mediums, such as water, soil, and dense environments, making it a pivotal development for industries and fields, including ocean exploration, subsea IoT, subterranean sensing, and smart farming. The technology not only enhances current communication capabilities but also opens new possibilities for environmental monitoring and resource management, underscoring its potential impact on global industrial and ecological practices.

Chapter 5

Conclusion, Lessons Learned, Methodology, and Future Works

5.1 Conclusion

The advancements presented in these two works address significant challenges in the realm of omnimedium communication, providing innovative solutions to both intra-medium and inter-medium communication barriers. These contributions are instrumental in advancing the vision of seamless data transmission across diverse physical environments.

EcoCapsule: The first work focuses on enhancing SHM in concrete environments by introducing a novel solution, the EcoCapsule. Traditional SHM methods rely on intrusive, wired sensors that pose several limitations, including high costs, limited monitoring regions, and maintenance challenges due to their cabling requirements. The EcoCapsule, a battery-free piezoelectric backscatter sensor, offers a groundbreaking approach to intra-medium communication within concrete structures. By integrating these sensors directly into the concrete during construction, the need for cables and later maintenance is removed, helping to maintain the structure's integrity. The

system uses elastic waves to both power up and communicate with the EcoCapsules, which then transmit data using backscatter communication. This method tackles the challenges in solid materials, including the occurrence of multiple wave types and high external pressures. Innovative solutions, such as wave prisms, frequency shift keying, and anti-stress shells, are employed to overcome these challenges. The successful deployment of EcoCapsules in various concrete types and the long-term pilot study on an operational footbridge underscore the viability and effectiveness of this approach in real-world applications. This development not only enhances SHM but also sets a precedent for intra-medium communication within solid materials.

The EcoCapsule technology is a pioneering advancement in intra-medium communication within concrete structures. This technology can be extended to other solid mediums, such as soil and geological formations, which are crucial for applications in environmental monitoring and infrastructure maintenance. For instance, embedding EcoCapsules in the soil can provide real-time data on soil health, moisture levels, and subsurface movements, which are essential for agricultural optimization and early warning systems for landslides or other geological hazards. The adaptability of this technology to various solid mediums enhances its utility, making it a versatile tool for comprehensive structural health monitoring and environmental assessment.

MeAnt: The second work tackles the challenge of low-power inter-medium communication, particularly between air and water, which is crucial for the upcoming 6G wireless networks and the IoE. Traditional methods of air-to-water communication rely on relay devices prone to displacement and operational challenges. This paper introduces the MeAnt platform, which leverages Piezo-MAs for direct cross-medium communication. By employing mechanical motion to generate electromagnetic waves, MeAnt overcomes the size constraints of conventional electrical antennas, making it suitable for compact and versatile applications across various mediums, including water, soil, concrete, and biological tissues. The platform addresses key challenges such as interference mitigation, collision management, and data integrity through innova-

tive techniques like chirp spread spectrum modulation, CSMA/CA with synchronized RTS, and polar codes. These solutions ensure reliable communication across different mediums, demonstrating the potential of Piezo-MAs to revolutionize cross-medium communication. The experimental validation and theoretical frameworks provided in the study establish MeAnt as a robust solution for seamless data transmission in diverse environments.

Moreover, the MeAnt platform's potential extends to underwater and underground communication systems. In marine environments, this technology can enhance underwater communication networks, enabling better data collection from oceanographic sensors and improving the coordination of autonomous underwater vehicles (AUVs) for scientific research and resource exploration. In underground environments, MeAnt can support communication in mining operations, enhancing safety by providing real-time data on environmental conditions and structural stability. The ability of Piezo-MAs to penetrate various mediums with minimal power requirements also opens up possibilities for their use in disaster response scenarios, where establishing communication in challenging environments is critical for search and rescue operations.

Together, these works contribute significantly to the overarching goal of omnimedium communication. The EcoCapsule advances intra-medium communication within solid structures by providing a maintenance-free, embedded sensing solution, while the MeAnt platform addresses the challenges of inter-medium communication, enabling seamless data transfer across different physical environments. By tackling both intra-medium and inter-medium communication barriers, these innovations pave the way for a future where data can be transmitted reliably and efficiently, regardless of the medium, thus advancing the integration of the Internet of Everything and the capabilities of 6G networks. Furthermore, these technologies' modular and scalable nature allows for their deployment in a wide range of applications, from smart cities and industrial automation to environmental conservation and healthcare. For instance, in the realm of smart healthcare, these communication methods simplify the process

of reading data from sensors embedded within the body. Similarly, in underground exploration, they could allow seamless communication with robots operating beneath the surface from above ground.

In summary, the developments presented in these papers not only address current challenges in intra-medium and inter-medium communication but also provide a robust framework for the future expansion of omnimedium communication technologies. By extending these innovations to a variety of mediums and applications, we can achieve a more interconnected and intelligent world where data flows seamlessly across all physical environments, driving advancements in safety, efficiency, and overall quality of life.

5.2 Methodology

Through our exploration of novel omnimedium communication paradigms, we aim to develop a comprehensive methodology that not only advances research in omnimedium communication but also serves as a guiding framework for broader communication-based studies across various domains.

Target the Problem: The foundation of any impactful research begins with identifying the core problem that needs to be addressed. In the context of communication technologies, this involves pinpointing the limitations of existing methods, such as their inability to operate consistently across diverse mediums like air, water, and solid structures. Understanding the challenges posed by these constraints enables researchers to establish a clear objective for their work and frame the broader significance of solving the issue.

Find out Solution: Once the problem is defined, the next step is to devise innovative solutions that address the identified gaps. This requires a multidisciplinary approach, leveraging insights from physics, material science, and signal processing

to design mechanisms capable of supporting communication in diverse environments. Sometimes, the solution comes from accidental paper reading, or from some unintentional experiment findings. The proposed solutions should be rooted in robust theoretical principles, ensuring feasibility and scalability for practical applications.

Conduct Preliminary Test: Before fully implementing the solution, conducting preliminary tests is essential to validate the underlying concepts and identify potential areas for improvement. These tests should evaluate the system's performance under controlled conditions that simulate real-world environments, offering critical data to refine the design. Iterative testing ensures the solution is reliable and efficient, minimizing unforeseen challenges in later stages. Also, the tests will reveal further challenges that we will encounter for real-world deployment.

Address Challenges: As development progresses, addressing challenges becomes inevitable, particularly those arising from system integration, environmental variability, or unforeseen technical limitations. Tackling these issues requires adaptability, creative problem-solving, and collaboration among researchers. By systematically overcoming obstacles, the research can maintain its trajectory toward delivering a functional and innovative communication paradigm.

Integrate into Systems: The final stage involves integrating the developed solution into existing communication systems to assess its real-world applicability and performance. This integration should focus on seamless compatibility and user-centric functionality, ensuring that the technology enhances existing networks without disrupting them. Successful integration not only validates the research but also paves the way for widespread adoption and transformative advancements in communication technologies.

5.3 Lessons Learned

Through our exploration of omnimedium communications throughout my Ph.D., I have learned many lessons to ponder. These insights have greatly benefited not only the exploration of omnimedium communication but also research in other related fields.

5.3.1 Integration between Existing Technologies

Researchers engaged in systems research must excel at integrating existing technologies into their systems. This integration requires a flexible mindset and a solid understanding of the technologies involved and the specific challenges they aim to address. For instance, the best paper from ACM SIGCOMM 2019 tackled the issue of underwater backscattering. This concept can be adapted and transferred to different scenarios, such as the interior of a wall for structural health monitoring. However, successful integration is not merely about copying existing solutions; it requires careful adaptation and innovation to meet the unique demands of the new application context.

When integrating existing technologies, it is essential to recognize and address the unique challenges posed by the specific scenario. This approach ensures that the research not only borrows from established methods but also contributes novel solutions to the field. In the context of omnimedium communication, our work involved the innovative application of mechanical antenna techniques. While these techniques have been used in other domains, we applied them to cross-protocol channels and developed new methods to overcome challenges specific to our research. This includes managing interference, ensuring data integrity, and achieving efficient energy use, all tailored to the particular needs of cross-medium communication.

This process of integration and innovation highlights the importance of interdisci-

plinary knowledge and creative problem-solving. By understanding the principles and limitations of existing technologies, researchers can adapt them to new contexts, pushing the boundaries of what is possible. For example, in developing the EcoCapsule for intra-medium communication within the concrete, we adapted non-intrusive detection techniques to address the complexities of wave propagation in solid materials. Similarly, in the MeAnt platform, we applied mechanical antenna technology to achieve low-power, cross-medium communication, overcoming the size constraints of traditional antennas.

Ultimately, the ability to integrate and innovate with existing technologies drives significant research advancements. It allows for the creation of systems that are not only practical and efficient but also capable of addressing new and complex challenges. This approach ensures that our research stands out, providing robust and versatile solutions for omnimedium communication. By continually exploring and adapting technologies from various fields, we can develop comprehensive systems that meet the evolving needs of diverse applications, from structural health monitoring to next-generation wireless networks.

5.3.2 Interdisciplinarity is Important

Interdisciplinary research is crucial for omnimedium communication. Firstly, in terms of research motivation, the collaboration between the fields of computer science and civil engineering provided us with the motivation to develop an in-wall passive backscatter communication network. This innovation addresses a longstanding challenge in civil engineering: wirelessly accessing the internal structural health monitoring data without relying on batteries. Traditional methods have been intrusive and maintenance-heavy, often limited by the need for wired connections or frequent battery replacements. By integrating principles from computer science, we could conceptualize and develop the EcoCapsule, a battery-free solution that significantly en-

hances the feasibility and reliability of SHM in concrete environments. Similarly, our interdisciplinary approach involving computing and ocean exploration highlights the critical need for cross-medium communication. We recognize the inadequacy of existing relay node-based solutions in addressing the dynamic and often harsh conditions of marine environments, prompting us to explore direct air-to-water communication methods.

Moreover, interdisciplinarity is particularly important in terms of the technical aspects of research. Conventional RF signals face significant attenuation issues, necessitating more novel and diverse approaches to low-power communication and networking. By combining our expertise with materials science, we explore the use of piezoelectric materials, leading to the development of Piezo-MAs. This approach leverages the unique properties of piezoelectric materials to create electromagnetic antennas, a burgeoning area of interest in materials science. Mechanical antennas offer promising solutions to the challenges of cross-medium communication, enabling efficient data transmission across various mediums such as water, soil, concrete, and biological tissues. Additionally, the integration of computer science principles allowed us to enhance these systems with advanced protocols, coding, and decoding techniques, making the entire system more robust and practical.

The lessons learned from these interdisciplinary collaborations highlight the importance of integrating diverse fields to tackle complex problems. The synergy between civil engineering, materials science, and computer science facilitates the development of innovative solutions like the EcoCapsule and MeAnt platform. These solutions not only address specific intra-medium and inter-medium communication challenges but also contribute to the broader vision of omnimedium communication. By fostering interdisciplinary research, we can continue to push the boundaries of what is possible, creating technologies that are more adaptable, efficient, and capable of operating seamlessly across different physical environments. This holistic approach is essential for advancing the IoE and realizing the full potential of next-generation wireless

networks.

5.3.3 Read and Gain Inspiration

Good inspiration often comes from reading. Engaging with a broad spectrum of literature allows researchers to uncover a wealth of valuable ideas and insights that can significantly influence their work. For instance, Dr. Adib's numerous papers regarding acoustic backscatter have profoundly inspired my research, providing both motivational and technical guidance. His work has highlighted innovative approaches and methodologies that have been pivotal in shaping my understanding and direction in omnimedium communication.

Through extensive reading and comprehension of various research papers, we can identify critical elements such as the feasibility of an idea and the portability of a specific technology. This process of continuous learning and adaptation is crucial for developing robust and innovative solutions. By analyzing and synthesizing the knowledge from diverse sources, we can refine our own research questions, methodologies, and technological applications, ultimately enhancing the quality and impact of our works.

Reading not only broadens our knowledge base but also helps us stay abreast of the latest advancements and trends in the field. It allows us to learn from the successes and challenges faced by other researchers, providing a foundation upon which we can build and innovate. This practice fosters a culture of intellectual curiosity and continuous improvement, driving us to push the boundaries of what is possible in omnimedium communication.

Ultimately, the insights gained from reading and understanding the work of others can be directly applied to our own research. They help in devising more effective communication strategies, improving the reliability and efficiency of our systems, and ensuring that our solutions are both practical and scalable. By incorporating these

learnings into our work, we can contribute to advancing the field and developing technologies capable of seamless communication across various physical mediums.

5.3.4 Focus on Practical Needs

Innovative ideas often emerge from addressing real-world challenges rather than theoretical exploration alone. Engaging with industry professionals and researchers from various disciplines is crucial for understanding practical needs and identifying pressing problems that require novel solutions. By stepping out of the lab and actively exchanging ideas with industry experts and practitioners, researchers can gain valuable insights that significantly shape the direction and relevance of their work.

Collaboration with industry not only helps in understanding the immediate needs and constraints but also provides a practical perspective that can guide research toward more impactful applications. For example, our work on the EcoCapsule for structural health monitoring was greatly influenced by the needs expressed by civil engineers concerned with the safety and longevity of concrete structures. Through discussions with industry experts, we identified the critical need for a maintenance-free, embedded sensing solution that could provide continuous data on the internal state of concrete without relying on cumbersome and intrusive cabling systems.

Similarly, our focus on cross-medium communication in the MeAnt platform was driven by practical challenges faced in marine and underground environments. By interacting with professionals in ocean exploration and environmental monitoring, we recognized the limitations of existing relay-based communication systems and the necessity for direct, low-power communication methods that could operate reliably across different physical mediums. These practical insights led us to innovate with mechanical antennas and develop solutions that are not only theoretically sound but also practically viable.

Ultimately, the most impactful and innovative research often arises from a deep un-

derstanding of practical challenges and necessities in various fields. By maintaining an ongoing dialogue with industry and other disciplines, researchers can ensure that their work is both relevant and applicable, leading to solutions that effectively meet the demands of real-world applications. This approach not only enhances the quality and utility of the research but also fosters a collaborative environment where ideas can flourish and evolve, driving continuous innovation and progress in omnimedium communication.

5.4 Future Works

5.4.1 In-Concrete Imaging with EcoCapsules

With the successful embedding of EcoCapsules within concrete structures, we now have the potential to advance into the realm of in-concrete imaging. This technology aims to utilize the reflected signals from EcoCapsules to construct detailed internal images of concrete, enabling the detection of internal damage, such as cracks and voids. By harnessing the principles of signal attenuation, refraction, and reflection, along with the broadband response characteristics of PZTs, we can achieve comprehensive internal imaging of concrete structures.

The initial phase involves the deployment of frequency-sweeping techniques. By transmitting a broad spectrum of frequencies and analyzing the reflected signals, we can map the internal features of the concrete. The variations in signal properties, such as attenuation and reflection, can provide critical insights into structural integrity. The broadband response of PZTs facilitates the use of a wide transmitting and backscattering frequency range, thereby enhancing the resolution and detail of the resulting images.

To further refine the imaging process, we propose integrating neural network-based

super-resolution techniques. Neural networks, trained on extensive datasets of concrete structures and known damage patterns, can process the raw signal data to produce clearer and more detailed images. These networks can be specifically designed to recognize and highlight different types of structural anomalies, thus improving the accuracy and utility of the imaging system.

Several key areas of future research will be critical to advancing this technology:

- **Optimization of Frequency Sweeping Techniques:** Investigating the optimal frequency ranges for various types of concrete and structural conditions will be essential. Tailoring the frequency sweeps to specific material properties and environmental conditions will enhance the precision and resolution of the imaging process.

- **Development of Advanced Signal Processing Algorithms:** Future research will focus on creating sophisticated signal processing algorithms capable of accurately interpreting the data from EcoCapsules. This includes noise reduction, signal enhancement, and advanced pattern recognition techniques to improve image clarity and diagnostic accuracy.

- **Training of Neural Networks for Super-Resolution Imaging:** Developing and training neural networks with large, annotated datasets that include diverse examples of concrete damage and structural anomalies will be crucial. These networks will need to be trained to recognize subtle differences in signal patterns indicative of specific types of damage.

By addressing these research areas, we can develop a robust in-concrete imaging system that significantly enhances our ability to monitor and maintain the integrity of concrete structures. This advancement not only promises to improve the safety and longevity of infrastructure but also contributes to the broader field of omnimedium communication by demonstrating the practical application of embedded sensor tech-

nology and advanced signal processing techniques.

5.4.2 Piezo Eavesdropping

The concept of a mechanical antenna is inherent in all piezoelectric materials, enabling them to perform acoustic-electric conversion and consequently emit EM waves. This phenomenon, often considered a byproduct, can be harnessed for innovative applications such as piezo eavesdropping. By deploying sensitive receiving antennas along with advanced signal processing solutions, we can exploit this leakage to enable eavesdropping across multiple scenarios, including underwater communication interception and microphone leakage detection in the air.

Piezo eavesdropping leverages the unique properties of piezoelectric materials. These materials, when subjected to mechanical stress, generate electric charges that can be converted into EM waves. By strategically placing sensitive receiving antennas in proximity to piezoelectric sources, we can capture these leaked EM signals. Such attacks and eavesdropping compromise the security of existing piezoelectric devices and create new challenges for the privacy protection of piezoelectric devices.

Some key application scenarios and potential techniques are listed below:

- **Underwater Communication Eavesdropping:** In underwater environments, piezoelectric materials are commonly used in sonar systems and underwater communication devices. The EM waves leaked during acoustic-electric conversion can be intercepted using specially designed underwater antennas. These antennas, combined with sophisticated signal processing algorithms, can filter and enhance the intercepted signals, allowing us to eavesdrop on underwater communications. This technology could significantly impact naval surveillance, underwater research, and maritime security.

- **Microphone Leakage Eavesdropping in Air:** In the air, piezoelectric mi-

crophones are ubiquitous in various electronic devices, including smartphones, laptops, and surveillance equipment. These microphones convert sound waves into electrical signals, which inadvertently emit weak electromagnetic waves. By employing sensitive antennas and advanced signal processing techniques, we can intercept these leaked signals to eavesdrop on conversations and audio recordings. This method could be particularly useful in intelligence gathering, counter-surveillance, and security applications.

- **Signal Processing and Neural Networks for Enhancement:** Capturing EM leakage from piezoelectric materials is only the first step. The intercepted signals are often weak and distorted, necessitating advanced signal processing techniques to filter out noise and enhance the desired signals. Techniques such as wavelet analysis and adaptive filtering can be employed to improve signal quality. Additionally, integrating neural networks for sound enhancement and optimization can significantly improve the clarity and intelligibility of the intercepted audio. Neural networks, particularly deep learning models, can be trained on large datasets of audio signals to recognize and enhance specific sound patterns. These models can learn to filter out background noise, amplify weak signals, and reconstruct distorted audio, making the intercepted signals much clearer and more useful. By leveraging the power of neural networks, we can transform raw electromagnetic leakage into high-quality audio data suitable for various eavesdropping applications.

5.4.3 Battery-free nm-level Vibration Sensing with COTS RFIDs

Piezoelectric transducers are commonly used for acoustic-electric conversion in applications such as vibration monitoring. Traditional implementations, however, necessitate wired connections and analog-to-digital conversion equipment to measure

the voltage changes across the piezoelectric terminals. This wired design restricts its application in many fields due to the constraints of physical connections and maintenance challenges. To overcome these limitations, we have developed a novel wireless vibration monitoring system that leverages COTS RFID technology, offering a battery-free solution with nanometer-level precision.

Our approach involves connecting PZTs to widely used RFID tags, creating a hybrid system that integrates the high sensitivity of piezoelectric sensors with the convenience and flexibility of wireless RFID communication. This integration is achieved through a well-designed circuit that modulates the vibration-induced changes in the impedance of the piezoelectric ceramics into the standard RFID communication protocol. Specifically, we employ MOSFET at the RFID antenna and the PZT to modulate the vibration voltage into conventional uplink and downlink signaling. The modulated signals are then transmitted to a receiver, which decodes these signals to provide high-precision analog modulation. This method detects vibrations at the nanometer level without needing batteries or wired connections. RFID technology not only simplifies the deployment and maintenance of the vibration monitoring system but also enables it to be used in various challenging environments where traditional wired systems would be impractical.

One of the key technical innovations of this system lies in the impedance modulation technique. By designing a circuit that accurately modulates the changes in impedance caused by vibrations in RFID communication signals, we can achieve precise and reliable vibration monitoring. This method ensures that even minute vibrations are captured and transmitted effectively. The receiver has advanced decoding capabilities to interpret the modulated signals accurately. This enables the system to achieve nanometer-level vibration sensing, making it suitable for applications that require extremely precise monitoring. This battery-free, wireless vibration monitoring system has broad applications across various fields.

This wireless, battery-free vibration sensing technology will be deployed in a variety

of real-world applications. For the power grid, the system can be deployed to continuously monitor the vibrations of transformers, detecting early signs of mechanical faults or degradation that could lead to failures. For bridge health monitoring, the system can be stuck to the bridge structures to provide real-time data on vibrations caused by traffic, environmental factors, or structural changes, enabling timely maintenance and repairs. In industrial settings, the system can be attached to various types of machinery to monitor their operational vibrations, helping to identify wear and tear or emerging issues before they become critical. Additionally, in the aerospace and automotive industries, the system can monitor the vibrations of components and assemblies, ensuring their structural integrity and performance under various operating conditions.

Future research will focus on several key areas to further enhance the capabilities and applicability of this wireless vibration monitoring system. Miniaturization efforts will aim to develop even smaller and more compact system versions to facilitate integration into tight spaces and complex structures. Enhanced signal processing algorithms will be investigated to increase the accuracy and reliability of vibration detection, particularly in noisy environments. Methods to extend the effective range of the RFID-based system will be explored to ensure reliable communication over longer distances. Finally, efforts will be made to enhance the robustness and durability of the system to withstand harsh environmental conditions, including extreme temperatures, humidity, and mechanical stresses.

By addressing these research areas, we can continue to refine and expand the applications of this innovative vibration-sensing technology, making it an indispensable tool for monitoring and maintaining critical infrastructures and systems.

References

[1] Zenghui Liu, Hua Wu, Wei Ren, and Zuo-Guang Ye. Piezoelectric and ferroelectric materials: Fundamentals, recent progress, and applications. 2023.

[2] Qi Xia, Wang-lin Wu, Fu-nian Li, Yong Xia, Xiao-li Ding, William HK Lam, Weng-hong Chung, and You-lin Xu. System design and demonstration of performance monitoring of a butterfly-shaped arch footbridge. *Structural Control and Health Monitoring*, 28(7):e2738, 2021.

[3] Shan Jiang and Stavros Georgakopoulos. Electromagnetic wave propagation into fresh water. *Journal of Electromagnetic Analysis and Applications*, 2011, 2011.

[4] Laura DeNardis. *The Internet in everything*. Yale University Press, 2020.

[5] Jennifer Yick, Biswanath Mukherjee, and Dipak Ghosal. Wireless sensor network survey. *Computer networks*, 52(12):2292–2330, 2008.

[6] Sayed Saad Afzal, Waleed Akbar, Osvy Rodriguez, Mario Doumet, Unsoo Ha, Reza Ghaffarivardavagh, and Fadel Adib. Battery-free wireless imaging of underwater environments. *Nature communications*, 13(1):5546, 2022.

[7] Siqi Ding, Yu Xiang, Yi-Qing Ni, Vijay Kumar Thakur, Xinyue Wang, Baoguo Han, and Jinping Ou. In-situ synthesizing carbon nanotubes on cement to

develop self-sensing cementitious composites for smart high-speed rail infrastructures. *Nano Today*, 43:101438, 2022.

[8] Filippo Ubertini, Antonella D'Alessandro, Austin Downey, Enrique García-Macías, Simon Laflamme, and Rafael Castro-Triguero. Recent advances on shm of reinforced concrete and masonry structures enabled by self-sensing structural materials. In *Proceedings*, volume 2, page 119. MDPI, 2017.

[9] Zhanghao Yu, Fatima T Alrashdan, Wei Wang, Matthew Parker, Xinyu Chen, Frank Y Chen, Joshua Woods, Zhiyu Chen, Jacob T Robinson, and Kaiyuan Yang. Magnetoelectric backscatter communication for millimeter-sized wireless biomedical implants. In *Proceedings of the 28th Annual International Conference on Mobile Computing And Networking*, pages 432–445, 2022.

[10] Vishnu Nair, Ashley N Dalrymple, Zhanghao Yu, Gaurav Balakrishnan, Christopher J Bettinger, Douglas J Weber, Kaiyuan Yang, and Jacob T Robinson. Miniature battery-free bioelectronics. *Science*, 382(6671):eabn4732, 2023.

[11] Dongming Feng and Maria Q Feng. Computer vision for shm of civil infrastructure: From dynamic response measurement to damage detection–a review. *Engineering Structures*, 156:105–117, 2018.

[12] Ian F Akyildiz and Erich P Stuntebeck. Wireless underground sensor networks: Research challenges. *Ad Hoc Networks*, 4(6):669–686, 2006.

[13] Liu Lanbo, Zhou Shengli, and Cui Jun-Hong. Prospects and problems of wireless communication for underwater sensor networks. *Wireless Communications and Mobile Computing*, 8(8):977–994, 2008.

[14] Xiuquan Fu, Weihong Chen, Shuming Ye, Yuewen Tu, Yawei Tang, Dingli Li, Hang Chen, and Kai Jiang. A wireless implantable sensor network system for in vivo monitoring of physiological signals. *IEEE Transactions on information technology in Biomedicine*, 15(4):577–584, 2011.

[15] Umair Mujtaba Qureshi, Faisal Karim Shaikh, Zuneera Aziz, Syed M Zafi S Shah, Adil A Sheikh, Emad Felemban, and Saad Bin Qaisar. Rf path and absorption loss estimation for underwater wireless sensor networks in different water environments. *Sensors*, 16(6):890, 2016.

[16] Xianhui Che, Ian Wells, Gordon Dickers, Paul Kear, and Xiaochun Gong. Re-evaluation of rf electromagnetic communication in underwater sensor networks. *IEEE Communications Magazine*, 48(12):143–151, 2010.

[17] PSS Pavan Ganesh and Hrishikesh Venkataraman. Rf-based wireless communication for shallow water networks: Survey and analysis. *Wireless Personal Communications*, 120(4):3415–3441, 2021.

[18] Lloyd E Emokpae and Mohamed Younis. Throughput analysis for shallow water communication utilizing directional antennas. *IEEE Journal on Selected Areas in Communications*, 30(5):1006–1018, 2012.

[19] Dipesh Dhital, Chen Ciang Chia, Jung-Ryul Lee, and Chan-Yik Park. Review of radio frequency identification and wireless technology for structural health monitoring. *Korean Communication*, 30(3):244–256, 2010.

[20] Akinori Tani, Yuichiro Yamabe, Masashi Murakami, and Motoki UGAJI. Fundamental tests on structural health monitoring systems by using rfid tag with sensors. In *Proc. of 14th World Conference on Earthquake Engineering, DVD-ROM, Paper ID: 11*, volume 149, pages 1–8, 2008.

[21] Muchao Zhang, Zhaoting Liu, Chuan Shen, Jianbo Wu, and Aobo Zhao. A review of radio frequency identification sensing systems for structural health monitoring. *Materials*, 15(21):7851, 2022.

[22] Mateusz Lisowski, Przemyslaw Gonek, Jakub Korta, Tadeusz Uhl, and Wieslaw J Staszewski. Structural damage detection using wireless passive sensing

platform based on rfid technology. *Structural Control and Health Monitoring*, 23(8):1135–1146, 2016.

[23] Abdul Salam, Usman Raza, Abdul Salam, and Usman Raza. Signals in the soil: an introduction to wireless underground communications. *Signals in the Soil: Developments in Internet of Underground Things*, pages 3–38, 2020.

[24] Jian Ding and Ranveer Chandra. Towards low cost soil sensing using wi-fi. In *The 25th Annual International Conference on Mobile Computing and Networking*, pages 1–16, 2019.

[25] Colleen Josephson, Bradley Barnhart, Sachin Katti, Keith Winstein, and Ranveer Chandra. Rf soil moisture sensing via radar backscatter tags. *arXiv preprint arXiv:1912.12382*, 2019.

[26] Nirupam Roy, Mahanth Gowda, and Romit Roy Choudhury. Ripple: Communicating through physical vibration. In *Proc. of USENIX NSDI*, pages 265–278, 2015.

[27] Teresa O'Rourke, Rudiger Pryss, Winfried Schlee, Thomas Probst, et al. Development of a multidimensional app-quality assessment tool for health-related apps (aqua). *Digital Psychology*, 1(2):13–23, 2020.

[28] Junsu Jang and Fadel Adib. Underwater backscatter networking. In *Proc. of ACM SIGCOMM*, pages 187–199. 2019.

[29] Aline Eid, Jack Rademacher, Waleed Akbar, Purui Wang, Ahmed Allam, and Fadel Adib. Enabling long-range underwater backscatter via van atta acoustic networks. In *Proceedings of the ACM SIGCOMM 2023 Conference*, pages 1–19, 2023.

[30] Yuchen Zhao, Sayed Saad Afzal, Waleed Akbar, Osvy Rodriguez, Fan Mo, David Boyle, Fadel Adib, and Hamed Haddadi. Towards battery-free machine

learning and inference in underwater environments. In *Proceedings of the 23rd Annual International Workshop on Mobile Computing Systems and Applications*, pages 29–34, 2022.

[31] Reza Ghaffarivardavagh, Sayed Saad Afzal, Osvy Rodriguez, and Fadel Adib. Ultra-wideband underwater backscatter via piezoelectric metamaterials. In *Proc. of ACM SIGCOMM*, pages 722–734, 2020.

[32] Reza Ghaffarivardavagh, Sayed Saad Afzal, Osvy Rodriguez, and Fadel Adib. Underwater backscatter localization: Toward a battery-free underwater gps. In *Proceedings of the 19th ACM Workshop on Hot Topics in Networks*, pages 125–131, 2020.

[33] Jingyu Qian, Xuesong Lu, Minhao Zhang, Fengzhong Qu, and Yan Wei. Cross-medium communication combining acoustic wave and millimeter wave: Anechoic pool, lake, swimming pool experiments. In *OCEANS 2023-Limerick*, pages 1–7. IEEE, 2023.

[34] Mari Carmen Domingo. Magnetic induction for underwater wireless communication networks. *IEEE transactions on antennas and propagation*, 60(6):2929–2939, 2012.

[35] Christoph Strangfeld, Sergej Johann, Maximilian Müller, and Matthias Bartholmai. Embedded passive rfid-based sensors for moisture monitoring in concrete. In *2017 IEEE SENSORS*, pages 1–3. IEEE, 2017.

[36] Mohamed R Abdelhamid, Ruicong Chen, Joonhyuk Cho, Anantha P Chandrakasan, and Fadel Adib. Self-reconfigurable micro-implants for cross-tissue wireless and batteryless connectivity. In *MobiCom'20: Proceedings of the 26th Annual International Conference on Mobile Computing and Networking*, 2020.

[37] Basem Shihada, Osama Amin, Christopher Bainbridge, Seifallah Jardak, Omar Alkhazragi, Tien Khee Ng, Boon Ooi, Michael Berumen, and Mohamed-Slim

Alouini. Aqua-fi: Delivering internet underwater using wireless optical networks. *IEEE Communications Magazine*, 58(5):84–89, 2020.

[38] Waqas Aman, Saif Al-Kuwari, Ambrish Kumar, and Muhammad Mahboob Ur Rahman. Security of underwater and air-water wireless communication. *arXiv preprint arXiv:2203.02667*, 2022.

[39] Yang Zhao, Jinxin Huang, Penghui Zhang, Yifei Cao, and Zhiquan Zhou. Direct air–water communication by using an optical-acoustic method. *Measurement*, 223:113824, 2023.

[40] Zhi Sun, Pu Wang, Mehmet C Vuran, Mznah A Al-Rodhaan, Abdullah M Al-Dhelaan, and Ian F Akyildiz. Mise-pipe: Magnetic induction-based wireless sensor networks for underground pipeline monitoring. *Ad Hoc Networks*, 9(3):218–227, 2011.

[41] Steven Kisseleff, Ian F Akyildiz, and Wolfgang H Gerstacker. Survey on advances in magnetic induction-based wireless underground sensor networks. *IEEE Internet of Things Journal*, 5(6):4843–4856, 2018.

[42] Zhangyu Li, Zhi Sun, Tarunraj Singh, and Erasmus Oware. Large range soil moisture sensing for inhomogeneous environments using magnetic induction networks. In *2019 IEEE Global Communications Conference (GLOBECOM)*, pages 1–6. IEEE, 2019.

[43] Ian F Akyildiz, Pu Wang, and Zhi Sun. Realizing underwater communication through magnetic induction. *IEEE Communications Magazine*, 53(11):42–48, 2015.

[44] Charles J Carver, Qijia Shao, Samuel Lensgraf, Amy Sniffen, Maxine Perroni-Scharf, Hunter Gallant, Alberto Quattrini Li, and Xia Zhou. Sunflower: locating underwater robots from the air. In *Proceedings of the 20th Annual International Conference on Mobile Systems, Applications and Services*, pages 14–27, 2022.

[45] Charles J Carver, Zhao Tian, Hongyong Zhang, Kofi M Odame, Alberto Quattrini Li, and Xia Zhou. Amphilight: Direct air-water communication with laser light. *GetMobile: Mobile Computing and Communications*, 24(3):26–29, 2021.

[46] Jaeed Bin Saif and Mohamed Younis. Underwater localization using airborne visible light communication links. In *2021 IEEE Global Communications Conference (GLOBECOM)*, pages 01–06. IEEE, 2021.

[47] Fengzhong Qu, Jingyu Qian, Jie Wang, Xuesong Lu, Minhao Zhang, Xuerui Bai, Zhouhua Ran, Xingbin Tu, Zubin Liu, and Yan Wei. Cross-medium communication combining acoustic wave and millimeter wave: Theoretical channel model and experiments. *IEEE Journal of Oceanic Engineering*, 47(2):483–492, 2021.

[48] Francesco Tonolini and Fadel Adib. Networking across boundaries: enabling wireless communication through the water-air interface. In *Proceedings of the 2018 Conference of the ACM Special Interest Group on Data Communication*, pages 117–131, 2018.

[49] Lianyun Yang, Janet Ho, Elshad Allahyarov, Richard Mu, and Lei Zhu. Semicrystalline structure–dielectric property relationship and electrical conduction in a biaxially oriented poly (vinylidene fluoride) film under high electric fields and high temperatures. *ACS applied materials & interfaces*, 7(36):19894–19905, 2015.

[50] Yu Chen, Shaozhao Wang, Huajiang Zhou, Qian Xu, Qingyuan Wang, and Jianguo Zhu. A systematic analysis of the radial resonance frequency spectra of the pzt-based (zr/ti= 52/48) piezoceramic thin disks. *Journal of Advanced Ceramics*, 9:380–392, 2020.

[51] Ling-Sheng Jang, Wai-Hong Kan, Ming-Kun Chen, and Yao-Min Chou. Parameter extraction from bvd electrical model of pzt actuator of micropumps using

time-domain measurement technique. *Microfluidics and nanofluidics*, 7:559–568, 2009.

[52] Surfside condominium collapse. `https://en.wikipedia.org/wiki/Surfside_condominium_collapse`, 2022. Accessed: 2022-1-14.

[53] Shima Taheri. A review on five key sensors for monitoring of concrete structures. *Construction and Building Materials*, 204:492–509, 2019.

[54] Jacques Curie and Pierre Curie. Development by pressure of polar electricity in hemihedral crystals with inclined faces. *Bull. soc. min. de France*, 3:90, 1880.

[55] Jerome P Lynch and Kenneth J Loh. A summary review of wireless sensors and sensor networks for structural health monitoring. *Shock and Vibration Digest*, 38(2):91–130, 2006.

[56] Soonwon Ka, Tae Hyun Kim, Jae Yeol Ha, Sun Hong Lim, Su Cheol Shin, Jun Won Choi, Chulyoung Kwak, and Sunghyun Choi. Near-ultrasound communication for tv's 2nd screen services. In *Proc. of ACM MobiCom*, pages 42–54, 2016.

[57] Qiongzheng Lin, Zhenlin An, and Lei Yang. Rebooting ultrasonic positioning systems for ultrasound-incapable smart devices. In *Proc. of ACM MobiCom*, pages 1–16, 2019.

[58] Lu Zhou, Si-Xin Chen, Yi-Qing Ni, and Alex Wai-Hing Choy. Emi-gcn: a hybrid model for real-time monitoring of multiple bolt looseness using electromechanical impedance and graph convolutional networks. *Smart Materials and Structures*, 30(3):035032, 2021.

[59] Sam Siu, Qing Ji, Wenhao Wu, Gangbing Song, and Zhi Ding. Stress wave communication in concrete: I. characterization of a smart aggregate based concrete channel. *Smart materials and structures*, 23(12):125030, 2014.

[60] Xiaoran Fan, Riley Simmons-Edler, Daewon Lee, Larry Jackel, Richard Howard, and Daniel Lee. Aurasense: Robot collision avoidance by full surface proximity detection. In *2021 IEEE/RSJ International Conference on Intelligent Robots and Systems (IROS)*, pages 1763–1770. IEEE, 2021.

[61] Xin Huang, Jafar Saniie, Sasan Bakhtiari, and Alexander Heifetz. Applying emat for ultrasonic communication through steel plates and pipes. In *2018 IEEE International Conference on Electro/Information Technology (EIT)*, pages 0379–0383. IEEE, 2018.

[62] Boyang Wang, Jafar Saniie, Sasan Bakhtiari, and Alexander Heifetz. Ultrasonic communication systems for data transmission. In *2019 IEEE International Conference on Electro Information Technology (EIT)*, pages 1–4. IEEE, 2019.

[63] Michael T Cunningham, Gary J Saulnier, Robert Chase, Edward M Curt, Kyle R Wilt, Francisco J Maldonado, Stephen Oonk, and Henry A Scarton. Low-rate ultrasonic communications and power delivery for sensor applications. In *MILCOM 2016-2016 IEEE Military Communications Conference*, pages 91–96. IEEE, 2016.

[64] Gary J Saulnier, Henry A Scarton, Andrew J Gavens, DA Shoudy, TL Murphy, M Wetzel, S Bard, S Roa-Prada, and P Das. P1g-4 through-wall communication of low-rate digital data using ultrasound. In *2006 IEEE Ultrasonics Symposium*, pages 1385–1389. IEEE, 2006.

[65] Shahram Etemadi Borujeni. Ultrasonic underwater depth measurement. In *Proceedings of the 2002 Interntional Symposium on Underwater Technology (Cat. No. 02EX556)*, pages 33–36. IEEE, 2002.

[66] Peter Oppermann and Christian Renner. Low-power ultrasonic wake-up and communication through structural elements. In *Proceedings of the 7th Inter-*

national Workshop on Energy Harvesting & Energy-Neutral Sensing Systems, pages 42–48, 2019.

[67] Vincent Liu, Aaron Parks, Vamsi Talla, Shyamnath Gollakota, David Wetherall, and Joshua R Smith. Ambient backscatter: Wireless communication out of thin air. *Proc. ACM SIGCOMM*, 43(4):39–50, 2013.

[68] Vikram Iyer, Vamsi Talla, Bryce Kellogg, Shyamnath Gollakota, and Joshua Smith. Inter-technology backscatter: Towards internet connectivity for implanted devices. In *Proc. of ACM SIGCOMM*, pages 356–369, 2016.

[69] Yao Peng, Longfei Shangguan, Yue Hu, Yujie Qian, Xianshang Lin, Xiaojiang Chen, Dingyi Fang, and Kyle Jamieson. Plora: A passive long-range data network from ambient lora transmissions. In *Proc. of ACM SIGCOMM*, pages 147–160, 2018.

[70] Xieyang Xu, Yang Shen, Junrui Yang, Chenren Xu, Guobin Shen, Guojun Chen, and Yunzhe Ni. Passivevlc: Enabling practical visible light backscatter communication for battery-free iot applications. In *Proc. of ACM MobiCom*, pages 180–192, 2017.

[71] Renjie Zhao, Purui Wang, Yunfei Ma, Pengyu Zhang, Hongqiang Harry Liu, Xianshang Lin, Xinyu Zhang, Chenren Xu, and Ming Zhang. Nfc+ breaking nfc networking limits through resonance engineering. In *Proc. of ACM SIGCOMM*, pages 694–707, 2020.

[72] Dongjin Seo, Ryan M Neely, Konlin Shen, Utkarsh Singhal, Elad Alon, Jan M Rabaey, Jose M Carmena, and Michel M Maharbiz. Wireless recording in the peripheral nervous system with ultrasonic neural dust. *Neuron*, 91(3):529–539, 2016.

[73] Tianyue Zheng, Zhe Chen, Jun Luo, Lin Ke, Chaoyang Zhao, and Yaowen Yang. Siwa: see into walls via deep uwb radar. In *Proc. of ACM MobiCom*, pages 323–336, 2021.

[74] Karthick Subbiah, Saraswathy Velu, Seung-Jun Kwon, Han-Seung Lee, Natarajan Rethinam, and Dong-Jin Park. A novel in-situ corrosion monitoring electrode for reinforced concrete structures. *Electrochimica Acta*, 259:1129–1144, 2018.

[75] Zachary C Grasley, David A Lange, and DD Matthew. Internal relative humidity and drying stress gradients in concrete. *Materials and Structures*, 39(9):901–909, 2006.

[76] Wen Hui Duan, Quan Wang, and Ser Tong Quek. Applications of piezoelectric materials in structural health monitoring and repair: Selected research examples. *Materials*, 3(12):5169–5194, 2010.

[77] Baoguo Han, Siqi Ding, and Xun Yu. Intrinsic self-sensing concrete and structures: A review. *Measurement*, 59:110–128, 2015.

[78] Chih-Yuan Chang and San-Shan Hung. Implementing rfic and sensor technology to measure temperature and humidity inside concrete structures. *Construction and Building Materials*, 26(1):628–637, 2012.

[79] Christoph Strangfeld, Sergej Johann, and Matthias Bartholmai. Smart rfid sensors embedded in building structures for early damage detection and long-term monitoring. *Sensors*, 19(24):5514, 2019.

[80] Sergej Johann, Christoph Strangfeld, Maximilian Müller, Björn Mieller, and Matthias Bartholmai. Rfid sensor systems embedded in concrete–requirements for long–term operation. *Materials Today: Proceedings*, 4(5):5827–5832, 2017.

[81] Young Hak Lee and Taekeun Oh. The measurement of p-, s-, and r-wave velocities to evaluate the condition of reinforced and prestressed concrete slabs. *Advances in Materials Science and Engineering*, 2016, 2016.

[82] R Kishore. Acoustic attenuation in solids. *Physical Review*, 173(3):856, 1968.

[83] Nazli Yesiller, Tuncer B Edil, and Craig H Benson. Ultrasonic method for evaluation of annular seals for wells and instrument holes. *Geotechnical Testing Journal*, 20(1):17, 1997.

[84] B Zhang, Jin Guang Teng, and Tao Yu. Compressive behavior of double-skin tubular columns with high-strength concrete and a filament-wound frp tube. *Journal of Composites for Construction*, 21(5):04017029, 2017.

[85] Jiang Du, Weina Meng, Kamal H Khayat, Yi Bao, Pengwei Guo, Zhenghua Lyu, Adi Abu-obeidah, Hani Nassif, and Hao Wang. New development of ultra-high-performance concrete (uhpc). *Composites Part B: Engineering*, 224:109220, 2021.

[86] Jin-Guang Teng, Yu Xiang, Tao Yu, and Zhi Fang. Development and mechanical behaviour of ultra-high-performance seawater sea-sand concrete. *Advances in Structural Engineering*, 22(14):3100–3120, 2019.

[87] Yunfei Ma, Nicholas Selby, and Fadel Adib. Drone relays for battery-free networks. In *Proc. of ACM SIGCOMM*, pages 335–347, 2017.

[88] Zhijia You and Lingjun Feng. Integration of industry 4.0 related technologies in construction industry: a framework of cyber-physical system. *IEEE Access*, 8:122908–122922, 2020.

[89] Ye Sun, Chen-Yuan Chung, Xiong Bill Yu, Zhen Liu, Yan Liu, and Junliang Tao. Advanced ultrasonic technology for air void distribution in concrete. *Materials Evaluation*, 71(3), 2013.

[90] Open-source design of ecocapsule. https://github.com/Anplus/In-concrete-Backscatter, 2022. Accessed: 2022-6-20.

[91] Ecocapsule project website. https://ecocapsule.tagsys.org, 2022. Accessed: 2022-6-30.

[92] Sidney Mindess. *Developments in the Formulation and Reinforcement of Concrete*. Woodhead Publishing, 2019.

[93] Sla 3d printing materials. https://www.hubs.com/knowledge-base/sla-3d-printing-materials-compared/, 2022.

[94] Solidworks. https://www.solidworks.com/, 2022.

[95] Jlc pcb. https://jlcpcb.com/, 2022. Accessed: 2022-1-14.

[96] Lp5900sd-1.8. https://www.ti.com/product/LP5900/part-details/LP5900SD-1.8/NOPB, 2022. Accessed: 2022-6-20.

[97] Ldo basics. https://www.ti.com/lit/SLYY151A, 2022. Accessed: 2022-6-20.

[98] Ti level shifter txb0302. https://www.ti.com/lit/gpn/txb0302, 2022. Accessed: 2022-6-20.

[99] Ti msp430g2553. https://www.ti.com/product/MSP430G2553, 2022. Accessed: 2022-1-14.

[100] Aht10 integrated temperature and humidity sensor. http://www.aosong.com/en/products-40.html, 2022. Accessed: 2022-6-20.

[101] Bfh1k-3eb full bridge strain gauge. https://www.alibaba.com/product-detail/Taidacent-Customizable-High-Precision-Foil-Resistance_62484048463.html, 2022. Accessed: 2022-6-20.

[102] Rigol dg2052. https://www.rigolna.com/products/waveform-generators/dg2000/, 2022. Accessed: 2022-1-14.

[103] Ciprian hva-800-a. https://www.ciprian.com/high-voltage-amplifiers/, 2022. Accessed: 2022-1-14.

[104] Epc uhf gen2 air interface protocol. https://www.gs1.org/standards/rfid/uhf-air-interface-protocol, 2022. Accessed: 2022-1-21.

[105] Owon xds3000. https://www.owon.com.hk/products_owon_xds3000_series_n-in-1_digital_oscilloscope, 2022. Accessed: 2022-1-14.

[106] Yxlon ff35 ct: High resolution industrial ct system for small/medium-sized parts inspection. https://www.yxlon.com/en/products/x-ray-and-ct-inspection-systems/yxlon-ff35-ct, 2022. Accessed: 2022-1-21.

[107] Concrete slab. https://en.wikipedia.org/wiki/Concrete_slab, 2022.

[108] Ti energytrace technology. https://www.ti.com/lit/pdf/SLAU157AP, 2022. Accessed: 2022-6-20.

[109] Jodie Y Lee, PK Goh, and William H Lam. New level-of-service standard for signalized crosswalks with bi-directional pedestrian flows. *Journal of transportation engineering*, 131(12):957–960, 2005.

[110] Walid Saad, Mehdi Bennis, and Mingzhe Chen. A vision of 6g wireless systems: Applications, trends, technologies, and open research problems. *IEEE network*, 34(3):134–142, 2019.

[111] Hanjiang Luo, Jinglong Wang, Fanfeng Bu, Rukhsana Ruby, Kaishun Wu, and Zhongwen Guo. Recent progress of air/water cross-boundary communications for underwater sensor networks: A review. *IEEE Sensors Journal*, 2022.

[112] Hanjiang Luo, Xiumei Xie, Guangjie Han, Rukhsana Ruby, Feng Hong, and Yongquan Liang. Multimodal acoustic-rf adaptive routing protocols for underwater wireless sensor networks. *IEEE Access*, 7:134954–134967, 2019.

[113] Alejandro Palmeiro, Manuel Martin, Ian Crowther, and Mark Rhodes. Underwater radio frequency communications. In *OCEANS 2011 IEEE-Spain*, pages 1–8. IEEE, 2011.

[114] Charles J. Carver, Tian Zhao, H. Zhang, K. Odame, Alberto Quattrini Li, and Xia Zhou. Amphilight: Direct air-water communication with laser light. In *NSDI*, 2020.

[115] Chi Lin, Yongda Yu, Jie Xiong, Yichuan Zhang, Lei Wang, Guowei Wu, and Zhongxuan Luo. Shrimp: a robust underwater visible light communication system. In *Proceedings of the 27th Annual International Conference on Mobile Computing and Networking*, pages 134–146, 2021.

[116] Marc Blumentritt, Kai Melhorn, Johannes Flachsbarth, Michael Kroener, Wolfgang Kowalsky, and Hans-Hermann Johannes. A novel fabrication method of fiber-optical planar transmission sensors for monitoring ph in concrete structures. *Sensors and Actuators B: Chemical*, 131(2):504–508, 2008.

[117] Zhupeng Zheng, Xiaoning Sun, and Ying Lei. Monitoring corrosion of reinforcement in concrete structures via fiber bragg grating sensors. *Frontiers of Mechanical Engineering in China*, 4(3):316–319, 2009.

[118] Carlos G Berrocal, Ignasi Fernandez, and Rasmus Rempling. Crack monitoring in reinforced concrete beams by distributed optical fiber sensors. *Structure and Infrastructure Engineering*, 17(1):124–139, 2021.

[119] Lan Jen Chu. Physical limitations of omni-directional antennas. *Journal of applied physics*, 19(12):1163–1175, 1948.

[120] Harold A Wheeler. Fundamental limitations of small antennas. *Proceedings of the IRE*, 35(12):1479–1484, 1947.

[121] Yong Cui, Chen Wang, Xiao Song, Ming Wu, Qianyun Zhang, Haiwen Yuan, and Zhihong Yuan. A survey of mechanical antennas applied for low-frequency transmitting. *Iscience*, page 105832, 2022.

[122] Mark A Kemp, Matt Franzi, Andy Haase, Erik Jongewaard, Matthew T Whittaker, Michael Kirkpatrick, and Robert Sparr. A high q piezoelectric resonator as a portable vlf transmitter. *Nature communications*, 10(1):1–7, 2019.

[123] Ahmed E Hassanien, Michael Breen, Ming-Huang Li, and Songbin Gong. Acoustically driven electromagnetic radiating elements. *Scientific reports*, 10(1):1–12, 2020.

[124] Shiwei Tian and Tianxiang Nan. Acoustically driven vlf antennas with high data rates. In *2021 IEEE International Symposium on Antennas and Propagation and USNC-URSI Radio Science Meeting (APS/URSI)*, pages 497–498. IEEE, 2021.

[125] Jinqing Cao, Huiming Yao, Yachen Pang, Jianchun Xu, Chuwen Lan, Ming Lei, and Ke Bi. Dual-band piezoelectric artificial structure for very low frequency mechanical antenna. *Advanced Composites and Hybrid Materials*, 5(1):410–418, 2022.

[126] Huaihao Chen, Xianfeng Liang, Cunzheng Dong, Yifan He, Neville Sun, Mohsen Zaeimbashi, Yuxiao He, Yuan Gao, Patanjali V Parimi, Hwaider Lin, et al. Ultra-compact mechanical antennas. *Applied Physics Letters*, 117(17):170501, 2020.

[127] Jianchun Xu, Zhao Li, Xuchao Pan, Xi Wen, Jinqing Cao, Wen Gong, Shaolong Yang, Ming Lei, Fangzhou Yao, and Ke Bi. Ultra-wideband electrostrictive mechanical antenna. *Advanced Functional Materials*, page 2210868, 2023.

[128] Warren P Mason. Piezoelectricity, its history and applications. *The journal of the Acoustical Society of America*, 70(6):1561–1566, 1981.

[129] Son Xuat Ta, Ikmo Park, and Richard W Ziolkowski. Crossed dipole antennas: A review. *IEEE Antennas and Propagation Magazine*, 57(5):107–122, 2015.

[130] Comsol multiphysics. `https://www.comsol.com/`, 2023.

[131] WI Ibrahim, MR Ghazali, SA Ghani, and Zulkurnain Abdul Malek. Measurement of vertical electric fields from lightning flashes using parallel plate antenna. In *International Conference On Electrical, Control And Computer Engineering 2011 (INECCE)*, pages 466–471. IEEE, 2011.

[132] Ieee standard procedures for measurement of power frequency electric and magnetic fields from ac power lines. *IEEE Std 644-2019 (Revision of IEEE Std 644-2008)*, pages 1–40, 2020.

[133] Constantine A Balanis. *Antenna theory: analysis and design*. John wiley & sons, 2016.

[134] John P Domann and Greg P Carman. Strain powered antennas. *Journal of Applied Physics*, 121(4), 2017.

[135] John Leonidas Volakis and John Leonidas Volakis. *Antenna engineering handbook*, volume 1755. McGraw-hill New York, 2007.

[136] Sony icf-p36 portable radio. `https://www.sony.com/ug/electronics/radios/icf-p36`, 2023.

[137] Brad Brannon. Analog devices: Basics of designing a digital radio receiver. `https://www.analog.com/en/technical-articles/basics-designing-digital-radio-receiver.html`, 2023.

[138] Rigol dg2052 50mhz function generator. `https://www.rigol-uk.co.uk/product/rigol-dg2052-50mhz-function-arbitrary-waveform-generator/`, 2022.

[139] A.h.systems sas-565l passive loop antenna. `https://www.ahsystems.com/catalog/SAS-565L.php`, 2022.

[140] Zheng Gong, Lubing Han, Zhenlin An, Lei Yang, Siqi Ding, and Yu Xiang. Empowering smart buildings with self-sensing concrete for structural health monitoring. In *Proceedings of the ACM SIGCOMM 2022 Conference*, pages 560–575, 2022.

[141] Zheng Gong, Zhenlin An, Jingyu Tong, Donghui Dai, and Lei Yang. Constructing smart buildings with in-concrete backscatter networks. In *Proceedings of the 28th Annual International Conference on Mobile Computing And Networking*, pages 788–790, 2022.

[142] Qiongzheng Lin, Lei Yang, and Yunhao Liu. Tagscreen: Synchronizing social televisions through hidden sound markers. In *IEEE INFOCOM 2017-IEEE Conference on Computer Communications*, pages 1–9. IEEE, 2017.

[143] Ningning Hou, Xianjin Xia, and Yuanqing Zheng. Don't miss weak packets: Boosting lora reception with antenna diversities. *ACM Transactions on Sensor Networks*, 19(2):1–25, 2023.

[144] Vamsi Talla, Mehrdad Hessar, Bryce Kellogg, Ali Najafi, Joshua R Smith, and Shyamnath Gollakota. Lora backscatter: Enabling the vision of ubiquitous connectivity. *Proceedings of the ACM on interactive, mobile, wearable and ubiquitous technologies*, 1(3):1–24, 2017.

[145] Peter Lars Dordal. An introduction to computer networks. 2014.

[146] Erdal Arikan. Channel polarization: A method for constructing capacity-achieving codes for symmetric binary-input memoryless channels. *IEEE Transactions on information Theory*, 55(7):3051–3073, 2009.

[147] Kai Niu, Kai Chen, Jiaru Lin, and QT Zhang. Polar codes: Primary concepts and practical decoding algorithms. *IEEE Communications magazine*, 52(7):192–203, 2014.

[148] Ahmed Elkelesh, Moustafa Ebada, Sebastian Cammerer, and Stephan Ten Brink. Belief propagation list decoding of polar codes. *IEEE Communications Letters*, 22(8):1536–1539, 2018.

[149] Ciprian. High voltage power amplifiers. `https://www.ciprian.com/high-voltage-amplifiers/`, Accessed September 2021.

[150] Peter Oppermann and Christian Renner. Higher-order modulation for acoustic backscatter communication in metals. In *Proceedings of the ACM SIGCOMM 2022 Conference*, pages 576–587, 2022.

[151] Wide input range boost/sepic/flyback dc-dc controller. `https://www.ti.com/product/TPS40210/part-details/TPS40210DRCR`, 2023.

[152] Ic gate drvr half-bridge. `https://www.digikey.com/en/products/detail/infineon-technologies/IRS21867STRPBF/3056635`, 2023.

[153] Nce n-channel enhancement mode power mosfet, nce0102. `https://datasheet.lcsc.com/lcsc/1809291523_Wuxi-NCE-Power-Semiconductor-NCE0102_C161843.pdf`, 2023.

[154] Github stm32 pwm for am transmitter. `https://github.com/kiwih/cubeide-timers-demo`, 2023. Accessed: 2023-6-20.

[155] Texas Instruments. Tlv1117. `https://www.ti.com/product/TLV1117`, Accessed September 2021.

[156] Federal Communications Commission et al. Understanding the fcc regulations for low-power, non-licensed transmitters. *Office of Engineering and Technology*, 34, 1993.

[157] Bruce DeYoung et al. Low power radio: a new communication method for reaching target audiences. 1992.

[158] Christine Erbe, Rebecca Dunlop, and Sarah Dolman. Effects of noise on marine mammals. *Effects of anthropogenic noise on animals*, pages 277–309, 2018.

[159] MSO5000 / MSO5204. `https://rigolshop.eu/product-oscilloscope-mso5000-mso5204.html`, 2023. Accessed: 2023-07-21.

[160] B2900 series precision source/measure units. `https://www.keysight.com/hk/en/products/source-measure-units-smu/b2900-series-precision-source-measure-units-smu.html`, 2022. Accessed: 2022-1-14.

[161] Zhiying Tian, Xin Zhang, and Haochen Wei. A test of cross-border magnetic induction communication from water to air. In *2020 IEEE International Conference on Signal Processing, Communications and Computing (ICSPCC)*, pages 1–4. IEEE, 2020.

[162] Zhi Sun and Ian F Akyildiz. Magnetic induction communications for wireless underground sensor networks. *IEEE transactions on antennas and propagation*, 58(7):2426–2435, 2010.

[163] Ann E Bowles, Samuel L Denes, and Michael A Shane. Acoustic characteristics of ultrasonic coded transmitters for fishery applications: Could marine mammals hear them? *The Journal of the Acoustical Society of America*, 128(5):3223–3231, 2010.

[164] Mark C Watson, Jean-François Bousquet, and Adam Forget. Evaluating the feasibility of magnetic induction to cross the air-water boundary. In *2021 Fifth Underwater Communications and Networking Conference (UComms)*, pages 1–4. IEEE, 2021.

[165] Shaolong Yang, Jianchun Xu, Menghao Guo, Bokun Zhang, Chuwen Lan, Haihong Li, and Ke Bi. Progress on very/ultra low frequency mechanical antennas. *ES Materials & Manufacturing*, 16:1–12, 2021.

[166] H Ding. Darpa mechanical antenna project may set off a military communications revolution. *Conmilit*, 26(4):71–73, 2017.

[167] CQ Ding and HY Song. Theory principle of the ameba antenna based on radiation of mechanical motion of electric charge and magnetic dipole. *Ship Electron. Eng*, 39(2):166–170, 2019.

[168] Zongxin Wang, Zhenxin Cao, and Fei Yang. Radiated field of rotating charged parallel plates and its frequency spectrum. *AIP Advances*, 8(2):025325, 2018.

[169] Chen Wang, Yong Cui, and Minsong Wei. Mechanically-rotating electret ulf/vlf antenna transmitter. In *2019 IEEE International Symposium on Antennas and Propagation and USNC-URSI Radio Science Meeting*, pages 1383–1384. IEEE, 2019.

[170] Y Cui, C Wang, X Song, and BW Liang. Simulation and analysis of mechanical antenna low frequency communication system based on electret material. *Acta Automatica Sinica*, 47(6):1335–1342, 2021.

[171] Wenhou Zhang, Zhenxin Cao, Xiaoyu Wang, Xin Quan, and Mengjiang Sun. Design, array, and test of super-low-frequency mechanical antenna based on permanent magnet. *IEEE Transactions on Antennas and Propagation*, 71(3):2321–2329, 2023.

[172] Qiuping Yi, Na Li, Jin Zhang, and Zhenyuan Sun. A rotating-magnet based mechanical antenna for vlf communication. In *Proceedings of the Seventh Asia International Symposium on Mechatronics: Volume II*, pages 69–77. Springer, 2020.

[173] A Madanayake, S Choi, M Tarek, S Dharmasena, S Mandal, J Glickstein, and A Sehirlioglu. Energy-efficient ulf/vlf transmitters based on mechanically-rotating dipoles. In *2017 Moratuwa Engineering Research Conference (MERCon)*, pages 230–235. IEEE, 2017.

[174] Xiaoyu Wang, Wenhou Zhang, Xin Zhou, Zhenxin Cao, and Xin Quan. Research on permanent magnet-type super-low-frequency mechanical antenna communication. *International Journal of Antennas and Propagation*, 2021:1–16, 2021.

[175] Joseph D Schneider, John P Domann, MK Panduranga, Sidhant Tiwari, Paymon Shirazi, Zhi Yao, Casey Sennott, David Shahan, Skyler Selvin, Geoff McKnight, et al. Experimental demonstration and operating principles of a multiferroic antenna. *Journal of applied physics*, 126(22):224104, 2019.

[176] Mohsen Zaeimbashi, Mehdi Nasrollahpour, Adam Khalifa, Anthony Romano, Xianfeng Liang, Huaihao Chen, Neville Sun, Alexei Matyushov, Hwaider Lin, Cunzheng Dong, et al. Ultra-compact dual-band smart nems magnetoelectric antennas for simultaneous wireless energy harvesting and magnetic field sensing. *Nature communications*, 12(1):3141, 2021.